Morphological Analysis and Post Processing of Platinum-Titanium Nanoparticles

by

Saeed Gholhaki

A thesis submitted to The University of Birmingham

for the degree of Doctor of Philosophy

School of Physics and Astronomy

University of Birmingham

October 2018

Declaration of Authorship

- This work was done wholly or mainly while in candidature for a research degree at this University.
- Where any part of this thesis has previously been submitted for a degree or any other qualification at this University or any other institution, this has been clearly stated.
- Where I have consulted the published work of others, this is always clearly attributed.
- Where I have quoted from the work of others, the source is always given. With the exception of such quotations, this thesis is entirely my own work.
- I have acknowledged all main sources of help.
- Where the thesis is based on work done by myself jointly with others, I have made clear exactly what was done by others and what I have contributed myself.

Abstract

In this thesis, the morphology of bimetallic Pt-Ti nanoparticles were investigated. Scanning Transmission Electron Microscopy (STEM) and X-ray Photoelectron Spectroscopy (XPS) was used to analyse the nanoparticles. Previously, it has been demonstrated that fully oxidised Pt-Ti nanoparticle form multi core morphology as the size of the nanoparticle increases. Here, the nanoparticles were investigated with minimal oxygen exposure and it was observed that the nanoparticle morphology prior to full oxidation is an amorphous alloy structure. Theoretical analysis through DFT calculation was also employed to investigate the addition of oxygen to the nanoparticle in a layer by layer manner. The theoretical results confirmed that the most stable structure after full oxidation is Pt core within the oxide Ti shell.

The thermal energy provided by the electron beam was used to induce a single core formation in the larger 90 kDa nanoparticles. Then, annealing of the sample was used to investigate thermal processing of the nanoparticles. It was observed that single morphology can be achieved by heating to 600 ± 100 ^{o}C and increasing the temperature to 900 ± 100 ^{o}C induced the segregated morphology of Pt-Ti nanoparticle. Therefore, it was possible to post process the morphology of the nanoparticle through heat treatment.

The results obtained from the XPS, demonstrated that the Ti shell is fully oxidised with mostly in TiO_2 and small amount of Ti_2O_3. The Pt core consist of pure Pt as well as a layer of oxide Pt. Thermally heating the nanoparticles to 600 ^{o}C resulted

in reduction of Pt core to fully metallic Pt state and also increased the Ti_2O_3 to TiO_2 ratio of the Ti shell. The reduction was reverted to its original state after exposure to air. The XPS results were compared and confirm through Grazing Incidence X-ray Fluorescence Analysis (GIXRF) and Near-Edge X-ray Absorption Fine Structure (NEXAFS).

To My Parents and My Two Sisters

Acknowledgements

I thank Professor Richard Palmer for the opportunity to work in the NPRL lab. I thank Dr Quanmin Guo and Dr Alex Shard for supervision and for help with corrections to my thesis.

Many thanks to all the colleagues at NPRL and NPL for the useful discussion and their friendship.

Very Special thanks to my parents for all their unconditional support throughout my life and PhD.

List of Publications

S. Gholhaki, S. H. Hung, D. J. H. Cant, C. E. Blackmore, A. G. Shard, Q. Guo, K. P. McKenna and R. E. Palmer. Exposure of mass-selected bimetallic PtTi nanoalloys to oxygen explored using scanning transmission electron microscopy and density functional theory. RSC Advances, 2018,8, 27276-27282.

R. Unterumsberger, P. Hnicke , Y. Kayser, B.x Pollakowski-Herrmann, **S. Gholhaki**, Q. Guo, R. E. Palmer and B. Beckhoff. Characterisation of core-shell nanoparticles by means of reference-free GIXRF and NEXAFS. Submitted.

S. Gholhaki, Q. Guo. Thermally induced morphological changes on bimetallic Pt-Ti nanoalloys. In preparation.

S. Gholhaki, Q. Guo. Characterisation of Pt-Ti nanoalloys using X-ray photoelectric spectroscopy. In preparation.

Contents

Abbreviations

DFT	**D**ensity - **F**unctional **T**heory
HAADF	**H**igh **A**ngle **A**nnular **D**ark **F**ield
FCC	**F**ace - **C**entered **C**ubic
FWHM	**F**ull **W**idth at **H**alf **M**aximum
HCP	**H**exagonal **C**lose **P**acking
HOPG	**H**ighly **O**riented **P**yrolytic **G**raphite
HREELS	**H**igh **R**esolution **E**lectron **E**nergy **L**oss **S**pectroscopy
IMFP	**I**nelastic **M**ean **F**ree **P**ath
STEM	**S**canning **T**ransmission **E**lectron **M**icrocsopy
SC	**S**imple **C**ubic (structure)
STM	**S**canning **T**unneling **M**icroscopy
CAE	**C**onstant **A**nalyser **E**nergy
FRR	**F**ixed **R**etardation **R**ate
CHA	**C**oncentric **H**emispherical **A**nalyser
STS	**S**canning **T**unneling **S**pectroscopy
TEM	**T**ransmission **E**lectron **M**icrocsopy
TP	**T**urbo **P**ump
vdW	**v**an-**d**er-**W**aals
XPS	**X**-ray **P**hotoelectron **S**pectroscopy
GIXRF	**G**razing **I**ncidence **X**-ray **F**luorescence
SMTB	**S**econd **M**oment approximation of the **T**ight **B**inding

Chapter 1

Introduction

Nanoscience is a relativity new branch of science that connects several disciplines such as physics, chemistry, biology and engineering together. This field focuses on materials and phenomena occurring at the nanoscale. The range is considered to be from 100 nm to a single atom. There are two approaches for structuring and production of nano-materials, Top-Down and Bottom-Up. Methods such as conventional lithography-etching techniques are categorised as Top-Down approaches, in this approach one starts out with bulk material and modifies the material down to the nanoscale. On the other hand, in the Bottom-Up approach, the nano-structures are built atom by atom or molecule by molecule.

The work presented in this thesis focuses on the morphology of bimetallic Pt-Ti nanoparticles, physically synthesised in a gas phase and size selected prior to deposition. In chapter 2, a detailed review of literature is provided. The chapter starts with a discussion on the importance of bimetallic nanoparticles, in particular platinum based nanoparticles. The catalytic volcano plot is discussed, this will highlight the importance of platinum alloying to obtain better catalysts. The theoretical and experimental motivations behind the Pt-Ti alloying is also presented. The possible routes for nanoparticle synthesis are also compared including gas condensation method used in this work. A detailed review of the morphological stability of the bimetallic nanoparticles is given, and the influence of oxygen and thermal annealing is studied. Finally, the chapter presents an overview of the literature on the analytical techniques used in this work i.e. X-ray photoelectron spectroscopy and electron microscopy of nanoparticles.

In Chapter 3, the techniques used to produce and characterise the nanoparticles are introduced. It starts by describing the magnetron gun cluster source including the annealing setup and the inert gas transfer glove box. Then, the technical details of the STEM used in this work is explained as well as the intensity calibration process. The physics and instrumental properties of the XPS setup is also described and finally the data analysis software employed for nanoparticle analysis is detailed.

Chapters 4,5 and 6 present the experimental results. Chapter 4 focuses on the oxidation effects on the structure of Pt-Ti nanoparticles. The size distribution is provided and the modification through oxygen exposure is explored. The experimental results are also compared to the theoretical calculations.

Chapter 5 demonstrates the electron beam nanoparticle interactions. The single core morphology induced by the electron beam was achieved in a large scale by thermal annealing the nanoparticle. It was shown that the thermal energy can be used to control the morphology of the nanoparticle. The HAADF STEM intensity was used to determine the position of the core after thermal treatment.

The chemical state of the nanoparticle before and after heat treatment was explored using XPS and the results are presented in chapter 6. It was observed that the Pt core reduced to its pure metallic form after thermal treatment. The XPS intensity was used to determine the shell thickness through use of the T_{NP} method which utilises relative XPS signal of the present elements, the method is described in the chapter. Finally GIXRF was used to compare the results with the XPS.

Finally, chapter 7 summarises all the main findings and describes possible future work that can be done in this area.

Chapter 2

Literature Review

2.1 Nanoparticles

Nanoparticles are an intermediary stage between the bulk matter and isolated atoms. It is established that nanoparticles show novel properties compared to their bulk [1]. Therefore the main aspects of nanoparticles, for instance synthesis, characterisation and applications are among the most important sections of nanotechnology.[2] These novel properties have been demonstrated to be significantly applicable in the fields of catalysis, drug delivery and electronics [3].

The bulk state and individual atom are the two extreme ends of the spectrum for matter, both have their unique electronic properties, discrete energy states and bands of energy states, respectively [4]. In between, aggregates of individual atoms, nanoparticles which exhibit completely different behaviours to the bulk or single atom exist. The properties of nanoparticles strongly depend on the number of constituents, which can range from 2 to 10^{6-7} atoms [5]. Nanoparticles can be made from most elements in the periodic table. A single element can be used to produce pure nanoparticles or a mixture of different elements to obtain alloy nanoparticles. The size of nanoparticles can be estimated by considering the packing of hard spheres into a spherical volume. It provides a rather reasonable mapping of nanoparticle size to diameter and fraction of surface atoms. This simple model assumes the total volume of a nanoparticle V_n with N atoms to be [6]

$$V_n = NV_a \tag{2.1}$$

Where V_a is the volume of a single bulk atom. Substituting the equation for volume gives

$$\frac{4\pi}{3}R_n^3 = N\frac{4\pi}{3}R_a^3 \tag{2.2}$$

The nanoparticle diameter (D_n) is then

$$D_n = N^{1/3}2R_a \tag{2.3}$$

Similarly the surface area of the nanoparticle S_n is related to the surface area of the atom S_a by

$$S_n = N^{2/3}S_a \tag{2.4}$$

The properties of the nanoparticle such as catalytic properties and optical properties depend on the diameter and the surface area of the nanoparticle. Therefore, it is crucial to be able to determine the nanoparticle morphology and structure. The advancement in the field of electron microscopy such as development on spherical-aberration corrected Scanning Transmission Electron Microscopy, has made electron beam microscopy a highly useful technique for investigating nanoparticles. However, the electron beam induced effects must be taken into account.

2.1.1 Platinum Based Nanoparticles

Bimetallic nanoparticles, consist of two different elements such as metals, have attracted a greater interest than the single element nanoparticles. [7, 8]. This is due to the additional control parameter on the final properties of the nanoparticle by fine tuning the composition and the morphology. In particular, Pt based bimetallic nanoparticles have attracted great attention due to the importance of Pt nanoparticles in hydrogen fuel cells. It is favourable to reduce the loading of Pt due to great difficulty associated with mining Pt as well as the rarity of the element. Figure 2.1 shows a volcano plot for the activity of each metal plotted against oxygen binding energy obtained from Density Functional Theory (DFT) calculations done by Norskov *et al* [9]. It is clearly visible that Pt is the closest element to the ideal point at the peak of the volcano plot [9]. If the oxygen attaches too strongly to the surface it can dissociate or even result in catalyst poisoning, this is the case for the elements on the right-hand side. On the other hand if the oxygen binding is too weak, it will be less likely for the oxygen to attach to the catalyst surface at the cathode, this is the case for the elements on the left-hand side. Therefore Pt is the best candidate followed closely by Pd.

It is desirable to move closer to the peak of the volcano plot. Alloying the Pt nanoparticle is the best option in achieving such an outcome. In addition, the mixing of another metal with Pt reduces the loading of Pt and the production costs. Greeley *et al* [10] demonstrated that alloying Pt with different transition

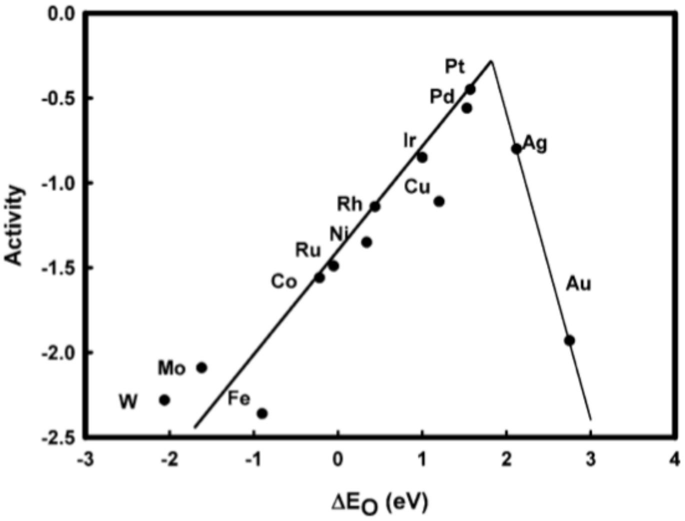

Figure 2.1: Pt is the closest to the ideal activity against the molecular oxygen binding energy point. This suggest that Pt based catalysts would offer the best balance of oxygen binding energy. Figure and caption from [9]

metals result into better catalytic performance. Figure 2.2 presents the volcano plot for Pt based bimetallic metals. Pt_3Ni was deduced to be the best with Pt_3Y closely placed as second.

Furthermore Greeley *et al* [11] also showed that surface structure of the studied material heavily influences the activity and oxygen binding energy. For instance, the (211) step edge site on a Pt surface demonstrated the lowest activity and oxygen binding energy in comparison to the (100) and (111) facets. By reducing the size of the material to the nanoscale, one can tailor the surface structure to the most desired morphology which may be energetically unfavourable to form on the bulk state. The size reduction of the material into smaller particles also makes the most efficient use of the precious resources. This is achieved by increasing the surface atom to bulk atom ratio, compared to the bulk state.

In particular, the performance of Pt-Ti nanoparticles in fuel cells was studied by DFT modelling [12, 13]. The focus of the study was mainly on high symmetry structures of Pt rich $Pt_{32}Ti_6$ nanoparticles. The studied structures are presented in figure 2.3. The structures were based on Truncated Octahedron(TO): Core-Shell,

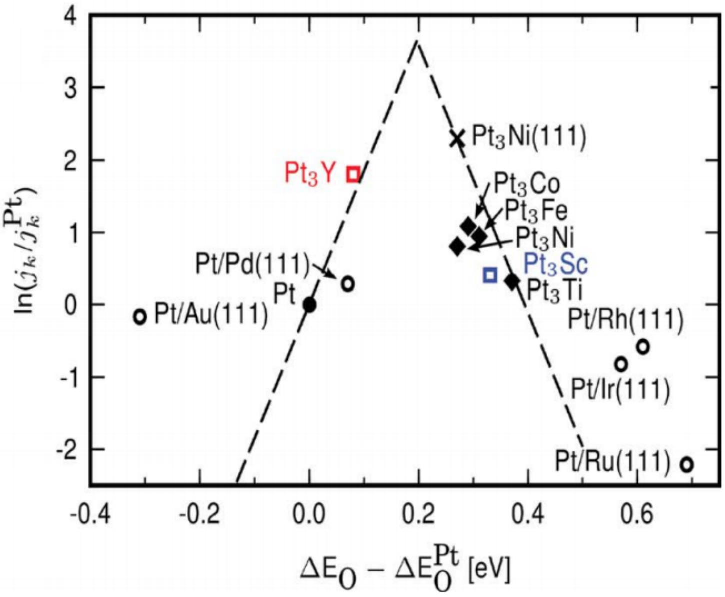

FIGURE 2.2: A volcano plot demonstrating the activity of Pt based bimetallic metals as a function of molecular oxygen binding energy. The Y scale is normalised to pure Pt. Pt_3Ni and Pt_3Y shows the best catalytic performance, where jk is the kinetic current density. Figure and caption from [10]

Hex and centroid TO configurations. The figure only shows three possible distribution of Ti atoms within the Pt nanoparticle. The calculations were performed for two different reactions, hydroxyl adsorption and carbon monoxide adsorption. The DFT results suggested that addition of Ti to the Pt nanoparticle reduces the binding strength between the hydroxyl molecules. This results to a faster oxygen reduction reaction which is desired for the catalytic reaction. In addition, it was observed that the carbon monoxide molecules bind to the Pt atom was also weaker in comparison to the pure Pt nanoparticles, this also improves the catalytic performance by minimising the catalytic poisoning level within the fuel cell.

The catalytic performance of the Pt_3Ti have also been studied experimentally [14–18]. For example, Hideki Abe *et al* [17] examined oxidation of formic acid and methanol by electrocatalysis on Pt_3Ti in the form of nanoparticles synthesised chemically. The experiments consisted of ordered and disordered Pt_3Ti structure, Pt-Ru and pure Pt catalyst. Figure 2.4 presents the CO stripping profile results. It can be seen that the current densities after CO exposure i.e. full curves on (a)

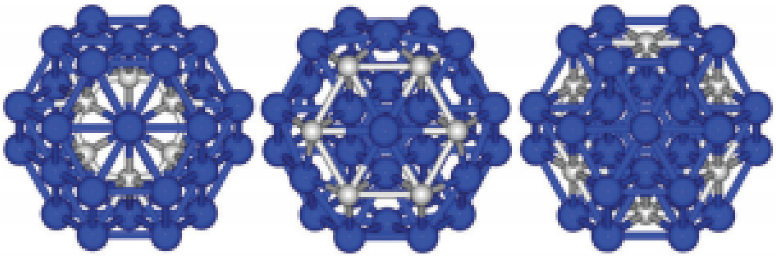

FIGURE 2.3: Cross sectional view of studied structures of $Pt_{32}Ti_6$ nanoparticles. The nanoparticle consists of 32 Pt atoms presented by blue marbles and 6 Ti atoms presented by grey marbles. Core-Shell, Hex and Centroid TO configuration. (left to right) Figure and caption from [12]

pure Pt and (b) Pt-Ru, are nearly zero relative to the current densities before CO exposure i.e. dashed curves. This suggest that in both cases, the strong affinity toward CO adsorption, results in passivation of the catalyst surface by irreversible adsorption of CO. Similar behaviour is also observed for disordered Pt_3Ti, however in contrast the stripping peak is much weaker than that of either pure Pt or Pt-Ru. The ordered Pt_3Ti nanoparticle shows an even weaker stripping peak than that of disordered Pt_3Ti. It can be deduced that both ordered and disordered Pt_3Ti nanoparticles have a much lower affinity toward CO adsorption.

Looking from a different perspective, the Pt-Ti mixture has also been reported to be useful in a different part of fuel cell energy cycle. TiO_2 has been known as one of the best candidates for water splitting which is essential to the energy production cycle. As without a clean supply of fuel, the application of hydrogen fuel cells are limited. In order to enhance the photocatalytic properties of TiO_2, alloying of the TiO_2 nanoparticle with elements such as Pt, Au , Rh, Ni, Cu and Ag have been reported. [19–29]. The addition of such elements to the TiO_2 modifies the absorption of the electromagnetic spectrum, minimises the probability of backward reaction where hydrogen and oxygen can re-create water or reduces electron - hole recombination. In particular, it has been demonstrated that addition of Pt to the TiO_2 can improve the photocatalytic activity, for instance in photohydrogenation of CH_3CCH with H_2O. [30–32]. This is mainly due to the enhanced charge

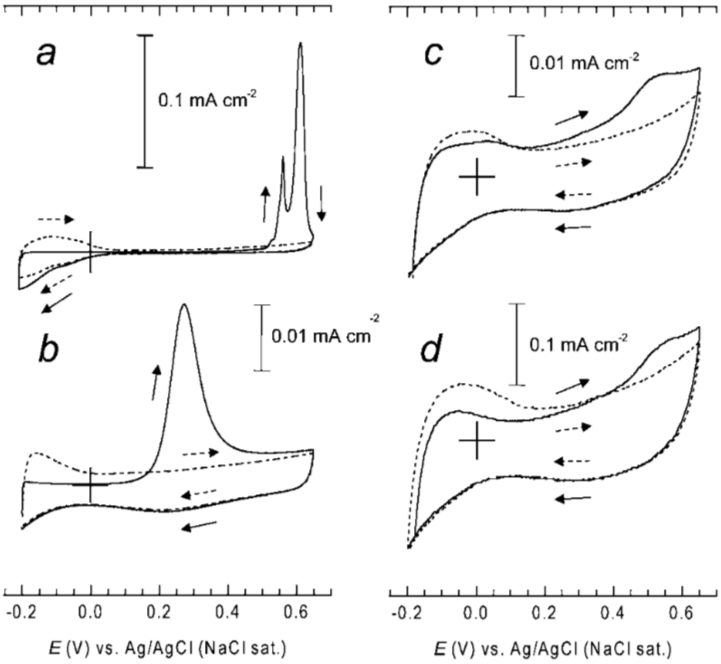

FIGURE 2.4: CO stripping profiles of (a) pure Pt, (b) Pt-Ru, (c) atomically disordered Pt_3Ti nanoparticles (d) atomically ordered Pt_3Ti nanoparticles. The dashes curves corresponds to the CV data before and solid line curves are after CO exposure. Figure and caption from [17]

separation between photo-formed electrons and holes. [30].

2.2 Nanoparticle Synthesis Methods

There are variations routes for producing nanoparticles. These methods are mainly categorised as chemical and physical methods [33–36]. Chemical synthesis is currently the most dominant method, mainly due to high production rate, and also because scaling up the production method is relatively a simple process. However it also has disadvantages, for example, poor size distribution of the nanoparticles when in most cases the size of nanoparticle is crucial, lack of precise control on the elemental composition as well as contamination from chemicals used during the synthesis process [37]. On the other hand, physical production offers better size and elemental composition control and cleaner nanoparticles without contamination from any undesired chemicals. But the production rate is limited and the scale up process is complex.

2.2.1 Chemical Production Methods

Chemical synthesis is generally performed in liquid phase. Specific chemicals are added to a reactor at elevated temperature to make certain elements precipitate to form particles. The particle characteristics is controlled by the initial reactants, reaction time and temperature. The size and compositions can be adjusted in a more precise manner by following a specific procedure, precursor quantities and vessel shape. Pt based nanoparticles are generally created with H_2PtCl_6 as the starting material with a reactant agent of potassium sitrate as described by Cushing *et al* [38].

Electrochemical reduction is another technique. In this method, electric current is used to induce and control the reaction. The electric current is passed through two electrodes with an electrolyte positioned between them. The metallic anodic sheet is then dissolved and metallic salt formed is reduced by the cathode to nanoparticles. The nanoparticles are then stabilised by the addition of a ligand species. [39, 40]

Radiation asisted production is another method, where γ radiation is used to initiate the precipitation reaction. Belloni *et al* [41] reported of successful production of silver nanoparticles in addition to elements like Cu, Pd, Pt, Pb and Au.

2.2.2 Physical Production Methods

Physical methods for nanoparticle synthesis generally produce dry nanoparticles which can be simply characterised and investigated by techniques that require vacuum to operate, such as electron microscopy, X-ray photoelectron spectroscopy (XPS) or mass spectroscopy techniques to determine size distribution.

The simplest method is ball milling where ceramic balls are used to grind a material until a desired size is achieved. It has been demonstrated that nanoparticles can be produced with an average size of less than 30 nm [42, 43]. An advantage of this method is that materials that are not compatible under normal condition due to their thermodynamic equilibrium, can be combined to produce nanoparticles due to the high pressure created when milling. However the biggest disadvantage of this method is the polydispersity of the nanoparticles produced. Therefore an extra step may be needed to filter out the nanoparticles with undesired sizes. The process may also add contamination from the materials of the milling balls and vessel. Therefore, numerous sophisticated physical techniques have been developed to produce nanoparticles with greater accuracy on the size and with minimal contamination.

Supersonic expansion nozzle sources [44, 45] take advantage of adiabatic expansion when a gas rapidly expands after entering a vacuum chamber to form a beam of nanoparticles. Hence, the source material need to be in the liquid form to be able to mix with the gas, prior to expansion. Figure 2.5 presents a schematic of super sonic expansion nozzle designed by De Heer and Knight [46]. A nanoparticle beam is generated when the metal - gas vapour mixture passes through the nozzle by the supersonic expansion. The control parameters are the pressure inside the chamber, temperature, nozzle size and gas which can be adjusted to determine the size and flux of the nanoparticles. The size ranges between 1 to 1000 atoms [46]. Since the nanoparticles travel in a beam where all the different sizes are mixed, the desired size can be precisely selected through a mass select setup [47]. The disadvantage of such a system is the low melting point temperature requirement for the material so that the material can be melted to a liquid state without the chamber overheating.

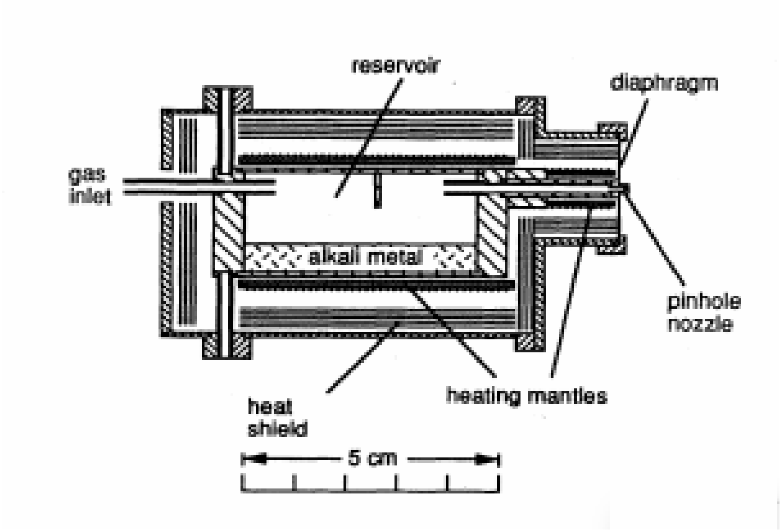

Figure 2.5: Setup of a supersonic expansion nozzle. The metal is evaporated so that a mixture with the gas is possible to form a nanoparticle beam. Figure and caption from [46].

Laser ablation can be employed to overcome the limiting factor, i.e. melting point requirements. The laser source can be used to vaporise the metal to produce nanoparticles. A burst of helium gas is released into the chamber simultaneously as the metal is vaporised to carry the nanoparticles away from the vaporisation site. The helium gas injection and the length of the laser pulse can be used to determine the final nanoparticle size between 2 to 10 nm [48, 49]. Figure 2.6 presents a diagram of a laser vaporisation source. In this particular system, the laser enters the chamber through the hole on the top and melts the rod at the bottom of the chamber. The atomic vapour is then pulsed out through nozzle.

Nanoparticle formation through gas condensation is also another well known method [50, 51]. Generally, a crucible of material is heated to evaporate the source material or a magnetron sputtering device is employed to eject atoms out of the target. The evaporated or sputtered atoms are then cooled by an injected gas and high pressure inside the chamber. The gas is needed to take away the excess energy of the atoms through three body collision, which results in the nanoparticle formation. There is no limit on the growth of the nanoparticle, therefore any size from two atoms to thousands of atoms is achievable. Figure 2.7 presents a schematic for

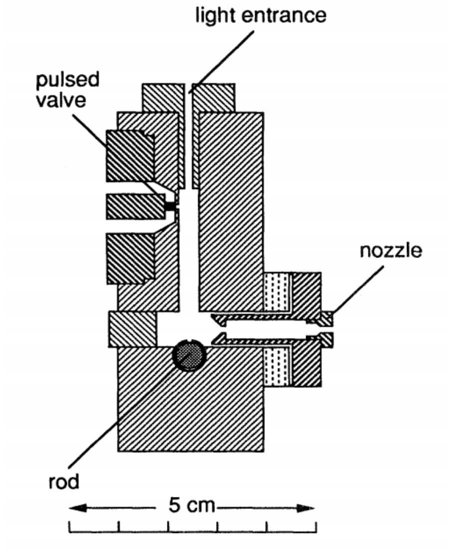

FIGURE 2.6: An example diagram of a laser ablation nanoparticle source. The entrance at the top is where the laser enters the chamber and heats the rod at the bottom. The pulsed valve releases gas to transfer the gas - material mixture through the nozzle. Figure and caption from [46].

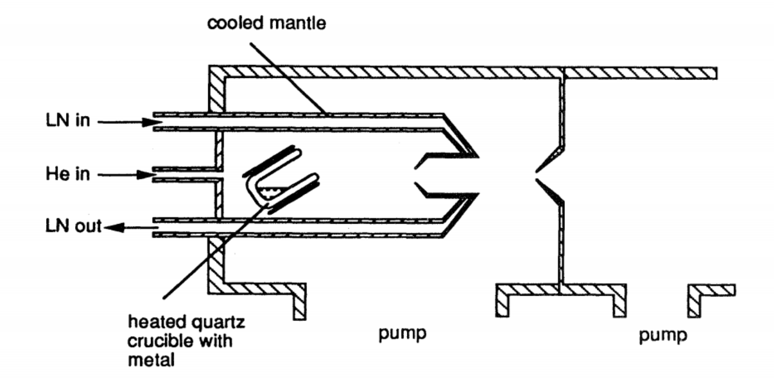

FIGURE 2.7: Schematic for a gas evaporation condensation nanoparticle beam source. A hot crucible is used to heat metal. The evaporated atoms are then condensed with the aid of liquid nitrogen. Figure and caption from [46].

an evaporation setup. Figure 2.8 presents an example for magnetron sputtering gas condensation source.

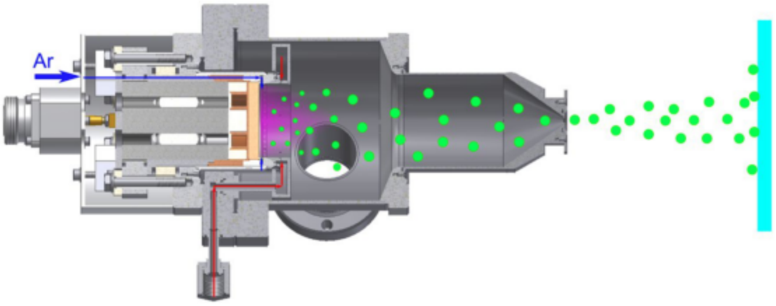

Figure 2.8: An example of a magnetron sputtering gas condensation nanoparticle beam source. The sputtered atoms are cooled and form nanoparticles which can be deposited on a substrate. Figure and caption from [51]

2.2.3 Bimetallic Nanoparticle Production

As mentioned earlier, the simplest method for nanoparticle synthesis in large quantities is through chemical preparation, this is also the case for bimetallic nanoparticles [52]. However, the size of the nanoparticle is crucial for any intended application, which highlights the importance of size control during the synthesis process. This is generally not achievable in a chemical process, hence it results in large size distribution. In addition, in most cases the nanoparticles are covered by organic molecules in order to passivate and prevent aggregation during the synthesis process [6]. The passivation through ligand achievements is highly likely to affect the properties of the nanoparticle and therefore undermine their potential use. In order to eliminate such issues, one can use physical methods to produce highly monodisperse nanoparticles with clean surface, since nanoparticles deposited on solid substrate are less likely to aggregate in comparison to colloidal suspension.

There are many benefits in production of nanoparticles with more than one element. The most important is the cost reduction due to the ability of mixing with a cheaper and more abundant material. The alloying can also lead to property enhancement. However, there is no guarantee that the final product is a core-shell structure. The final nanoparticle might have half element A and half element B or mixtures to different degrees.

The combination of two or more elements opens more possibilities for production of more advanced materials by enhancing or even developing new properties. Here, the focus is mainly on metals. There has been a huge interest for the production of bimetallic or even trimetallic nanoparticles for a variety of applications [52–54]. The significant interest in these nanoparticles has resulted in many different techniques for production being investigated. In particular, gas-phase methods have become popular due to lacking the aforementioned challenges of chemical methods. There are mainly two distinct techniques, the first method is the use of mixed source targets or multiple targets with different materials. Secondly, coating of the nanoparticles with a second or third material after deposition on a substrate [6].

Coating and Annealing after Deposition of Supported Nanoparticles

Bimetallic nanoparticles can be produced by coating already deposited nanoparticles using various vapour deposition techniques *in situ*. Initially, the material with stronger bonding to the substrate is deposited. This results in initial single element nanoparticles on the surface which then can act as seed nuclei for further bimetallic nanoparticles. In order to permit diffusion and aggregation of deposited atoms during deposition, the substrate is heated to high temperature. The core-shell nanoparticle can be formed in this way by not only taking into account the substrate bonding but also the surface free energies and the miscibility of the involved elements [6].

Chen *et al* [55], reported formation of Pt-Au nanoparticles on the TiO_2 substrate by this method. Initially Pt nanoparticles were formed on the substrate surface, then Au atoms were deposited at room temperature to from bimetallic Pt and Au nanoparticles. STM imaging before and after of gold deposition showed the formation of alloy nanoparticles, since the particle surface coverage density stayed the same before and after Au deposition but the overall size of the nanoparticles increased after. Low energy ion scattering experiments were then employed to confirm the presence of AuPt nanoparticles in an intermixed state rather than a core-shell morphology. Platinum has a higher surface energy than gold in the bulk. Therefore one might expect thermodynamically for Pt to form the core and Au to make up the shell. This was not clearly the case. This is a perfect example that the nanoparticle properties are quite different to the bulk properties [6].

One disadvantage of this method is the broad size distribution of the final product. However it has been shown that by employing size-selected nanoparticles with narrow size distribution as the seed, the final bimetallic nanoparticles will inherit the narrow size distribution to an acceptable extend [56].

This method is relatively straightforward. However, it does suffer from lack of precise size control on the final product. It can be improved by utilising size-selected nanoparticles as seeds.

Bimetallic Nanoparticles by Sputtering of Mixed or Double Targets

Production of bimetallic nanoparticles by the use of double target or an alloy target is the most common physical technique. It is straight forward and feasible if one already has a sputtering source. As discussed earlier, the laser ablation is the most widely used method for this purpose. There can be either a single laser on a single alloy target or two lasers for two adjacent targets [6]. The binary mixture produced by the lasers is then further cooled using an inert gas so that nanoparticles formation takes place, which are then directed onto a substrate.

Bi-elemental nanoparticles other than metal-metal combination have also been generated through laser vaporisation such as metal-oxide and metal-semiconductor. These type of nanoparticles have not been constraint to only small sizes. But, it has been demonstrated that control of the size distribution and the elemental composition is more challenging than in the case of metal-metal particles.

Laser ablation has been a popular method mainly for the advantage of material versatility. However, the pulse operation becomes a massive drawback when a great continuous output of nanoparticles is needed [6]. The magnetron sputtering technique offers high throughput and continuous operation. For instance, Sumiyama *et al* [57] demonstrated that for metal nanoparticles, the target can be operated in either DC glow discharge or in RF glow discharge. However, for production of semiconductor and insulator material, one has to set the target to RF glow discharge.

Bimetallic nanoparticles in core-shell structure of Co-Si and Fe-Si were produced by sputtering method. Alloy structure of CoPt and CoAl have also prepared with this system. The two targets can be separated by positioning a plate between the targets [57]. It was observed that when a plate was positioned in-between the targets, no bimetallic nanoparticles were detected. This shows the importance of the vapour mixing of the two materials.

Jose-Yacaman group [58] have demonstrated that a commercial uni-target magnetron sputtering source can be used to produce AuPd alloy nanoparticles from AuPd alloy target. The size was tuned using adjustments on the evaporation conditions.

Nanoparticles with a diameter of 1.10 ± 0.44 nm, 3.00 ± 0.30 nm and 5.00 ± 0.07 nm were generated.

Bimetallic Nanoparticles by In-flight Coating

Another interesting method of production of bimetallic nanoparticle is in-flight coating of the single element particles with an additional element. The feasibility of this method was proven by Harbich's group [59–61]. The aim was to condense solid rare-gas matrix films onto a substrate cooled to temperatures around helium liquid. Then a thin film of the desired material such as gold is evaporated on top of the matrix. Finally size-selected nanoparticles can then travel through the mixture to be coated in flight before deposition on the substrate.

In order to demonstrate the method, silver atoms were condensed on a frozen layer of rare gas to investigate the porosity of the film. Atomic Force Microscopy (AFM) and Scanning Electron Microscopy (SEM) were used to image and characterise the self supporting metal film replica of the frozen solid rare gas matrix surface structure. By varying the condensation time different thicknesses were produced. The pore sizes and density could also be adjusted through varying the temperature of the condensation.

2.3 Morphology of Bimetallic Nanoparticles

2.3.1 Morphological Stability

Nano-alloys or bimetallic nanoparticles offer great tunability of the physical and chemical properties through material choice as well as size control and morphology. The morphology of the nanoparticle is crucial in determination of final properties. Therefore, the stability of the desired morphology is greatly important in the real world use of bimetallic nanoparticles.

The morphology of a bimetallic nanoparticle is determined through its geometric structure and its chemical ordering. The chemical ordering is the arrangement of two different elements within a geometric structure [62]. The stability of nanoparticles for both single and multi elemental composition are generally determined by the surface energies and in particular interface energies for bimetallic nanoparticles and strain within the nanoparticle as well as quantum effects i.e. electronic

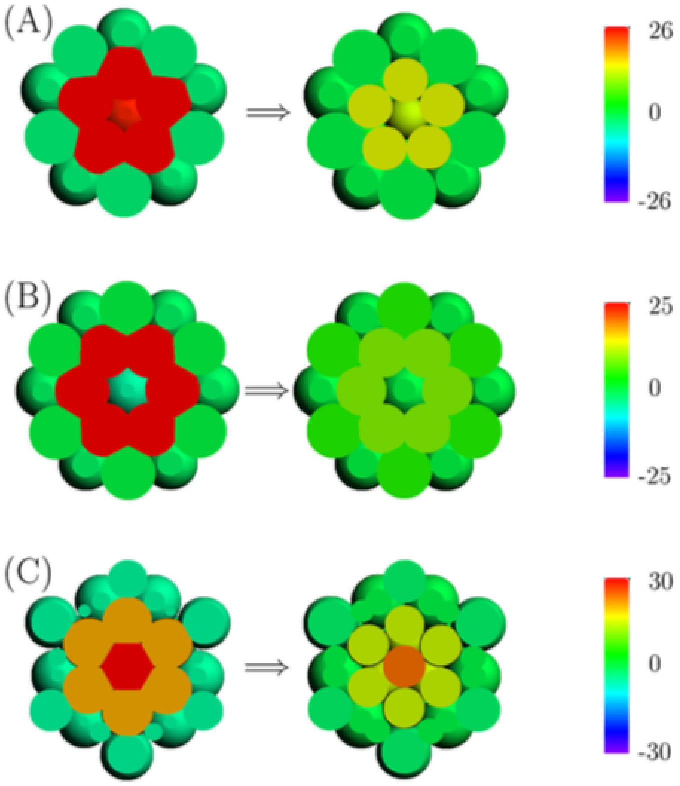

Figure 2.9: (A)polyicosahedra-5, (B)polyicosahedra-6 and (C)anti-Mackay are three different structure. On the left-hand side is the pure Ag nanoparticle and on the left is the same nanoparticle but the inner Ag atoms are replaced by Cu atoms.It is clear than all structures are locally relaxed after allying. Pressures are in GPa. Figure and caption from [62]

shell effects. Ferrando *et al* [62] demonstrated using SMTB potential calculations how mixing of Cu and Ag can enhance the stability of Ag nanoparticles. Figure 2.9 shows the pressure map of pure Ag on the left for three different structure. The Cu atoms are smaller than Ag atoms, therefore, when the internal Ag atoms are substituted by Cu atoms the strain within the nanoparticle is released as it is clear on the left-hand side figure.

In particular, it has been demonstrated by DFT calculations that relative stability of bimetallic Pt-TM nanoparticles (TM = Fe, Co, Ni, Cu, Zn) with 55-atoms increases with respect to their parent compounds with alloying .[63] The report considered one of the key parameters involved in the stability of bimetallic nanoparticles, the excess energy E_{exc}. Figure 2.10 shows the excess energy as a

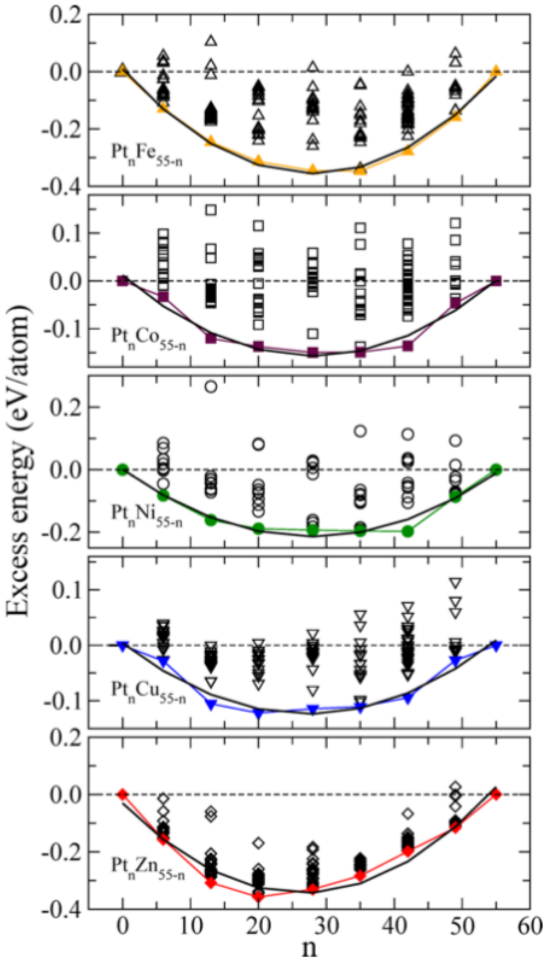

FIGURE 2.10: Excess energy against composition for Pt$_n$-TM$_{55 \rightarrow n}$. The coloured curved line connects lowest energy configuration for each case, the black symbols on each panel demonstrates the excess energy for different possible configuration

. The black curved line was obtained by a parabolic fitting of the lowest energy curves i.e the coloured lines. Figure and caption from [63].

function of composition.

It can be seen that the formation of the bimetallic Pt$_n$-TM$_{55\text{ - }n}$ nanoparticles is energetically favourable for all systems and compositions since the excess energy is negative for all cases. The excess energy has a parabolic behaviour and it decreases as the Pt atoms are replaced by TM atoms. This suggests that bimetallic nanoparticles, when both metals are miscible, should be expected to be more stable when forming alloy nanoparticles.

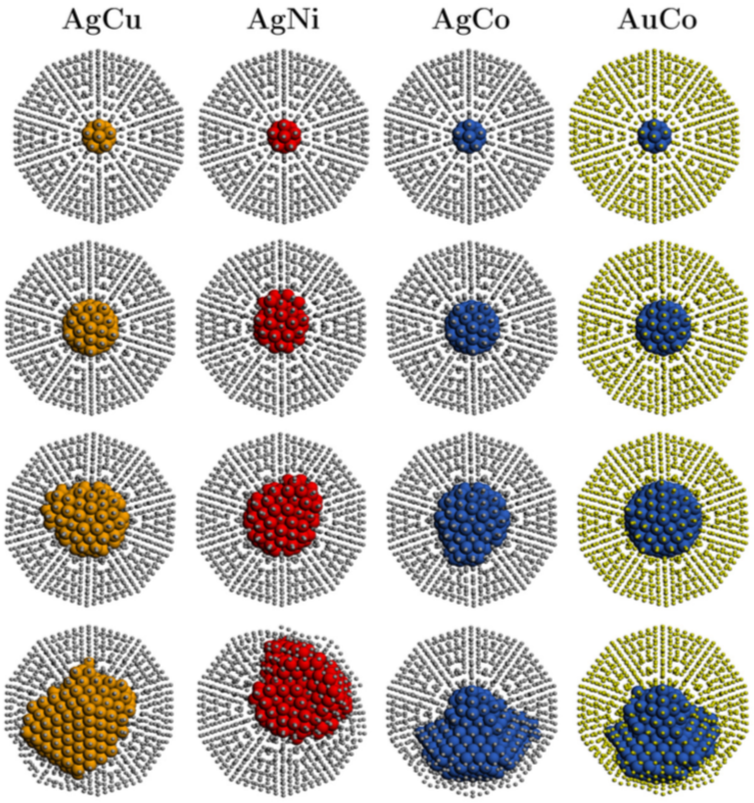

FIGURE 2.11: Lowest-energy configuration of Cu@Ag, Co@Ag Co@Au and Ni@Ag nanoparticles. As the core size increases, the symmetry of the structure is also broken. The core areas contain 13, 55, 147, or 309 atoms from top to the bottom accordingly. The symmetry breakage is mainly due to build up of strain within the nanoparticle as the core size increases. Figure and caption from [64]

Bimetallic nanoparticles do not always preserve the symmetrical morphology, in other words, it has been shown that the lowest energy i.e. the most theoretically stable structure for bimetallic nanoparticles sometimes is the one without a symmetry. For instance, Bochicchio *et al* [64], demonstrated that for icosahedron structure of Cu@Ag, Co@Ag Co@Au and Ni@Ag, with 1415 atoms in total (@ represent Core@Shell structure), when the core is small, the lowest energy is the structure with symmetrical core-shell structure, however as the core size increases, the development of irregular shapes and asymmetrical structure is more favourable. Figure 2.11 presents the results. This is mainly caused by the accumulation of strain as the core size increases. If the number of atoms in the shell is increased, the morphological instability is gradually suppressed.

The theoretical stability of the bimetallic nanoparticles provides an insight into the potential final structure of the nanoparticle, however in any real world application the conditions are far from the zero kelvin - clean environment that the nanoparticles are generally considered in. In reality, the environment is far more complex than the ideal environment for the use of nanoparticles. The first issue is the presence of abundance oxygen in the air, which can have huge impact on the final structure of the nanoparticle in particular in metal-metal bimetallic nanoparticles. This leads to the oxidation effect on the morphology of the nanoparticles.

2.3.2 Oxidation Effect

Oxygen effect consideration is crucial in the production of stable bimetallic nanoparticles. No matter what the original arrangement of elements was during the production of the nanoparticles, it is believed that the more reactive elements to oxygen always transfer to the surface due to the presence of oxygen in air [65, 66].

For instance, previous work in our group performed by Feng *et al* [65, 66] demonstrated that Cu-Au core-shell nanoparticles can be generated and the final morphology of the nanoparticles can be controlled using production parameters. When the Ar and He gas flow were roughly equal a Au core and Cu shell nanoparticle was observed in figure 2.12(a). Figure 2.12(c) demonstrates the intensity line profile from the STEM HAADF image. However, reducing the He flow resulted to a Cu core and Au shell nanoparticle as shown in figure 2.12(b) with the line profile shown in figure 2.12(d).

The Au core and Cu shell structure was stable over a long period of time. In contrast, in the Cu core and Au shell structure the Cu atoms migrated to the surface over time and the morphology was changed to a Au core and Cu shell, this was due to the higher tendency of Cu atoms to react with oxygen, therefore the presence of the oxygen made the initial structure unstable.

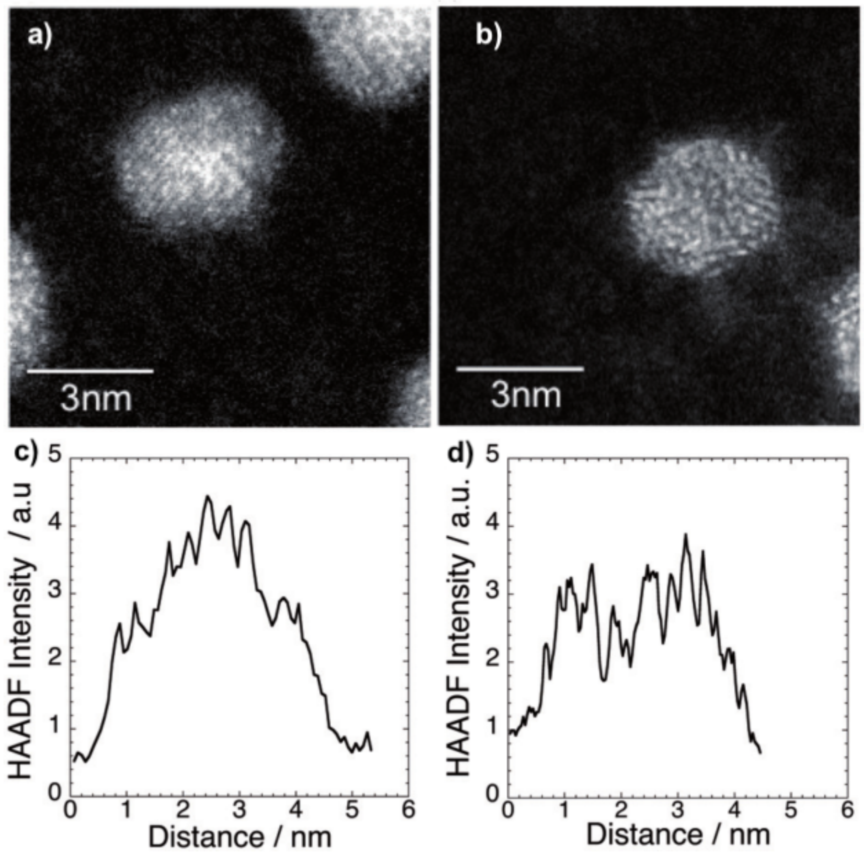

Figure 2.12: HAADF STEM images of Au-Cu nanoparticles produced with two different set of production parameters. (a) presents Au core with Cu shell (b) presents Cu core with Au shell, (c) and (d) are the intensity line profiles respectively. Both morphologies can be confirmed from the line profiles. Figure and caption from [66]

Oxygen effect on the morphology of nanoparticles is not always undesirable. The oxygen reaction with the nanoparticle can be used to derive the formation of a specific structure. For instance, Dai *et al* [67] demonstrated that the initially disordered structure of Pt_3Co nanoparticles can be changed to a Pt shell - Co core structure using thermal annealing under oxygen environment. The process took two steps, in the first step the disordered Pt_3Co nanoparticle changed to an ordered inter-metallic Pt_3Co structure while being annealed under the oxygen atmosphere. In this step,initial thin layer of Pt shell is formed through surface segregation. This thin layer effectively blocks Co oxidation. In the next step, the temperature is lowered, this allows the migration of Pt atoms from other nanoparticles to attach onto the Pt surface of the ordered Pt_3Co nanoparticles,

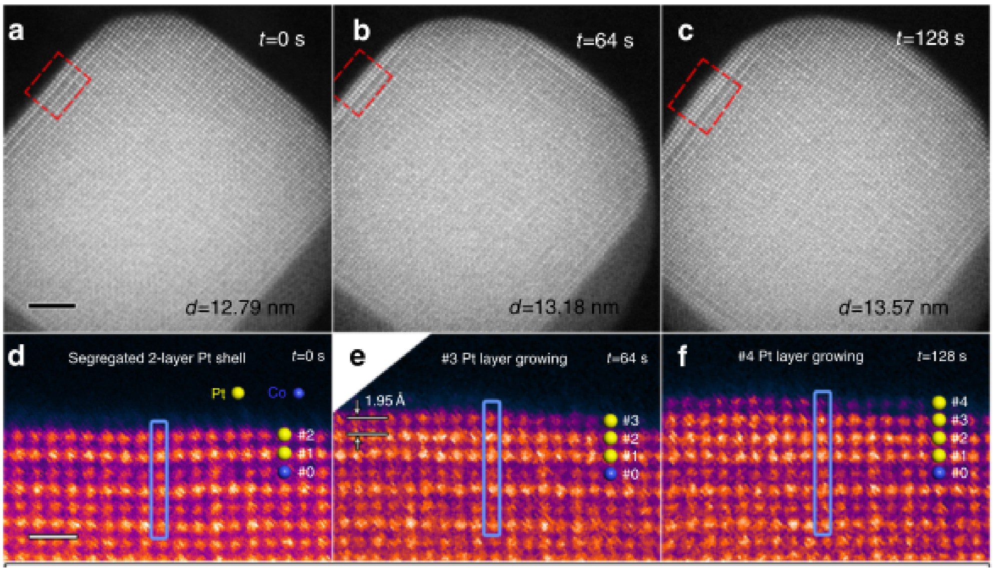

FIGURE 2.13: Layer by layer growth of Pt shell through annealing under oxygen atmosphere. (a)-(c) STEM images taken at 0, 64 and 128 while annealing at 300 C under oxygen, scale bar is 2 nm. (d)-(f) corresponding magnified surface of the nanoparticle. yellow marble presents Pt and blue marbles are Co. Figure and caption from [67]

resulting into further growth of Pt layer under the oxygen environment. The layer by layer growth process is demonstrated in figure 2.13.

The oxygen effect on the morphology of the nanoparticle and the use of oxygen to induce a specific structure has been discussed. However, it was seen annealing of nanoparticles can play a crucial role in the final morphology. The next section is focused on post processing through annealing of bimetallic nanoparticles.

2.3.3 Annealing Effect

Annealing of the bimetallic nanoparticles can induce morphology changes as well as enhance the properties. It is crucial to investigate the morphology of bimetallic nanoparticles, since most application of this type of particles involve operating at elevated temperatures, such as catalysis.

For instance, Keewah Chan *et al* [68], examined the annealing effects on the structure and optical properties of embedded Au nanoparticles in silicon suboxide films.

Au-SiO$_x$ films were produced through sputtering using a RF magnetron. It was observed that annealing the sample increases the diffusion of the embedded Au nanoparticles towards the surface of SiO$_x$ film. The surface plasmon resonance peak position and intensity could also be modified through annealing, since it is greatly affected by inter-particle distance and size of the Au nanoparticles on the surface.

The magnetic properties of core-shell nanoparticles with maghemite core and amorphous silica shell were also enhanced by annealing for 3 hrs at 300 C [69]. The enhancement was due to a decrease in the blocking temperature and the weakening of the inter-particle interactions. The thermal decomposition of the organic surfactant on the surface of the nanoparticle at elevated annealing temperatures results in the formation of amorphous carbon inside the nanoparticle.

The morphology of the bimetallic nanoparticles could also be determined through annealing. Guisbiers *et al* [70], investigated the response of Cu-Ni bimetallic nanoparticles to annealing. They performed the annealing during the synthesis through wet chemistry. Figure 2.14(b) demonstrates STEM image of as created nanoparticles, figure 2.14(d) shows the EDX line scan across the nanoparticle. It is clear that as created nanoparticles are in Janus structure. However when the annealing temperature increases a different morphology was observed. Figure 2.14(a) presents the nanoparticles synthesised at an elevated temperature, It can be seen from the EDX line profile in figure 2.14(c) that the morphology is in an alloy format. Therefore the final structure can be controlled through annealing in the synthesis process.

The invention of TEM and STEM holders capable of heating the nanoparticles under the electron beam has opened new doors into annealing effect on the nanoparticles. As such, one can follow precisely every step of the annealing experiment live with a precise control of the annealing temperature. For example, NiAu nanoparticles synthesised through wet chemical methods, have been heated under

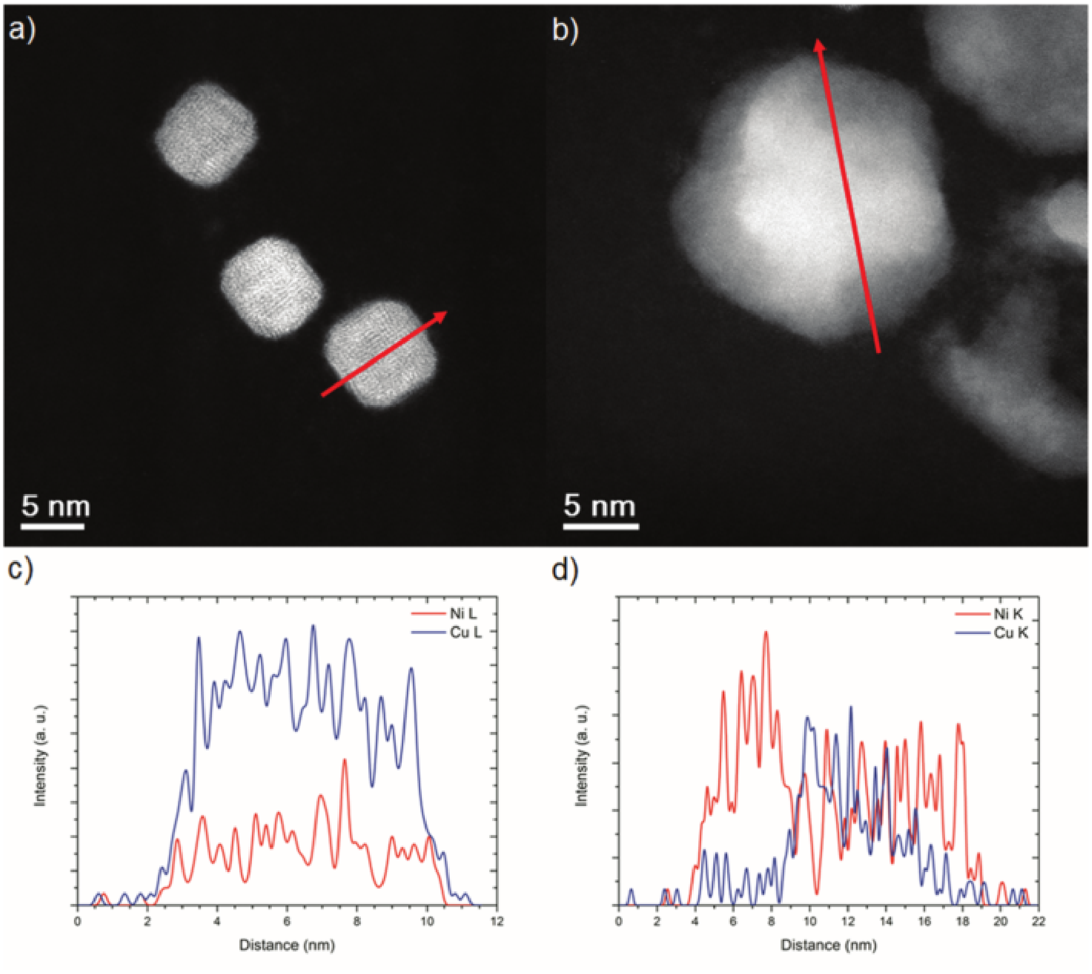

Figure 2.14: (a) STEM HAADF image of Cu-Ni nanoparticle in alloy configuration synthesised at elevated temperatures. (b) STEM HAADF image of Cu-Ni in janus structure. (c) and (d) present the EDX single line data as demonstrated by the red arrow of the nanoparticles. Figure and caption from [70]

.

the electron beam [71]. Figure 2.15 presents TEM of the nanoparticles at four different temperature. It was observed that to minimise their total energy during the annealing process, the particles undergo a sequence of thermal transformations. At temperatures below 250 ^{o}C, the core-shell morphology was stable, as the temperature increases to 250-300 ^{o}C the cobalt atoms in the shell begin to diffuse and reorganise to eliminate grain boundaries as seen in figure 2.15(a)-(b). As the annealing temperature was increased even further to 350 ^{o}C, the Au core begins to migrate to the side as seen in figure 2.15(d). Finally, when the heating

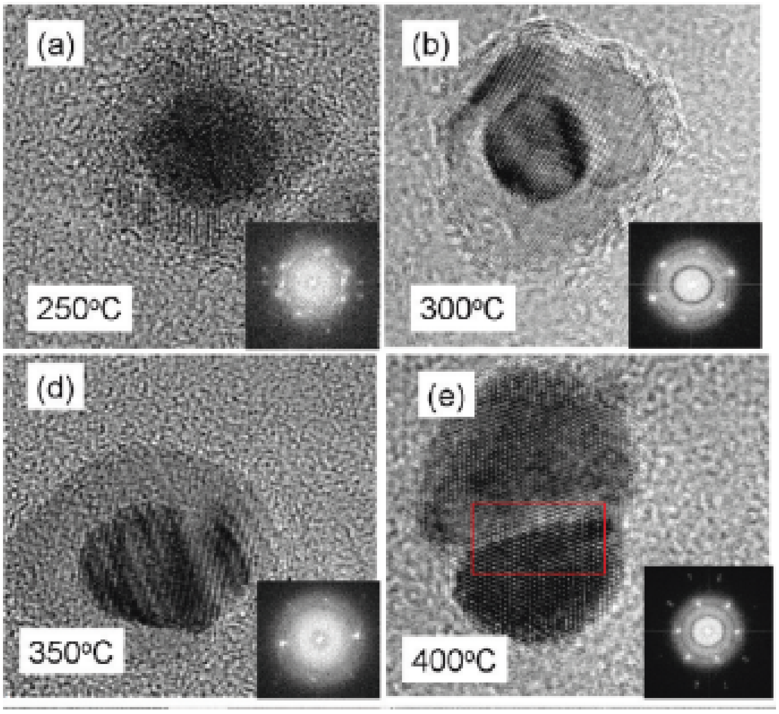

Figure 2.15: (a) Image of Au-Co nanoparticle in alloy configuration synthesised at elevated temperatures. (b)-(d) the cobalt atoms in the shell begin to diffuse and reorganise to eliminate grain boundaries . (e) the strain and interface energies are minimised by forming a segregated core-shell morphology. Figure and caption from [71]

temperature reaches to 400 °C, the strain and interface energies are minimised by forming a segregated core-shell morphology.

2.4 Electron Microscopy of Nanoparticles

The nanoparticles must be characterised in order to underpin their useful properties. This characterisation is mainly for the size and morphology of the nanoparticles, since these factors are crucial in determination of their properties. There are many new techniques that have been developed in the past decades to characterise nanoparticles, however electron beam microscopy techniques have proven to be the most powerful technique in nanoparticles characterisations. For instance, in High Angle Annular Dark Field (HAADF) imaging in the Scanning Transmission Electron Microscope (STEM) with aberration correction, the measured image

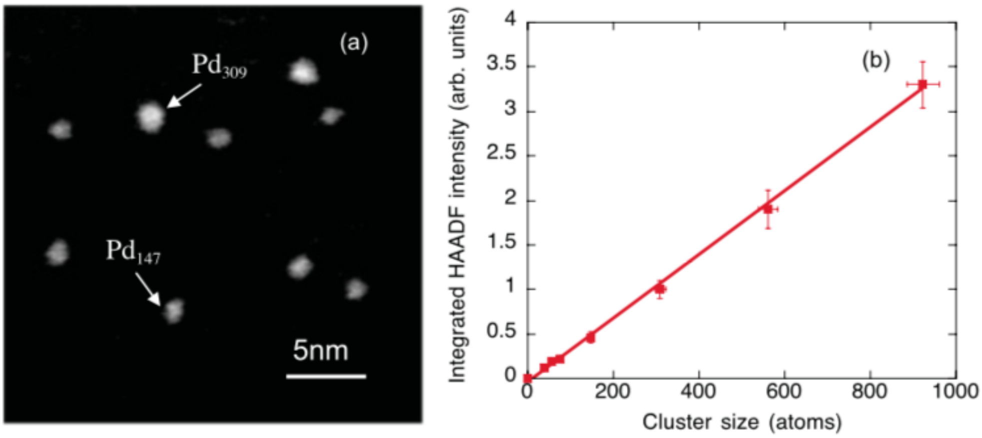

FIGURE 2.16: (a) HAADF-STEM images of a TEM grid simple with co-deposited Pd_{309} and Pd_{147}. (b) Integrated HAADF intensity over Pd nanoparticle against the cluster size. Figure and caption from [74]

intensity (I) has a simple relationship with the sample thickness (t) and atomic number (Z) [72].

$$I \sim tZ^{\alpha} \tag{2.5}$$

This relationship is valid in the limit of sufficiently thin samples. The exponent α is 2 for pure Rutherford scattering , this value is reduced by the electronic screening of the nuclear charge [73]. In practice, the value for this exponent depends on the microscope setup and the experimental parameters, such as the inner collection angle. The α exponent is crucial for chemical composition analysis in bimetallic nanoparticles. Sample thickness is difficult to determine inside the microscope, however, nanoparticles are ideal candidate for this purpose. Size-selected nanoparticles produced in our group have been used to calibrate the intensity of the HAADF-STEM microscope [72, 74]. Figure 2.16(a) presents a HAADF STEM image of a TEM grid with Pd_{309} and Pd_{147} co-deposited. The intensity contrast is clearly visible. Figure 2.16(b) presents a plot of HAADF intensity against the nanoparticle size, the linear relation is demonstrated as expected.

However, as it is well known the act of measurement on any system is likely to affect the state of the system. The electron beam effects on nanoparticles is no exception. It is essential to understand the effects of the electron beam on the nanoparticle in order to obtain an un-biased and true understanding of nanoparticles. The electron beam - nanoparticle interactions are believed to be through electron beam-induced heating effect, defect formation in the particles, charging of the particle and excitation of surrounding gases. However it is difficult to establish the dominating effect. This is still an ongoing debate in the scientific community [75, 76]. For instance, Wang *et al* [77] reported electron beam induced thickening of the protective oxide layer around Fe nanoparticles.

Fe nanoparticles with a thin layer of oxide were imaged with TEM for prolong periods of times. It was observed that the oxide layer around the Fe nanoparticle thickens as the imaging time increases, shown in figure 2.17. This effect was investigated in order to pin point which of the mentioned electron beam-nanoparticles interaction mechanism is the dominating factor for this phenomenon. When the electron beam was focused on only half of the nanoparticle the oxide layer only progressed where the electron beam was placed. This suggested that the effect cannot be due to heating since if that was the case, Fe is a good heat conductor therefore the oxide layer should thicken at all edges. The electron beam was also placed at the vicinity of the nanoparticle but the oxide layer did not thicken, this proved that the thickening is also not due to the excitation of surrounding gases. The team concluded that the thickening is not due to the temperature rise caused by electron bombardment, neither due to the charging of the particles nor ionisation of the oxygen. The thickening is dominated by the electron beam-induced defect mediated transport process.[77]

The electron beam induced morphology change of nanoparticles have also been investigated. It has been shown [78] that when Ag-Au nanoparticles were imaged under the electron beam for long period, the oxidation of Ag is accelerated and the

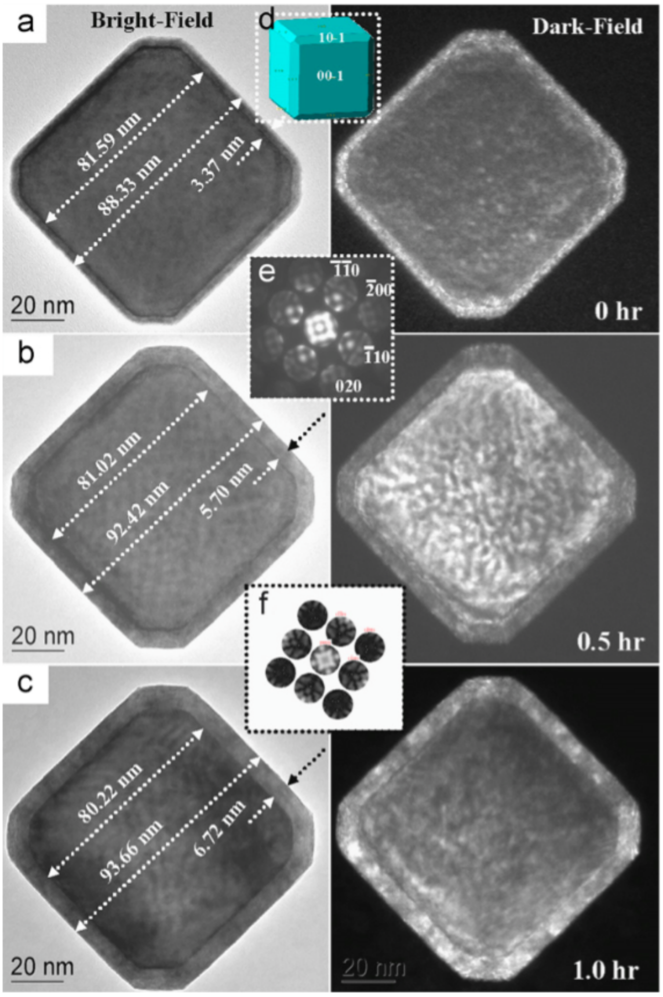

FIGURE 2.17: TEM images of Fe nanoparticles, bright field image on the left and the corresponding dark field image on the right. The images are taken at (a) 0, (b)0.5 and (c)1.0h. The progressive thickening of the oxide layer is clearly visible. (d) present 3D morphology of the nanoparticle. (e) and (f) show experimentally obtained CBED and computer simulated CBED. Figure and caption from [77]

morphology is changed from alloy structure to a hollow structure demonstrated in figure 2.18 (a to f) with Ag oxide as the outer shell and Au as the inner shell. In order to determine what aspect of the electron beam-nanoparticle interaction induces the morphology change, nanoparticles were heated *in situ* to temperatures up to 400 C. This resulted in small changes on the surface of the nanoparticle, however it retained its alloy morphology. This suggests that the morphology change is due to beam induced creation of oxidising species rather than beam induced heating of the sample.

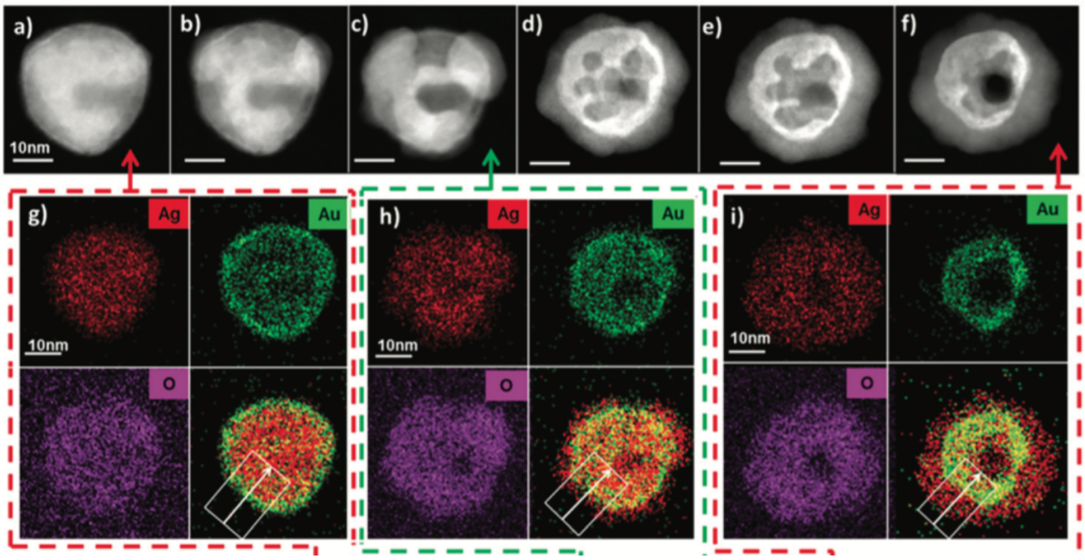

FIGURE 2.18: HAADF-STEM images of Au-Ag nanoparticles. It can be seen that the nanoparticle transforms from an alloy structure to a hollow Au-core Ag_2O shell structure, note the formation of a void in the centre i.e. the kirkendall effect.(g) to (i) EDX spectrum images at different stages showing the elemental composition and their distribution across the nanoparticle at different stages. Figure and caption from [78]

Other important phenomena observed under electron microscope is the coalescence of the nanoparticles induced by the electron beam. It has been demonstrated that many times in the literature [79–82]. For instance, Kumawat *et al* [83], demonstrated glutathione-capped red-fluorescent gold nanoparticles embedded on copper grid, transform into clean larger gold nanoparticles under high energy electron beam of Emission Gun Transmission Electron Microscope (FEG-TEM). Figure 2.19 shows merging of the two smaller nanoparticles under electron beam irradiation. The migration of grain boundaries through diffusion of atoms occurs in the nanoparticle with a loose crystal packing followed by coalescence and restructuring to form combined larger size Au nanoparticles. The organic ligand is removed by secondary electrons.

The organic ligand protection is weak and destroyed by the electron beam. However, Niu *et al* [84], from our group have demonstrated that mixing of Au with Ti to produce Au-Ti bimetallic nanoparticles reduced the sintering of nanoparticles

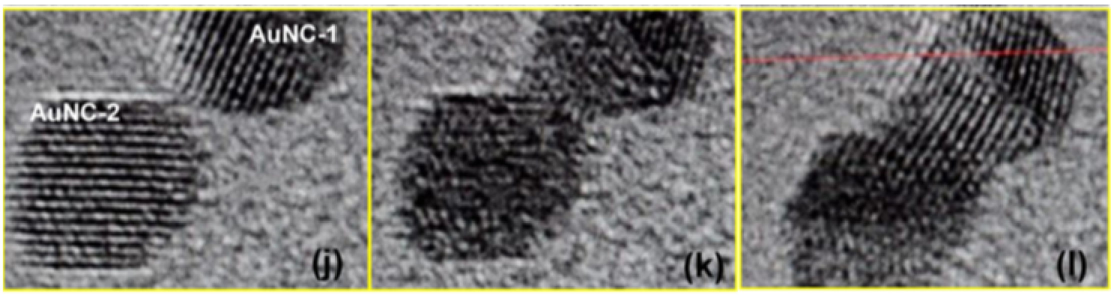

FIGURE 2.19: TEM image of Au nanoparticles being irradiated by the electron beam. (j) 30 s of irradiation (k) 31 s of irradiation and (l) 35 s of irradiation. The migration of grain boundaries through diffusion of atoms occurs in the nanoparticle with a loose crystal packing followed by coalescence and restructuring to form combined larger size Au nanoparticles. Figure and caption from [83]

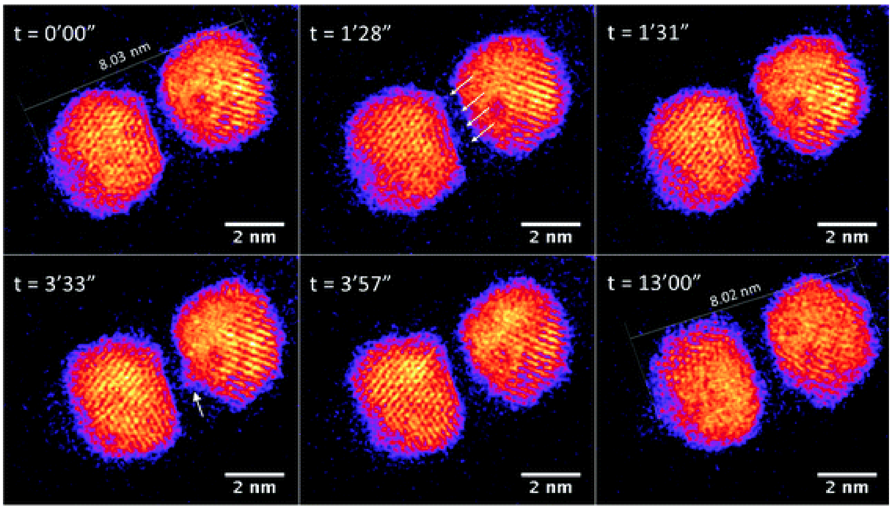

FIGURE 2.20: HAADF STEM images of bimetallic Au-Ti nanoparticles over time. The sintering process is significantly slower due to the reactive Ti in the nanoparticle. The time is shown on the top left side of each image. Figure and caption from [84]

under the electron beam on SiO_2 substrate. It was observed that pure nanoparticles coalesce quickly under the electron beam irradiation as one would expect. However bimetallic Au-Ti nanoparticles are significantly more stable. Figure 2.20 demonstrates HAADF STEM images of the bimetallic Au-Ti nanoparticles over a period of time. The bimetallic Au-Ti nanoparticles showed an anchoring effect against sintering due to the inclusion of highly reactive Ti atoms. It was concluded that this was mainly due to strong alloying of Ti to the SiO_2 substrate.

2.5 X-ray Photoelectron Spectroscopy of Nanoparticles

X-ray Photoelectron Spectroscopy (XPS) is a powerful tool to investigate the electronic and geometric structure of molecules, solids and surfaces [85]. The ever growing interest in nanostructured materials such as nanoparticles deposited on surfaces, due to their enhanced properties i.e. high catalytic activity, highlights the important question of how the XPS of deposited nanoparticles can be employed to obtain information about their electronic and geometric structure. The advantage of techniques such as XPS over electron microscopy is that the electron microscopy provides vast amount of information about a single or a few nanoparticles at a time, so in order to obtain a complete picture, great amount of acquisition and data analysis needs to be carried out. However, XPS is an ensemble method i.e. a great size of specimen can be investigated in a relatively short time scale. Obviously, each technique has its own strong points and can provide extra information to obtain a full understanding of nanoparticle properties.

2.5.1 Nanoparticle Size Effect on XPS

The XPS provides a direct insight into the electronic structure of the material. As the size approaches to smaller scale, i.e. nanoscale, the size of the nanoparticle has a direct and strong influence on the electronic structure, due to the strains induced within the nanoparticle and quantum effects becoming more relevant. Therefore, high sensitivity of XPS to changes in the electronic structure can be employed to probe the sample in ensemble. The most well known effect is the binding energy shift due to changes in nanoparticle size [86–89]. For instance, Lopez-Salido *et al* [87], investigated Ag nanoparticles grown on HOPG and characterised using Scanning Tunnelling Microscopy (STM) and XPS. It was observed that Ag 3d

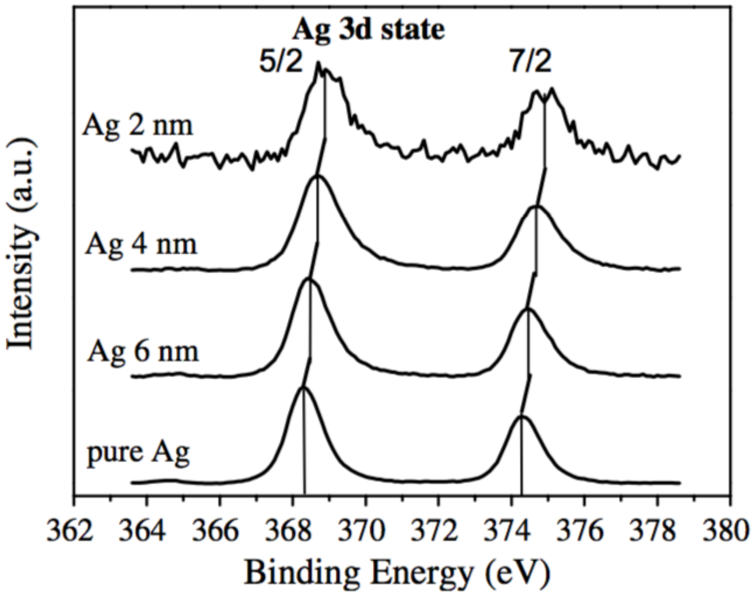

Figure 2.21: Ag 3d peak agains the size of the nanoparticles. The smaller nanoparticles the peak is shifted to higher energies, however as the particles sizes increases the binding energy approaches the bulk value. Figure and caption from [87]

states shift to the bulk states at a particles size of 6 nm and higher (shown in figure 2.21). However, this threshold value varies depending on the substrate as well as the particle geometry.

Similar study on Co nanoparticles on insulating supports, shows similar trend. Co nanoparticles on Al_2O_3 films were investigated for initial and final state shift as the nanoparticle size was increased [85]. Figure 2.22 demonstrate a plot of energy change for final and initial state against the particle size. It is clear that both values increase as the nanoparticle size increases, as expected. Theoretical analysis on the structure of the Co nanoparticles suggested the energy shift to be mainly due to a lattice contraction that is induced through growth process.

The broadening of the XPS peaks is also another phenomenon that depends on the nanoparticle size. For instance, Peters *et al* [86], study the size effect of small Au clusters between 1 to 34 atoms on silica substrate by XPS. An overall high energy shift of the 4f peak was observed, which increases linearly with inverse cluster radius. The liquid drop model explains such a behaviour through electrostatic final

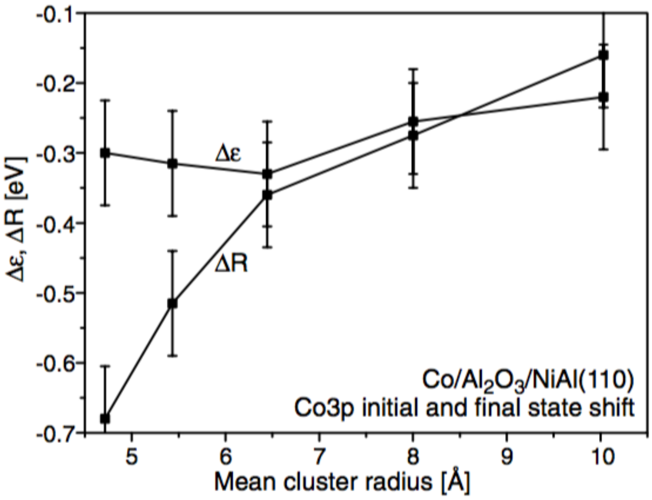

Figure 2.22: Co 3p initial $\Delta\epsilon$ and final state ΔR as a function of the mean cluster radius. Figure and caption from [85].

state effect. According to the model the positive charge remained on the cluster is confined by the small radius, hence interacts with the escaping photoelectron, on contrary, in the metallic bulk phase the charge is spread to an infinitely large volume. The broadening of the peak is demonstrated in figure 2.23. It was deduced that as the size of the nanoparticle decreases, the photon - nanoparticle interaction becomes more and more important, hence the broadening of the phonon broadening. The authors argue this is due to a final state effect, because according to the electrostatic drop model the positive charge left on the cluster is confined by the radius (R) and therefore interacts with the escaping photoelectron in contrast to the metallic bulk phase for which the charge is spread to an infinitely large volume.

The binding energy of a core electron of an element can be affected by the chemical bonding of that element. Qualitatively, the electrostatic interaction between the electrons is reduced by the electrostatic shielding of the nuclear charge from all other electrons in the atom. Removal or addition of electronic charge as a result of change in bonding also alters the shielding. Therefore withdrawal of valence electron charge i.e. oxidation, increases the binding energy and addition of valence electron charge, decreases the binding energy [90].

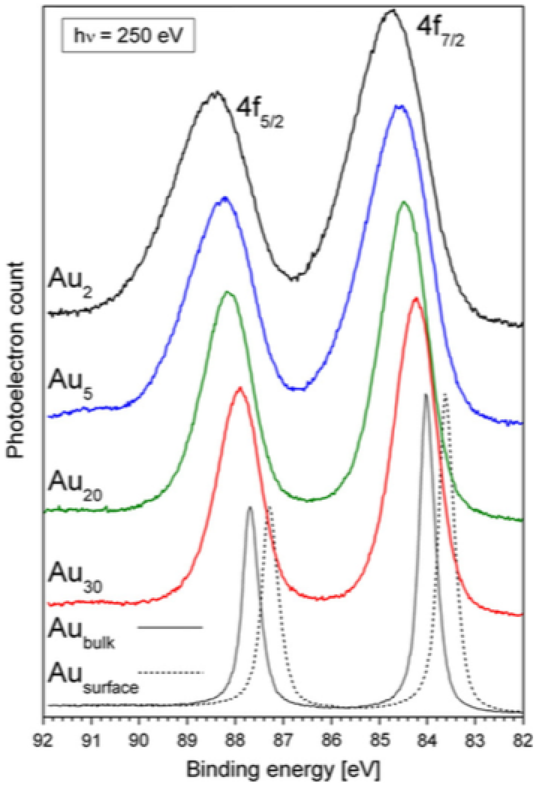

Figure 2.23: XPS spectra of Au clusters on silica. The peak position shifts to higher bonding energy as the cluster size decreases and the broadening of the peak is observed. Figure and caption from [86].

The sensitivity of XPS to chemical state of nanoparticles, makes the technique highly useful in chemical and reaction analysis. For instance, the interaction of Pt nanoparticles on TiO_2 substrate was investigated using XPS [91]. NO_2 was used to examine the reactivity of the nanoparticles to oxygen at room temperature. It was observed that initially the nanoparticle is in a subsurface/dissolved oxygen Pt-O_{sub} state, then it transformed into PtO and finally PtO_2. It was also observed that all three state of oxidised Pt nanoparticle can be reduced by annealing under vacuum. First PtO_2 is reduced to PtO and then Pt-O_{sub} and finally pure Pt. Figure 2.24 demonstrated the XPS spectra as the Pt nanoparticles were oxidised by exposure to NO_2 and then were reduced through heating under vacuum.

XPS has also proven to be a reliable technique for characterisation of core-shell nanoparticle [92–95]. For instance, it can be employed to establish the chemical

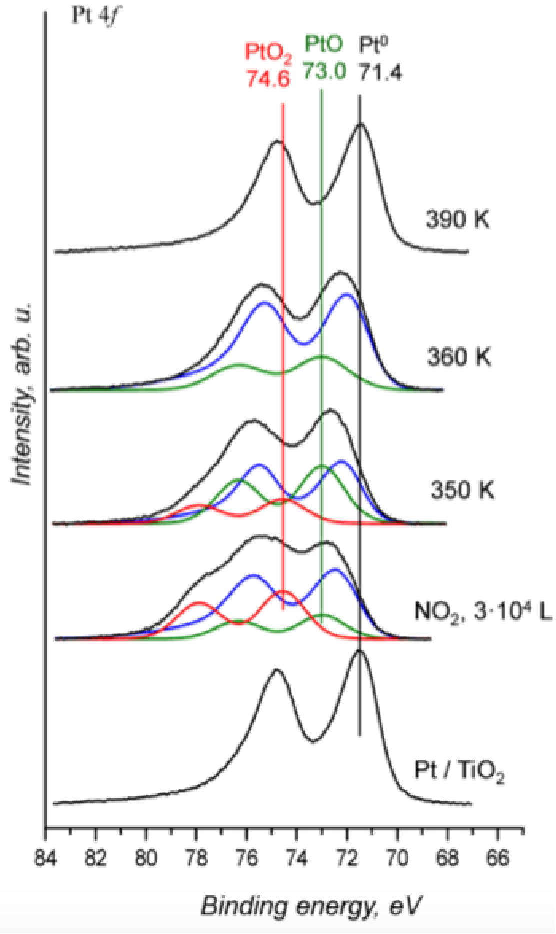

FIGURE 2.24: Pt 4f photoelectron spectra of the Pt/TiO_2 sample in the initial state and after corresponding exposures to NO_2 at different temperatures. Second derivatives of the functions describing the Pt $4f_{7/2}$ line. Figure and caption from [91].

state of the shell. Lewera *et al* [93], made advantage of this feature to report that the oxidation state of Pt-Ru nanoparticle can influence the catalytic activity of the nanoparticles. The chemical state of bimetallic AgNi nanoparticles was also investigated using XPS.

Chapter 3

Experimental Techniques

All the work presented in this thesis, was performed by mainly three pieces of equipment. Mass-selected nanoparticles were produced using a magnetron sputtering gas aggregation cluster source [96]. The samples were characterised using STEM and XPS. *In-situ* heating of the samples was performed by DENS Solutions Wildfire heating holder. In order to transfer the samples with minimum air exposure, a glove box was modified and filled with inert gas. In addition, a heating stage attached to the cluster source was used to heat the samples *in situ*. XPS located at the National Physical Laboratory (NPL) was used for the XPS analysis of the particles. The equipments used are explained in this chapter as well as the analysis techniques used to characterise the nanoparticles.

3.1 Magnetron Sputtering Gun Cluster Source

The magnetron sputtering gas-aggregation cluster source was employed to generate bimetallic Pt-Ti nanoparticles investigated in this thesis. The magnetron gun can be loaded with single or mixed metal target. For production of nanoparticles for this work, an alloy target of Pt-Ti was used. Figure 3.1 presents a schematic

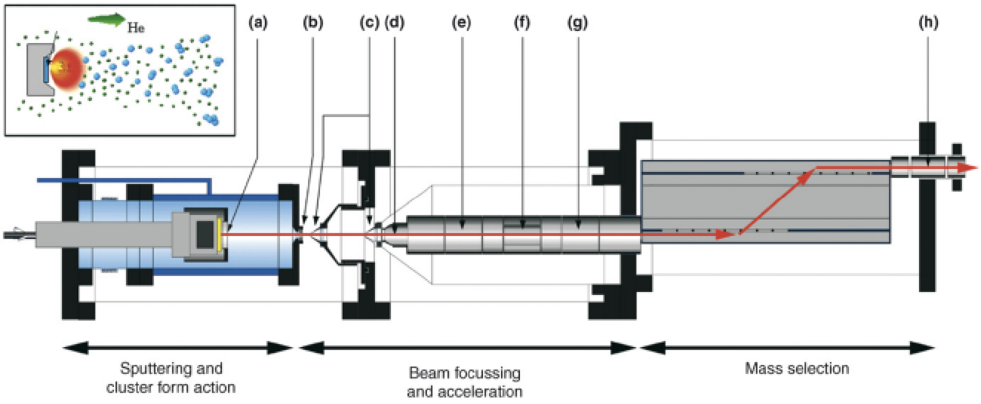

FIGURE 3.1: Schematic diagram of the Magnetron Gun Cluster source. (a) Metal target on the magnetron gun, (b) Adjustable nozzle, (c) skimmers, (d) high voltage lens, (e),(g) and (h) einzel lenses, (f) deflector plates for spatial control. Image adapted from [97].

diagram of the cluster source. The source consists of three main sections: (i) sputtering and cluster formation chamber, (ii) Ion optics and beam focussing chamber and (iii) time of flight based mass selection chamber. The cluster source is differentially pumped to pressures around 10^{-7} mbar. The cluster formation occurs in the inner first chamber of sputtering in addition to cluster formation chamber. This chamber is cooled with liquid nitrogen to enhance cluster formation of sputtered atoms. The second chamber consist of ion optics to accelerate and collimate the beam of clusters. The third chamber is known as the mass selection section, where the desired size of the nanoparticles is selected for deposition. The vacuum is achieved and maintained through continuous operation of the rotary and turbo pumps. The rotary pumps are capable of achieving 10^{-3} mbar and turbo pumps bring the pressure further down to 10^{-7} mbar. The pressures was also continuously monitored by using pirani and penning gauges.

3.1.1 Magnetron Sputtering and Gas Condensation

A commercially available magnetron gun is used for sputtering. A target material, for instance Pt-Ti in Figure 5.1 is inserted in the chamber. Ar gas is injected through a small inlet into the chamber, an Ar plasma is created in front of the target by applying a RF or DC high voltage.[96] For Pt-Ti target a DC voltage was used. A dense vapour of atomic ions and small clusters is formed in front of the target. The plasma potential is slightly more positive than the positive confining surface due to the screening effect therefore a large electric field is created between the biased target and the plasma to accelerate Ar ions sputtering. The cluster formation is enhanced further in this vapour by injecting He gas into the chamber. Both the Ar and He gas flow are regulated. The gas mixture containing clusters leaves the inner chamber of this section through an adjustable nozzle indicated as (b) in figure 5.1. The clusters-gas mixtures undergoes a supersonic expansion by going through two conical skimmers indicated by (c) before entering the ion optics chamber. The advantage of plasma sputtering techniques over other methods is that since the clusters are created in plasma a significant portion of the clusters are ionised therefore no further ionisation is needed.

A magnet is placed behind the target to intensify the plasma and enhance ionisation. Alloy Pt-Ti target, supplied by PI-KEM with purity of 99.95% was used for this work. The Pt to Ti mass ratio was 25% to 75%,corresponding to 13 Ti atoms for every Pt atom. The helium atoms act as the third body in a three body collision, so that the excess kinetic energy of the metal atoms are dissipated and aggregates are formed. Liquid nitrogen is also used to cool the plasma further so the aggregation is more efficient.

3.1.2 Ion Optics

A well formed cluster beam is crucial for mass selection and deposition. The cluster source is designed to measure positively charged particles therefore a negative biased voltage is applied to the ion optics lenses. After entering the ion optics chamber the beam is accelerated by the extraction lens (d) to a high voltage. The cluster beam is focused at two stages (e) and (g) by a pair of einzel lenses into the time of flight mass selector. A set of deflection plates (f) is used to adjust the trajectory of the beam entering the mass selection chamber.

3.1.3 Time of Flight (ToF) Mass Selection

The principal behind the ToF is previously discussed by Issendorff *et al* [98]. Here the summary in the form of a basic idea is presented. The idea is to displace the well focused cluster ion beam laterally by accelerating a portion of the beam perpendicular to its initial direction. This is achieved by applying a pulsed electric field, enabling the beam to drift in the perpendicular direction for some time. Later the perpendicular movement is stopped by applying an electric pulse in the opposite direction. The lateral displacement of the ion beam depends on the magnitude and timing of the electric pulse and also on the mass of the ions. Therefore in this way the ions with different masses are dispersed into parallel beams with different displacements. A small exit aperture can be used to only select a small portion of the mass distribution of the beam.

The necessary parameters required to describe the process are presented in figure 3.2. This process requires a homogenous electric field, therefore the length l determined by the opening in plate 2 only allows ions that experience the homogeneous field to pass throw i.e. ions which experienced the distorted field just before the opening are blocked. This is length s of the cluster beam in addition to the clusters that enter the chamber while accelerating, also deflected onto plate 2. Distance a which is the distance covered by ions during the acceleration should be large enough so that the selected cluster size does not reach plate 2. On the other hand it should not be much smaller than *d1* between plates 1 and 2 so that too high voltage is not needed for the pulse.

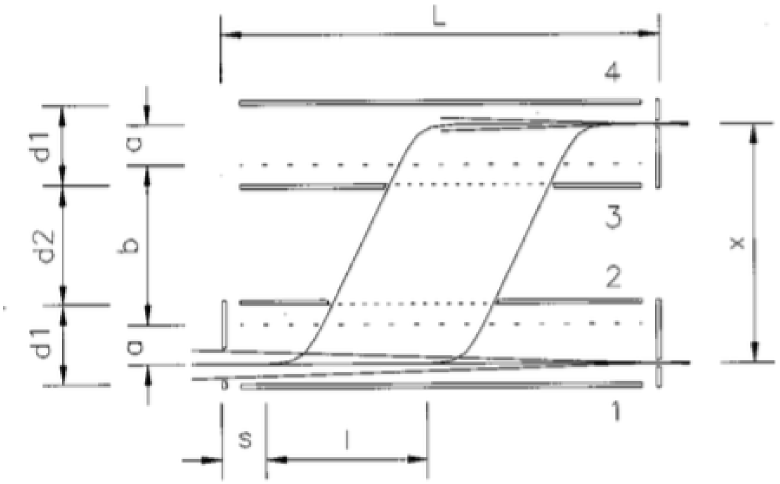

Figure 3.2: Schematic diagram of the mass selector. Plates 1 and 4 are used to apply short voltages pulses so that the ion beam drifts in vertical direction. l: length of displacement, x: total displacement, b: field free region, a: beam offset traveresed during high voltage pulse, *d1-d2*: plate separations, s: blocked portion of the beam due to field distortion, L total length. Image adapted [98]

The resolving power achieved by the mass selector attached to the cluster source is derived from the mass dependence of the vertical displacement. If m_o and v_{m_o} are the mass and the perpendicular velocity of the transmitted ions, an ion with mass m acquires the velocity:

$$v_m = v_{m_o} \frac{m_o}{m} \tag{3.1}$$

The lateral displacement is then calculated using the known values for the voltage pulse time and also the total displacement of the transmitted ions x. The exit aperture only allows certain range of masses Δm pass, out of the laterally dispersed mass distribution. If the full width half maximum of the convolution of the exit slit opening and the ion beam profile is defined as Δx then the mass resolution is given by

$$R = \frac{m}{\Delta m} = \frac{x}{\Delta x} \tag{3.2}$$

Therefore the resolution depends on the ratio of the lateral displacement and the exit slit width. [98]. The vertical displacement in the mass selector used for this work was 180 mm and the exit aperture was set to 8 mm.

3.1.4 Deposition

Finally the size-selected nanoparticle beam enters the deposition chamber where the particles are deposited on the desired surface. The deposition energy can be controlled through applying a bias voltage to the deposition stage. Three deposition regimes have been investigated before [99] soft-landing, pinning and implantation. The soft-landing of nanoparticle is achieved by low deposition energies around 1 eV per atom, this regime avoids fragmentation of the nanoparticle however the particles are free to move around at room temperature. The pinning can be achieved by deposition at the pinning energy threshold which results in self-pinning of the clusters due to creation of surface defects. Implantation can be achieved by deposition at energies much higher than that of the pinning energy. In this work the Pt-Ti nanoparticles were deposited with 500 V applied to the deposition stage which corresponds to the soft-landing regime. Therefore the nanoparticles are assumed to retain as created structure. The nanoparticles were deposited on Cu TEM grids with amorphous Carbon film for STEM and for the XPS samples, nanoparticles were deposited on Si and HOPG. The samples are loaded and unloaded through a load lock. This enables the user to transfer and store the samples with minimum air exposure.

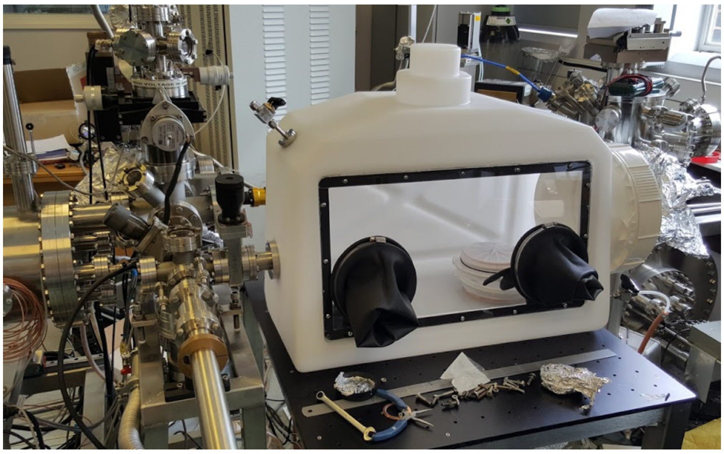

Figure 3.3: The glove box used to transfer the sample from the cluster source to the STEM room.

3.1.5 Mobile Inert Atmosphere Glove Box

In order to prevent oxidation of the nanoparticles, it was necessary to transfer the samples under an inert gas. A small size glove box was purchased from Sigma Aldrich and was modified. Figure 3.3 presents a picture of the glove box in the lab.

The glove box was modified so that it can be attached to the cluster source directly through a gate valve. Inlet and outlet valves were also installed to flow an inert gas into the glove box. Argon gas was used to fill the box before sample transfer. The Ar flow was started about an hour before the transfer.The oxygen level was measured using an Oxygen detector inside the box. The samples were taken out of the cluster source and placed on the STEM arm inside the box. The glove box was detached from the connections and taken to the STEM room. Samples were exposed to the atmosphere for a brief time when taken out of the glove box to insert in the STEM. Therefore it is reasonable to assume that the nanoparticles formed a thin oxide surface.

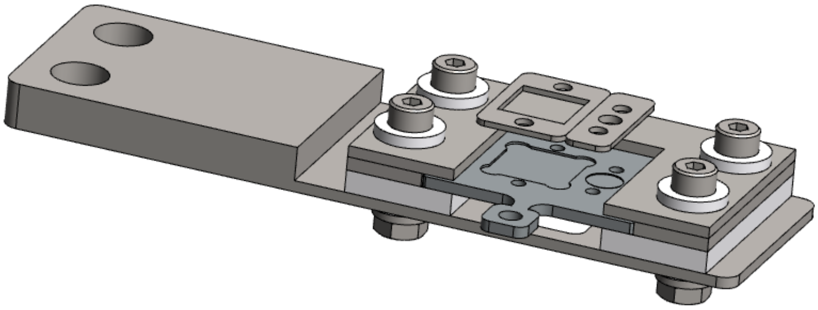

Figure 3.4: A systematic diagram of the electron bombardment annealing stage.

3.1.6 Annealing Setup

Electron bombardment heating stage was developed to anneal the samples *in situ* after deposition. The thermal stage was placed in a different chamber attached to the deposition chamber. The sample could be moved using a linear transfer drive to the annealing stage. The electron bombardment was achieved by allowing 3.5A current with 9.8 V through a wire behind the sample stage and applying a bias voltage of 500V between the wire and the sample stage to reach temperatures of up to 900 ^{o}C Figure 3.4. The temperature reading was done using a thermocouple attached to the vicinity of the sample and also a high temperature pyrometer. The annealing temperature could be controlled by adjusting the parameters. The annealing time was 20 minutes.

3.2 Scanning Transmission Electron Microscopy

The STEM mainly consists of electron source, lenses, aberration corrector and imaging system. Figure 3.5 presents an image of the C_s corrected JEOL 2100F

Figure 3.5: The C_s corrected JEOL 2100F STEM, capable of producing 200 keV electron beam.

STEM used in this work.

The advantage of electron beam techniques is that the electrons are an ionising radiation, therefore the electron beam is capable of removing tightly bound inner-shell electron from the atom by transferring some of its energy to the atoms in the specimen. This strong interaction results in a wide range of secondary signals from the specimens which could be detected and analysed. Some of these signals are presented on figure 3.6.

The STEM used for this work is also capable of performing electron energy-loss spectrometry (EELS) and X-ray energy-dispersive spectrometry (XEDS). Both these methods use the secondary signals to obtain chemical information about the sample being imaged.

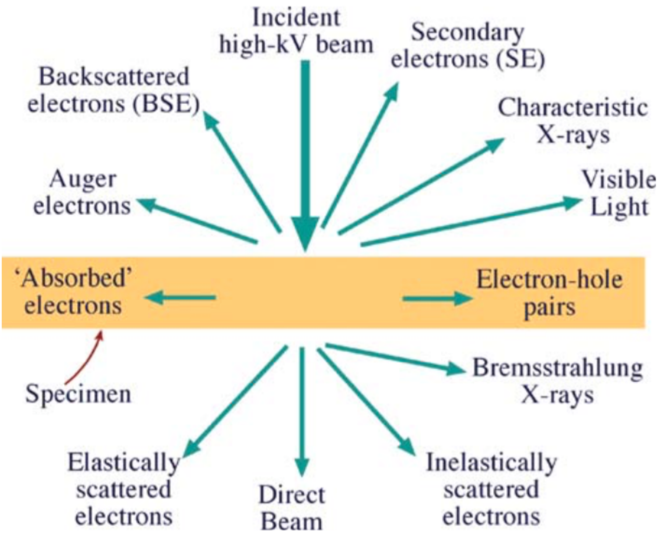

FIGURE 3.6: Signals generated as a result of high energy electron beam interacting with a relatively thin specimen.Figure and caption from [100]

3.2.1 Electron Source

The quality of the electron beam is crucial, since in order to obtain the best signal from the specimen, the input signal must be fine tuned. There are mainly two types of electron sources: thermionic source and field-emission source. In thermionic sources as the name suggested the electrons are emitted as the source is heated. The second type, field-emission source generates electrons by applying a strong electric field between the source and an anode. The heating and field-emission method can be combined together to produce Schottky source which is the source in the STEM used for this work, in short the Schottky source is called the electron gun.

In thermionic gun, the heating of the source overcomes the workfunction needed to the electrons to leave the source. Generally this type of sources are cheaper to maintain and easier to run. On the other hand the field emission guns (FEG) produce better monochromatic electrons. In FEG a cathode is made with respect to two anodes. The first anode is charged positively with a few kV to extract the electrons from the tip. This increase in the electric field must be done slowly in

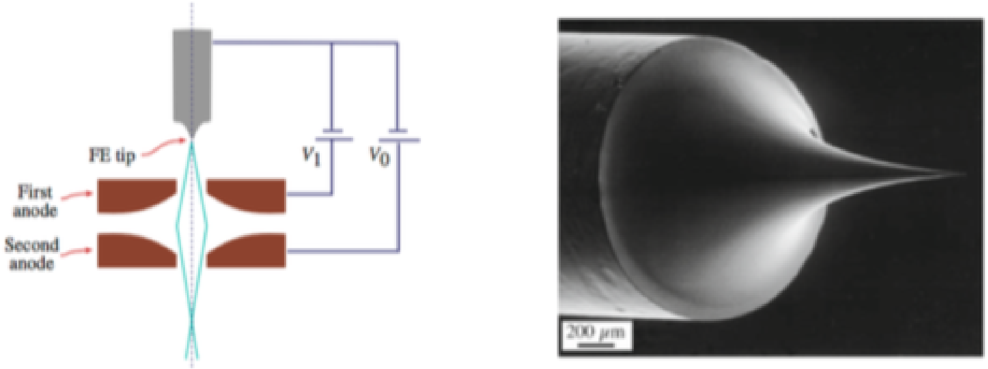

(a) Electron path for a FEG

(b) a FEG tip

FIGURE 3.7: The field-emission gun tip with a diagram of the electron paths showing the two anodes needed to form the electron beam. Figure and caption from [100]

order to avoid thermo-mechanical shock to the gun that could potentially fracture the tip [100]. Figure 3.7 presents an image of the FEG tip and also a simple diagram for the beam generation.

The electrons extracted from the tip using the first anode are then accelerated to higher voltages through the second anode. These two anodes also act as the first set of electrostatic lens to refine the electrons into a beam. The FEG sources are maintained and used under ultra high vacuum conditions in order to keep the tip surface clean, however due to the build up of contamination on the surface even in UHV conditions the gun needs to be flashed to remove the contaminant. This problem does not exist with Schottky FEGs as they are continuously heated during operation. The beam current and the acceleration voltage for the JEOL F2100 microscope used for this experiment were 170 μA emission current on average with 200 kV acceleration voltage.

3.2.2 Lenses and Aberration Correction

Magnetic lenses are used to form an electron beam. Figure 3.8 demonstrate a diagram of the magnetic lens. It consists of a cylindrically symmetrical core made of magnetically soft material such as iron. This core is called the polepiece. Then a hole is drilled through the Fe core that is called the bore. The second part of the lens is a coil of copper wire which is wrapped around the Fe core. When there is a current going through the Cu foil a magnetic field is created in the bore. The lenses must be cooled since the resistance of the current produces heat. The electron beam trajectory can be controlled through varying the strength of this magnetic field.

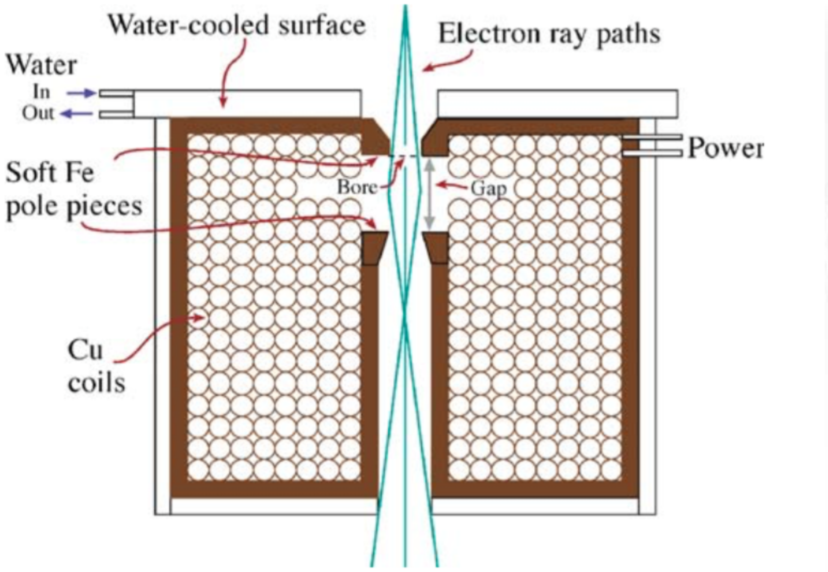

Figure 3.8: Schematic diagram of a magnetic lens.Figure and caption from [100]

Similar to real lenses the magnetic lens is also prone to many kinds of defects, the main defects compromising the image quality in microscopes are spherical aberration, chromatic aberration and astigmatism. The spherical aberration correction (C_s) is explained, this feature of the JEOL F2100 is the most unique feature available to this experiment. Figure 3.9 presents a diagram of the spherical aberration defect in the lens. Spherical aberration is caused when the lens bends the rays that go through the lens further away from the optic axis more strongly than those close to the axis. This will result in a disk shaped image of the point source in the plane of least confusion and a larger disk image in the Gaussian-image plane.

This effect can be compensated by applying a negative C_s to the beam after the lens which is perfomed in the C_s correction part of the STEM.

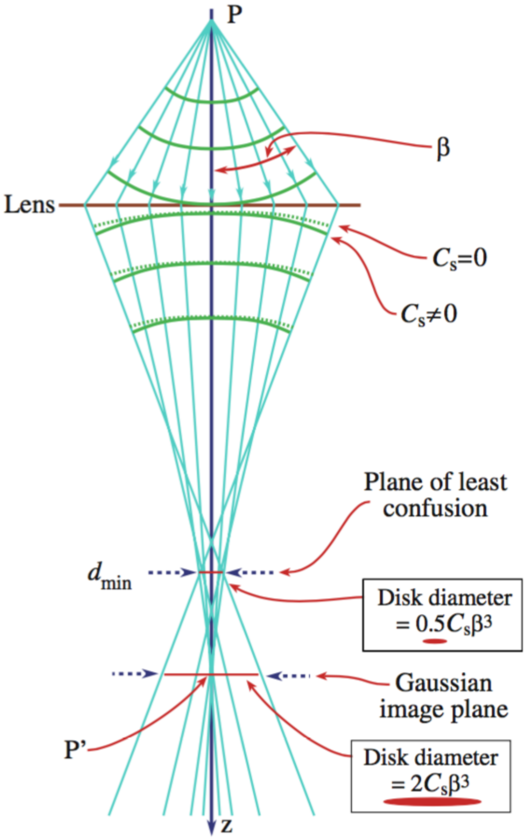

Figure 3.9: Spherical aberration effect when a beam passes through a lens. This can be compensated by applying a negative C_s correction. Figure and caption from [100]

3.2.3 Imaging System

Unlike TEM where the electron beam is static, the STEM images the surface by focusing the electron beam onto a point and scanning the surface pixel by pixel.The electrons interact with the specimen and are detected after the interaction. These interactions could be either weak elastic interactions resulting in small angle elastic scattering or strong inelastic interactions resulting in higher angle inelastic scattering of the electrons. Figure 3.10 presents different type of detectors used for collecting such scattered electrons. The Bright Field Detector (BF) detects elastically scattered electron that are scattered under small angles.

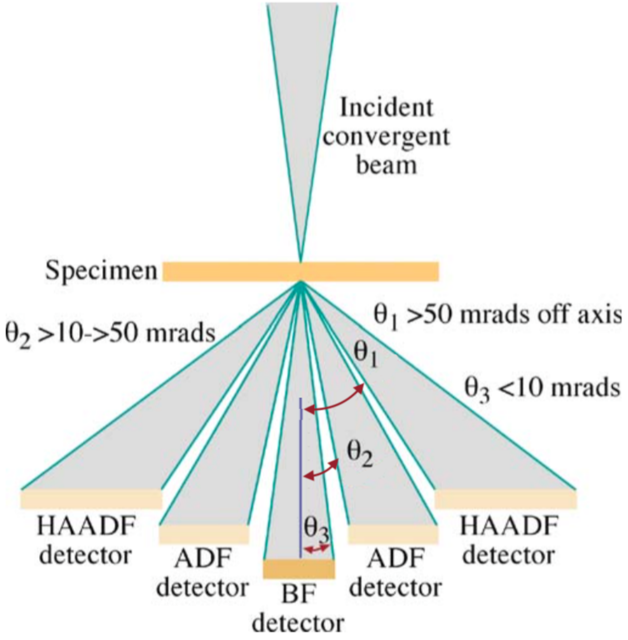

Figure 3.10: Schematic diagram of detectors in STEM.Figure and caption from [100]

On the other hand the Annular Dark Field detector (ADF) is positioned to detect inelasticly scattered electrons at higher angles. High Angle Annular Dark Field (HAADF) detector that is capable of detecting even more strongly scattered electrons. Since the interaction is stronger when it is inelastic, HAADF images provide a much better contrast and resolution compared to the BF imaging. The HAADF detector was used for imaging Pt-Ti for this experiment. HAADF detector has the shape of a hollow disc, therefore it only detects scattered electrons within a specific range. This range can be adjusted using the camera length.

The maximum resolution of the microscope is determined mainly by electron energy i.e. acceleration voltage [100]. The resolution limit using the small angle approximation for the microscope is:

$$Resolution \approx 0.61 \times \lambda \tag{3.3}$$

The wavelength λ can be calculated using the De Broglie wavelength:

$$\lambda = \frac{h}{mv} \tag{3.4}$$

where h is the Planck's constant, m is the mass of the electron and v is velocity. The electron velocity can be calculated using:

$$v = \sqrt{\frac{2eV}{m}} \tag{3.5}$$

where V is the acceleration voltage and e is the electron charge. Finally, using equation 3.4 and addition of the relativistic effect the final equation becomes:

$$\lambda = \frac{h}{\sqrt{2meV}} \times \frac{1}{\sqrt{1+\frac{eV}{2mc^2}}} \tag{3.6}$$

Therefore, for 200 kV acceleration voltage the resolution would be 2.51 pm. This is the theoretical limit, the actual experimental value will be larger. It should be noted that there is a compromising relation between increasing the electron energy to obtain better resolution and the electron beam damage on the specimen.

The intensity collected by the detector is directly proportional to the Rutherford scattering cross section. The equation below shows the differential cross section for this high angle scattering:

$$\sigma_R(\theta) = \frac{e^4 Z^2}{16(4\pi\epsilon_0 E_o)^2} \frac{d\Omega}{sin^4\frac{\theta}{2}} \tag{3.7}$$

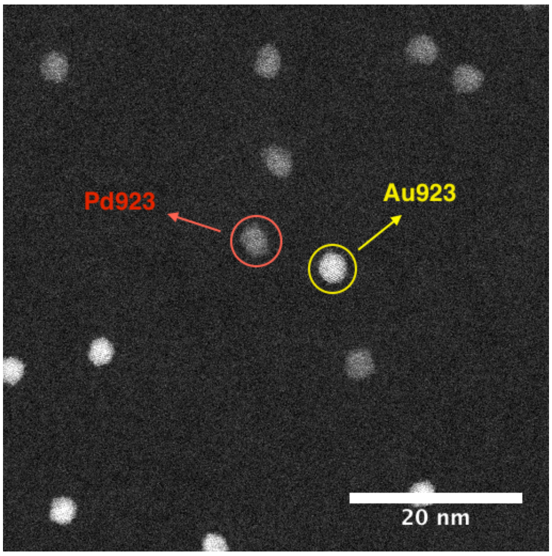

FIGURE 3.11: HAADF-STEM image of Au_{923} and Pd_{923} deposited on the same surface, the intensity difference is clearly visible.

Where e is electron charge, Z is atomic number, Ω is solid angle and E_0 is the electron energy. It can be seen that $\sigma \propto Z^2$, as a result:

$$I \propto (Z)^{\alpha} \tag{3.8}$$

where I is the HAADF STEM intensity. However in practice the value is not precisely two, due to the electron screen effect making the nucleus appear somewhat less positive.

It is crucial to calibrate HAADF intensity recorded by the STEM in order to relate intensity and atomic number. It has been demonstrated before that size-selected nanoparticle can be used to calibrate the intensity [101]. The intensity for 8 collection angles was calibrated as follow.

Au and Pd size selected nanoparticles with 923 atoms were deposited on the amorphous carbon film on copper TEM grid. Figure 3.11 shows a HAADF-STEM image of the sample. The intensity difference between the two nanoparticle is clearly visible, this is due to widely different atomic number(Au, 79 and Pd, 47).

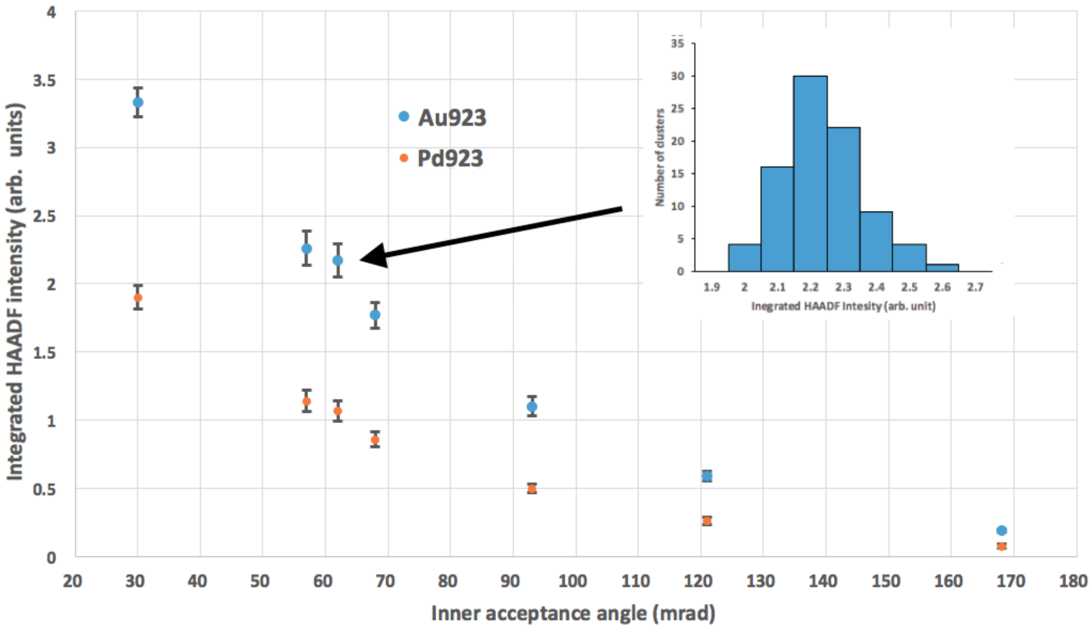

FIGURE 3.12: HAADF-STEM integrated intensity against the inner collection angles. It can be seen the intensity decreases with increasing collection angles. An example of the histograms is also provided.

The detector is a hollow plate of inside diameter 3 mm and outside diameter 8 mm. The inner collection angles are only mentioned when explaining the results since the outer collection angle can be caluclated using the geometry of the detector.

In total 8 inner acceptance angles were investigated, 20 HAADF-STEM images were taken with the same scanning parameters for all images (shown in figure 3.11) for each inner collection angle. A program was developed within Fiji to measure recorded total integrated HAADF intensity, subtracting the background for each nanoparticle. A histogram of these values was created for every inner collection angle for both Au_{923} and Pd_{923}. The peak value for each histogram was taken as the intensity for the cluster for that collection angle. Figure 3.12 presents a plot for all the intensity values against the inner acceptance angle, a histogram example is also given on the figure. The errors are the standard deviations obtained from histograms.

It is obvious that the signal intensity decreases as the collection angle increases. By taking the ratio of the integral intensity for Pd and Au, the exponent n in

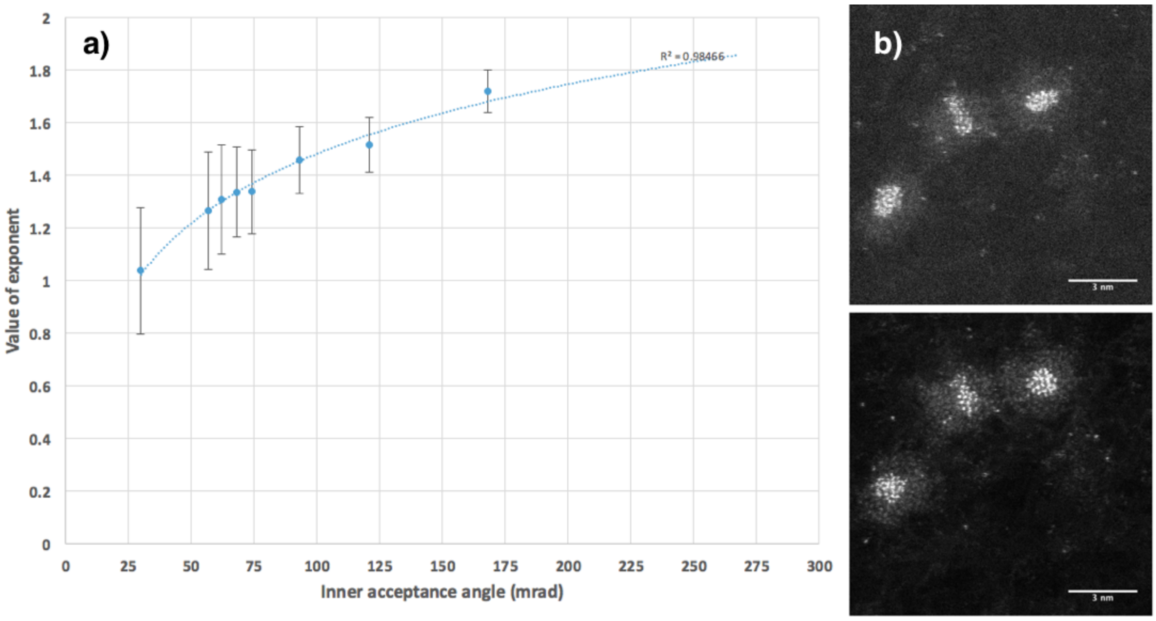

FIGURE 3.13: a) The value of the exponent α as a function of the inner collection angle. The solid line is a log fit on the data. b) 30000 amu Pt-TiO_2 clusters (bright core Pt, halo shell TiO_2), top is an image taken with inner collection angle of 62 mrad and bottom is 30 mrad, even though the exponent is closer to the theoretical value at higher collection angles but the image contrast is better at 30 mrad due to the higher signal-to-noise ratio.

equation 3.8 can be calculated. Figure 3.13 presents a plot of exponent n against inner acceptance angle. It can be seen that the value of n increases as the inner collection angle increases from 30 to 168 mrad. The solid line is a logarithmic fit on the data, which shows a reasonable fit with the least square fitting $R = 0.985$. The trend suggest that due to partially shielding of the bound electrons on the nucleus charge, this value is always smaller than the theoretical value of 2. It can also be deduced that the value gets closer to the perfect Rutherford scattering value of 2 as the collection angle increases. However it should be noted that for larger collection angles the signal-to-noise ratio decreases. Therefore, there is a compromise between Z contrast and signal-to-noise ratio.

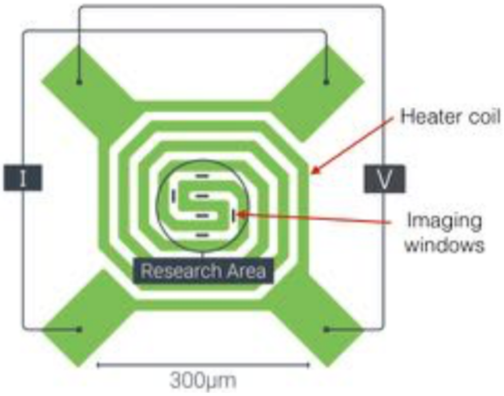

FIGURE 3.14: A diagram of the DENS solutions heater chip design demonstrating the contact points as well as the experiments windows where the temperature is uniform. Figure adapted from [102]

3.2.4 STEM In-Situ Heating

The thermal annealing under the electron beam was conducted using a DENS solutions wildfire heating holder. The DENS chip consist of a metal heater embedded in silicon nitride with imaging windows. The silicon nitride thickness is roughly 20 nm. Four connections are made to the the heating chip, two for power delivery and the other two connections for measurements. A diagram of the chip is presented in figure 3.14. Two contacts deliverying current and the voltage is measured through the other two connections to allow the resistance to be calculated. This provides an accurate method for temperature measurements as well as feedback control of the applied current to maintain a steady temperature. The initial calibration was done by the manufacturer and calibration values are provided to be entered in the control software. The software is also capable of recording the temperature log for analysis after the experiment.

3.3 X-ray Photoelectron Spectroscopy

X-ray Photoelectron Spectroscopy (XPS) is a standard technique used for surface analysis. XPS can provide quantitative information about the composition, chemical and electronic structure of a surface region of a sample. It takes advantage of the photoelectric effect, first introduced by A. Einstein in 1905 [103]. The method involves using a monochromatic electromagnetic radiation (photons) to excite bound electrons above the vacuum level. The intensity of emitted electrons over a range of kinetic energies are measured and spectra are obtained. the intensity peaks in the spectra can be identified to correspond to a specific electron shell of elements present and further analysis such as peak quantification and chemical state identification can be performed. The probing depth can be between 2 to 10 atomic layers [90].

3.3.1 The Principle of XPS

When the surface of the sample is irradiated by photons with sufficient energy, the excitation of electrons due to the photoelectric effect takes place. This process can be simply explained by the equation

$$E_{\gamma} = E_{kinetic} + E_{binding} + \phi \tag{3.9}$$

where E_{γ} is the energy of the photons, $E_{kinetic}$ is the kinetic energy of the emitted electron, $E_{binding}$ is the binding energy of the electron and ϕ is the work function of the material [104]. In order to simplify the calculation for the electron binding energy, normally an electrical contact between the sample and the spectrometer is made so that the Fermi levels of the two are at the same energy. The advantage of such a setup is that only the work function of the spectrometer need to be considered when calculating the binding energy. [104].

The excitation of electrons by the XPS process, results in production of Auger electrons. The Auger process takes place when a core electron leaves an atom through photoelectric effect and an empty state is formed. An electron from

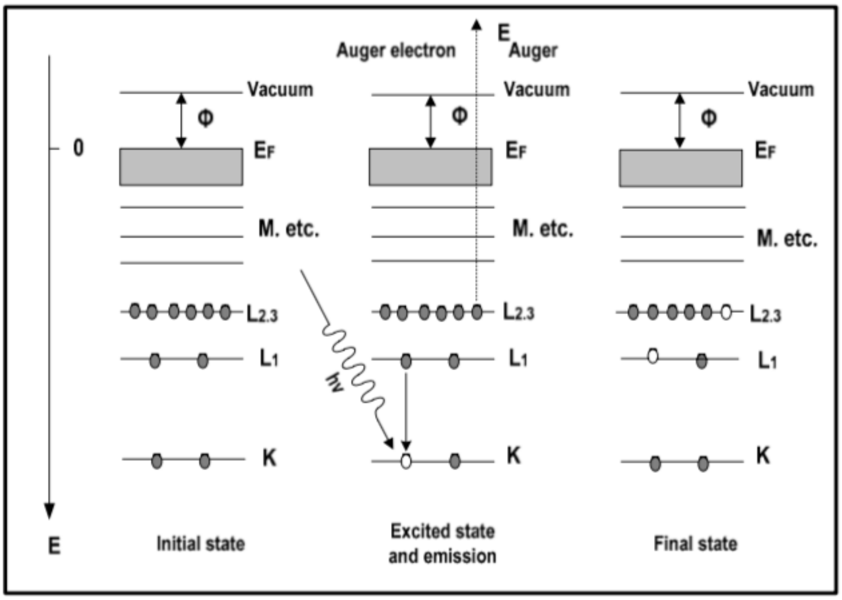

FIGURE 3.15: Energetic scheme of the Auger Process carried out using X-ray radiation. Left diagram demonstrate the initial state, then the ionisation process is demonstrated in the middle. One electron from a higher level drops to the vacancy in K level, the energy released is captured by the electron in $L_{2,4}$ level and is sufficient to expel the electron from the atom. On the right the final state of the atom is demonstrated, note the atom is doubly ionised. Figure and caption from [90, 105]

a higher electronic state then drops to the newly created empty state. As the electron originated from a higher energy state and is moving towards a higher potential, an amount of energy equal to the energy difference between the two state is released. This energy can either be emitted as a photon or excite another electron in to leave the atom. The process is demonstrated in figure 3.15.

The energy of the Auger electron is independent of the X-ray source and it purely depends on the specific atomic energy levels of the atom. The Auger peaks usually rise with broader and more complex structure than photoemission peaks.

The majority of the excited electrons experience inelastic collision as they are leaving the sample. Such electrons are known as secondary electrons, these electrons are the main source of the background signal observed in a spectrum. On the other hand, the electrons which do not experience inelastic collisions are known as primary electrons, such electrons provide the core information about the sample. This background signal can be removed by curve fitting, however, it may inevitably introduce some error in quantitative intensity determination and peak positions. The X-ray radiation employed in photoemission experiments has penetration depth orders of magnitude larger than the depth from which electrons can escape. Therefore the X-ray intensity is almost uniform across the depth of the sample where the primary electrons originate. The sample is then approximately considered as an electron source with fixed intensity, I_0 originating from a thin layer (d) of the sample which attenuate the emitted electrons [90]. Hence, the Beer's Law can be employed to describe the intensity loss over the depth of the sample

$$I_T = I_0 e^{-d/\lambda \cos\theta} \tag{3.10}$$

where I_T is the transmitted electron intensity, λ is the inelastic-mean-free-path (IMFP), and θ is the angle between the path of the electron and the normal to the sample surface. It can be deduced that the probing depth is primarily dependent on the IMFP within the specimen. This is defined as the depth of sample over which the photoelectron intensity is decreased to 1/e of its original value. Figure 3.16 presents a figure of electron kinetic energy against the IMPF. It is clear that this value is strongly dependent on the kinetic energy of the electrons.

It should be noted that over most of the energies probed by XPS, from 10 to 1500 eV, the electrons with higher kinetic energy are capable of further penetration. The significant increase of IMPF at values below 10 eV is most likely due to the fact that electrons lack the required energy to interact with valence electron plasmons, hence decreasing the probability of inelastic collision. Above the minimum at 50 eV, it can be concluded that electrons with higher kinetic energy will be detected from deeper depths. This is useful in depth profile analysis.

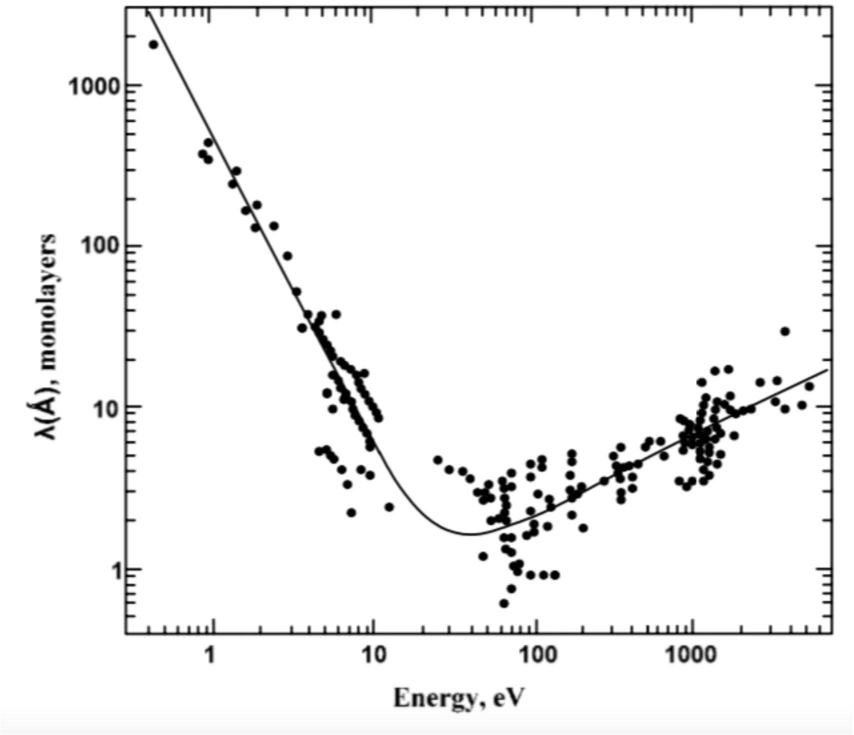

Figure 3.16: A plot demonstrating electron kinetic energy against inelastic-mean-free-path. Figure adapted from [90, 106]

3.3.2 Analysis

XPS spectra contain many information on the sample characteristics. As discussed previously, the background of the spectra is mainly a result of inelastic collision of the photoelectrons with the sample. Therefore, an increase in intensity towards the lower end of the spectrum is observed with a step increase after each recorded peak. The main photoelectron peaks can be fitted by a Lorentzian and a Gaussian lineshape. The Gaussian part depends on the instrumental factors and the Lorentzian contribution is from the core hole lifetime of the state. As a result, the full-width-half-maximum (FWHM) of the Lorentzian portion of the peak must be altered by an amount by the uncertainty principle

$$\Gamma \approx \frac{h}{\tau} \tag{3.11}$$

where Γ is the FWHM, h is the planck's constant, and τ is the core hole lifetime. Different chemical and electronic state of the elements being studied can often overlap, thus deconvolution is necessary to to analyse the proportion of various state in the spectrum. Normally, the process of fitting the peak is a lot easier using an automated fitting software such as CasaXPS. However, one needs to be careful as the fitting results do not always makes physical sense.

Another phenomena is the splitting of the peaks into doublets. This is due to the spin-orbit coupling of a certain state, the interaction between the electron's orbital angular momentum l, and its spin s. Based on quantum mechanics l can take any value of real integer up to $n-1$, where n is the electron shell number with sub-shell number s,p,d etc. The electron spin s is 1/2, thus the total angular momentum j of the electron is

$$j = \mid l \pm s \mid \tag{3.12}$$

Therefore, for l values greater than 0, the total angular momentum can take $l \pm 1/2$. The doublets occurs in ratios related to the degeneracy of the states, for instance for a p state, j can take values of 1/2 and 3/2 and degeneracy of $2j+1$, thus the peak valued will be in a ratio of 1:2. As the peak position and relative intensity is known, these values in addition to the FWHM can be used as constraints when fitting the XPS peaks.

Satellite peaks are unwanted features observed in XPS spectra. The satellite peaks are smaller copies of the primary peaks at fixed separation from them. They are caused by an X-ray source that is not monochromatic. A result of photoelectrons excited by additional characteristic lines from the X-ray anode. However, it is usually easy to remove them from the data and automatically done by the analysis software since their position and intensities in comparison to the primary peaks are well known.

3.3.3 XPS Setup

A typical laboratory XPS setup consist of an X-ray source, monochromator and an analyser. All the equipment must be attached to a chamber with base pressure at ultra-high vacuum ($\approx 10^{-9}$ mbar). This is to ensure the surface does note react during data acquisition. In simple terms, the X-ray gun is an electron emitting filament with an anode at the opposite end. The electrons are accelerated towards the anode and after the collision their energy is emitted as X-rays. The anodes are typically made of aluminium or magnesium. A dual anode configuration is also possible. This type of setup is useful for much easier identification of Auger peaks in the spectra, since the X-rays would have two different energies, 1253.6 eV for magnesium $K\alpha_{1,2}$ lines and 1486.6 eV from the aluminium $K\alpha_{1,2}$ lines. However since Auger peaks are independent of the X-ray energy, their position will be unchanged for both sources.

A monochromator is used to remove as much unwanted Bremsstrahlung radiation as possible as well as any characteristic lines other than the $K\alpha_1$ or even $K\alpha_{1,2}$ for a better signal to noise ratio. It normally consist of a quarts crystal with a well known diffraction pattern. Positioned at a specific point so that only radiation of the required wavelength is diffracted through the system. The XPS analyser is a complicated equipment since the accurate energy of the electrons must be measured. Most common analyser is a concentric hemispherical analyser (CHA). As it is implied by the name, two conductive hemispheres positioned concentrically to one another with each set to a specific potential. Photoelectrons are allowed to enter the space between the hemispheres through a small slit. Figure 3.17 demonstrate a diagram of the setup.

The potential between the plates deflects the electrons in a way that only electrons with a specific energy i.e. pass energy will be able to pass through the entire analyser to be detected and amplified by a channeltron or micro-channel plate.

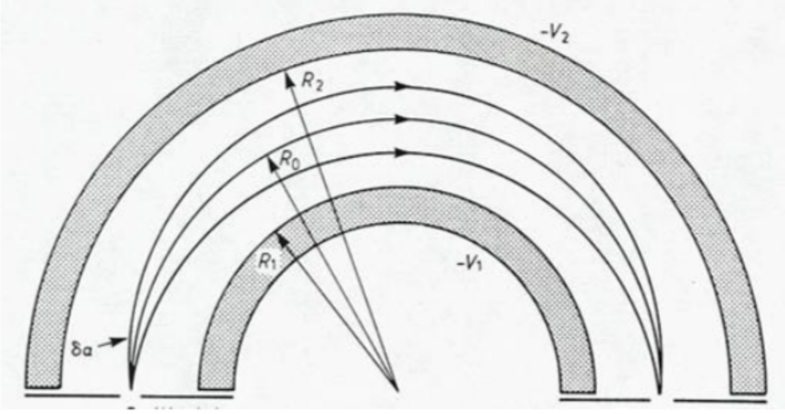

FIGURE 3.17: Cross sectional view of the concentric hemispherical analyser. R1 and R2 are the radii of the hemispheres and V1 and V2 are the potentials applied to them. Figure and caption from [90, 106]

These devices are electron multipliers , working very similarly to a standard photomultiplier tube. An electrostatic lens is then used to focus the electrons into the entrance of the analyser which also retards the electrons as they arrive. There are two methods for resolving the electron energy. The analyser can either operate at a fixed retardation potential and vary the potential of the hemispheres during a scan known as Fixed Retardation Rate (FRR) mode or the pass energy is kept fixed and the retardation potential can be varied known as Constant Analyser Energy (CAE) mode. CAE is more popular, mainly due to the fact that the relative energy resolution of the analysis is defined as

$$\frac{\Delta E}{E_\alpha} \tag{3.13}$$

where E_α is the energy of the electron at the point it passes through the analysis, therefore by keeping this value fixed, the energy resolution of the analyser also remains fixed.

Kratos Analytical AXIS X-ray XPS setup with an Aluminium source of Kα radiation with 1486.6 eV photon energy was used for this work. The pass energy was set to 20 eV for narrow scans and 120 eV for survey scans.

3.4 Sample Preparation

Copper TEM grids with amorphous carbon film or DENS heating Chips with SiNx films were used for the STEM analysis. The substrates were loaded into the load lock mounted on a flag style sample plate. The cluster source was tuned to obtain the highest nanoparticle current. The surface coverage was set between 5% to 10% depending on the sample, the coverage was controlled by the deposition time required for a specific coverage. The beam current was rastered across the substrate to ensure coverage uniformity.

For the samples which needed to be protected from oxidation, the mobile inert gas glove box discussed earlier, was used. It was attached to the load lock, filled with argon while oxygen level constantly monitored. The load lock was then vented using Ar and the samples were transferred into the box where then they were loaded on the STEM sample holder, either on the standard TEM grid single tilt holder or the DENS heating holder, depending on the experiment. The box was then carried to the STEM room, and the holder was inserted swiftly into the STEM column.

The best effort was made to keep the scanning parameters constant throughout the project, however minor adjustments were required to enhance image quality from session to session. The majority of the images were recorded with collection angle of 62 mrad to preserve consistency.

For the XPS samples, Si was the main substrate used, however the particles were also deposited on HOPG for the project. The substrate was sonicated in isopropanol (IPA) for 15 mins and then in acetone for another 15 mins to ensure cleanness of the substrate. The nanoparticles were the soft-landed on the substrate with coverage of 10% with rastering during deposition. The samples were then transferred to the National Physical Laboratory for XPS measurements. The XPS setup was capable of *in situ* thermal annealing samples to 600 C.

3.5 Data Analysis

FIJI [107] was used for data analysis of the HAADF STEM images, this includes statistics and videos for heating experiments. For detailed intensity and size distribution a plug-in for FIJI was written in Java programming language. The program was capable of measuring the approximate core and shell size of the Pt-Ti nanoparticles. Information such as total HAADF intensity for the core and shell as well as the background in the vicinity of the nanoparticle was provided. (see figure 3.18). The XPS data was analysed using CasaXPS [108]. The spin orbital splitting ratio between the doublet of electronic subshell f 5/2 and 7/2 is 3:4, therefore the ratio of areas between Pt $4f_{5/2}$ and Pt $4f_{7/2}$ peaks was constrained accordingly . The peak separation was constrained to 3.3 eV when fitting the Pt peaks. Similarly the spin orbital splitting ratio between the doublet of electronic subshell p 1/2 and 3/3 is 1:2, therefore the ratio of areas between Ti $2p_{1/2}$ and Ti $2p_{3/2}$ peaks was constrained accordingly . The peak separation was constrained to 5.7 eV when fitting the Ti peaks. Typical peak width for the Pt doublets and the Ti $2p_{3/2}$ was 1.2 ± 0.1 eV and for broader Ti $2p_{1/2}$, the peak width was 2.4 ± 0.2 eV.

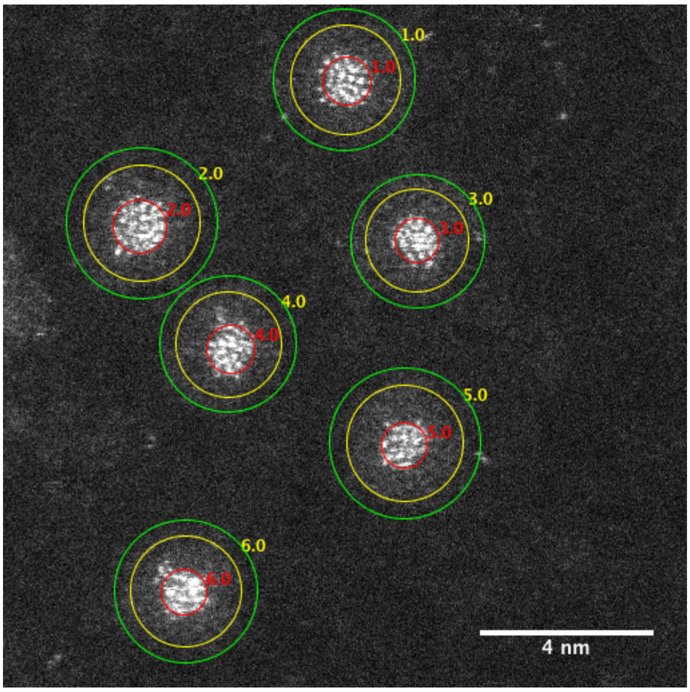

Figure 3.18: An example of the FIJI program output used for nanoparticle analysis. Red circle estimates the core size, yellow total nanoparticle size and green circle calculates the background in near vicinity of every nanoparticle. The values are then outputted in a text file for further data analysis.

Chapter 4

Oxidation Effect on Morphology of Pt-Ti Nanoparticles

4.1 Introduction

In this chapter, theoretical and experimental results of oxidation effect through air exposure on the morphology of Pt-Ti nanoparticles are presented. The magnetron gun sputtering cluster source with time-of-flight based mass filter was used to size select the nanoparticles. An inert gas transfer box was designed and built to transfer the samples with minimal air exposure. The study focuses on two particular masses of Pt-Ti nanoparticles, 30 kDa and 90 kDa. The chapter includes a brief description on the methodology of the experiments. The HAADF STEM images of fully oxidised samples are presented and discussed followed by results on surface oxidised Pt-Ti nanoparticles. A detailed description of the theoretical results are provided in order to obtain an in depth understanding of the system, followed by conclusions on comparison of the theoretical and experimental results.

The production of Pt-Ti samples, STEM imaging and data analysis was performed and designed by the author. The theoretical work was performed by Shih-Hsuan

Hung and Keith McKenna (Department of Physics, University of York), in collaboration with the author. The majority of the this work is already published by the author [109].

Morphology of bimetallic nanoparticles is strongly affected by oxidation of one or both metallic component. It is highly challenging to pin point the oxidation effect in both experimental and theoretical studies. The experimental work require careful handling and procedure to minimise oxygen exposure. The theoretical works generally require significant processing power to only apply the theoretical model to the two elements involved to determine nanoparticle structure, let alone introducing an extra element such as oxygen effect into the calculation. In this chapter, we have attempted to address to some extent both of these issues.

4.2 Method

Pt-Ti nanoparticles were created under vacuum through sputtering of the Pt-Ti alloy target with the ratio of 13 Ti atoms for every Pt atom within the condensation gas. A beam of nanoparticles was formed using ion optics and directed to the mass selector. Pt-Ti nanoparticles with two different masses i.e. 30 ± 2 kDa and 90 ± 5 kDa were selected and deposited through soft landing on copper TEM grids covered with amorphous carbon film. The sample coverage was kept at 5% to minimise coalescence between the particles. At least 10 samples were made throughout the project to ensure the repeatability of the results. To ensure full oxidation of the particles for oxidised samples, the samples were exposed to air for 24 hours. The samples were then transferred to the STEM and imaged. At least 100 nanoparticles were imaged on average to obtain enough data for analysis.

4.3 Morphology of Pt-Ti after Exposure to the Air

Figure 4.1 present HAADF STEM images of Pt-TiO_2 nanoparticles i.e. Pt-Ti nanoparticles after air exposure. In figure 4.1(a)-(b) 90 kDa nanoparticles are shown and 4.1(b)-(c) demonstrates smaller size 30 kDa nanoparticles. The grey halo in the images is the oxidised Ti shell, the Pt core is demonstrated by the bright central spot. The scattering intensity is strongly dependent on the atomic number Z of elements in HAADF imaging [101]. Figure 4.1(e) demonstrates the average line profile of the red rectangle in 4.1(c), where the background is carbon HAADF intensity, the shoulders are TiO_2 and carbon intensity and the main peak is TiO_2, Pt and carbon intensity. The large difference between the atomic number of Pt (78 amu) to Ti (22 amu), there is a significant contrast between Pt and Ti atoms. On the other hand, the low scattering intensity of Ti becomes an issue when compared to the carbon film, hence an ImageJ plugin was written in Java to quantify the core and shell size. The higher magnification images demonstrate the interior structure of both nanoparticles. The single core structure of 30 kDa Pt-Ti nanoparticle is clearly visible from the STEM images, a single bright core covered by TiO_2 shell. In contrast the 90 kDa nanoparticle demonstrates a multi-core structure with cores scattered around the centre of the nanoparticle and covered by TiO_2 shell.

Figure 4.2 presents a statistical analysis on the core and the total diameter size for 30 kDa and 90 kDa Pt-TiO_2 nanoparticles. Figure 4.2(a)-(b) presents (a) core and (b) shell size distribution for 30 kDa Pt-TiO_2, the core size was measured to be 1.0 ± 0.2 nm in diameter with a shell thickness of 0.8 ± 0.4 nm, resulting to a nanoparticle with diameter of 2.6 ± 0.8 nm. In 90 kDa nanoparticles, the program calculated a single core size of 0.9 ± 0.4 nm in diameter with a total diameter of 3.5 ± 1 nm, shown in figure 4.2(d)-(c). It was difficult to define a shell thickness

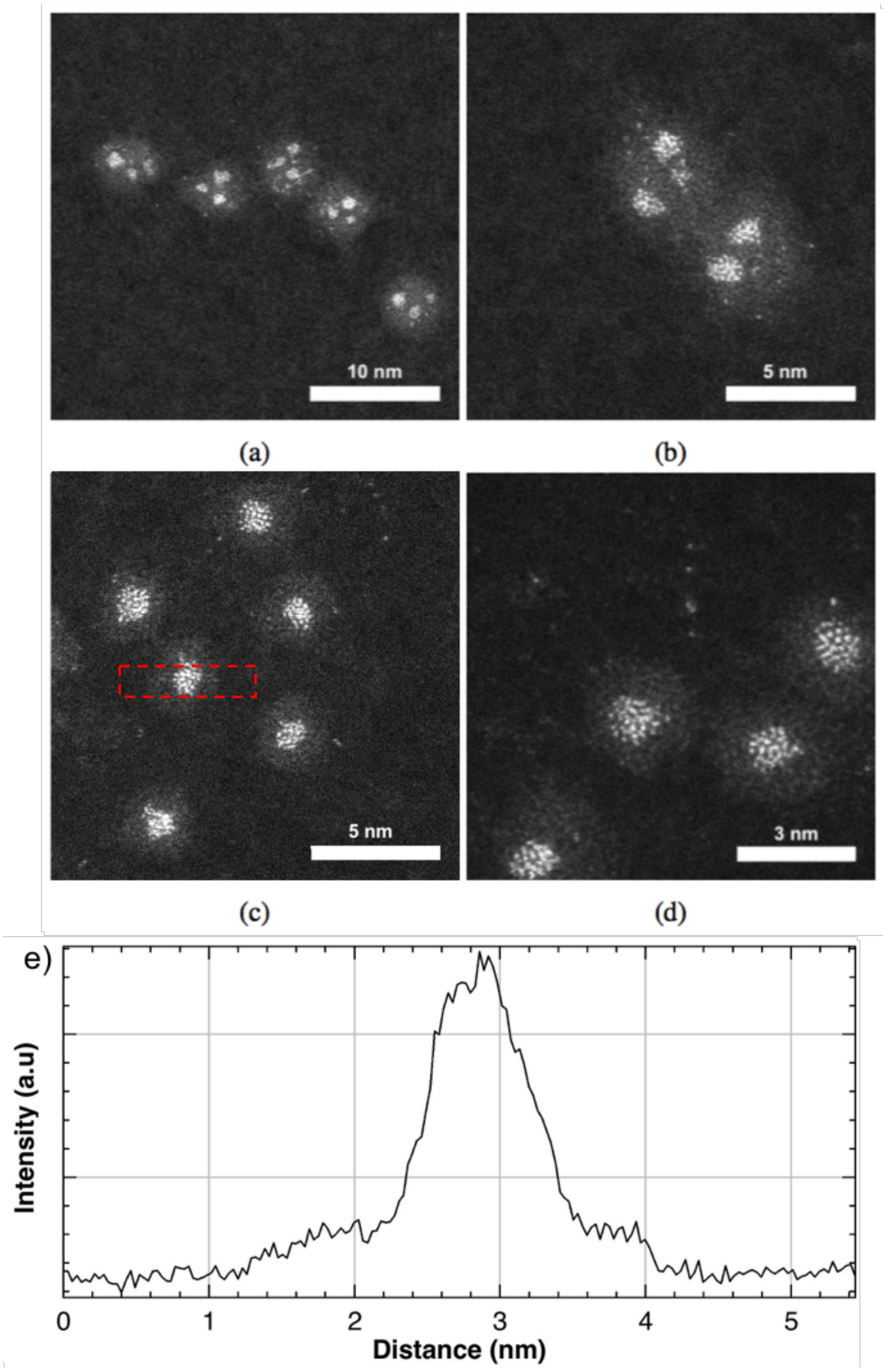

Figure 4.1: (a),(b) are STEM HAADF images of 90 kDa Pt-TiO_2 with different magnification. (c),(d) 30 kDa Pt-TiO_2. Pt is demonstrated by bright spots at core of the nanoparticle and the halo around and inside each nanoparticle is TiO_2. The higher magnification image demonstrates the interior. The single and multi core structure in each size is clearly visible. (e) is an average line profile of the red rectangle demonstrated on (e), the shoulders are TiO_2 HAADF intensity on carbon and the peak is TiO_2, Pt and carbon HAADF intensity. [image and caption taken from [109]]

in multi-core morphology, therefore total nanoparticle size is given. The core sizes in single and multi-core morphology are comparable which suggest the mechanism behind the core formation is identical. Hence, the multi-core morphology is mostly due the size difference between the two nanoparticles. The nanoparticle in both samples were fully oxidised due to Ti being one of the most reactive elements to oxygen and also long air exposure.

4.4 Morphology of Surface Oxidised Pt-Ti

In order to investigate the morphology of, as deposited nanoparticles and analyse the oxygen effect, it was crucial to image the nanoparticles morphology prior to oxidation. Therefore a portable glove box was modified so that it was attachable to the magnetron cluster source sample loading chamber, through the load-lock. The glove box was filled with Ar gas and the oxygen level was measured throughout the process. The oxygen level was below the detection limit of the device. The samples were then transferred inside the box to the STEM room and loaded in the STEM column. Due to the design of the electron microscope's load-lock a 2-3 second exposure of the sample to the air was inevitable.

The HAADF STEM images of the Ar transferred 90 kDa Pt-Ti nanoparticles is presented in figure 4.3. As it can be seen, the morphology is significantly different to the morphology of the oxidised Pt-Ti through prolong exposure to the air. It is clear that the initial state prior to full oxidation is a mixture of Pt and Ti i.e. alloy. However, as mentioned earlier the nanoparticles experienced a brief exposure to air during transfer. This resulted into a thin Ti oxide layer which can be observed as a thin halo around every nanoparticle, demonstrated more clearly in higher magnification images figure 4.3(b) and (c). From this point onward, the samples imaged in this process i.e. Ar transferred, will be referred to as surface oxidised Pt-Ti in contrast to the fully oxidised Pt-TiO_2 nanoparticles. The dispersion of

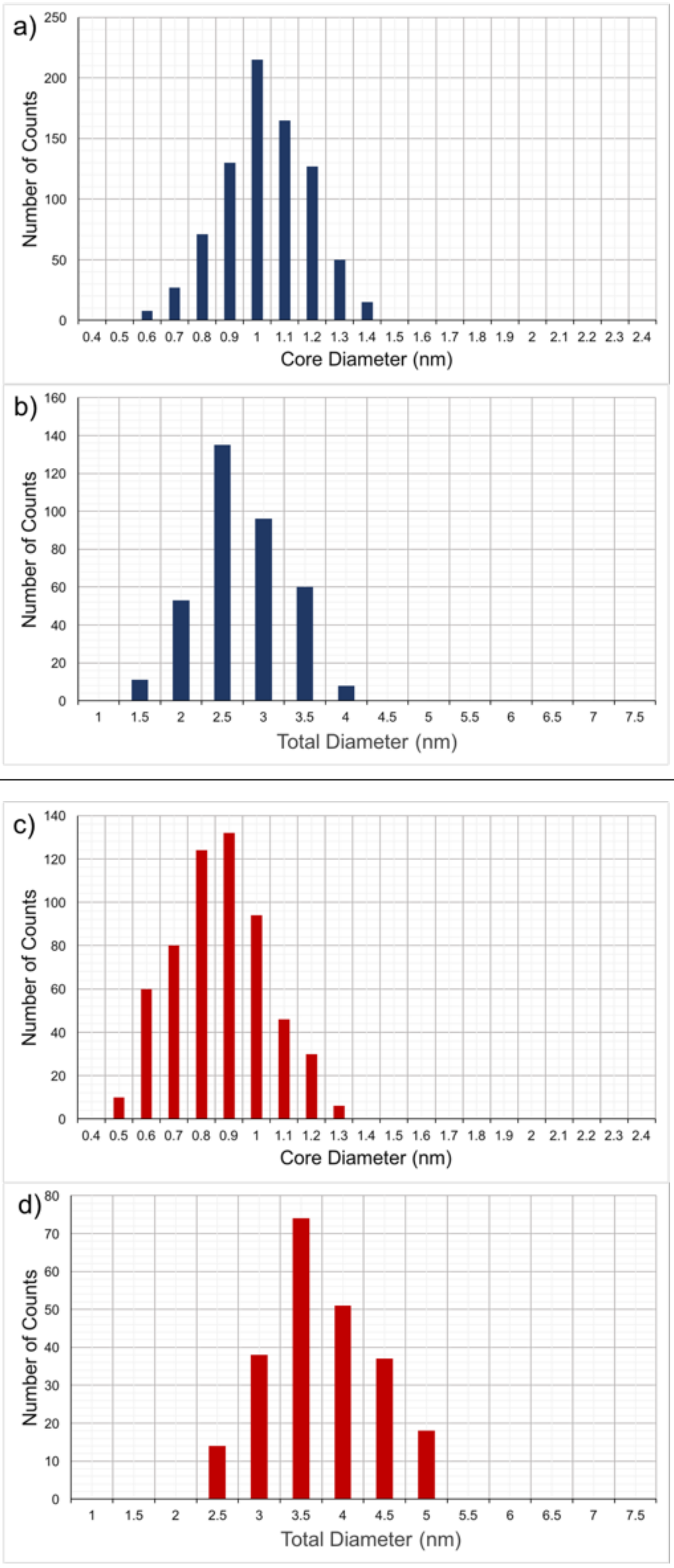

FIGURE 4.2: Size distribution for Pt core and total diameter of nanoparticle Pt-TiO_2. (a) and (b) presents 30 kDa core and total diameter respectively. (b) and (c) represent 90 kDa core and total diameter respectively. [(a) taken from [109]]

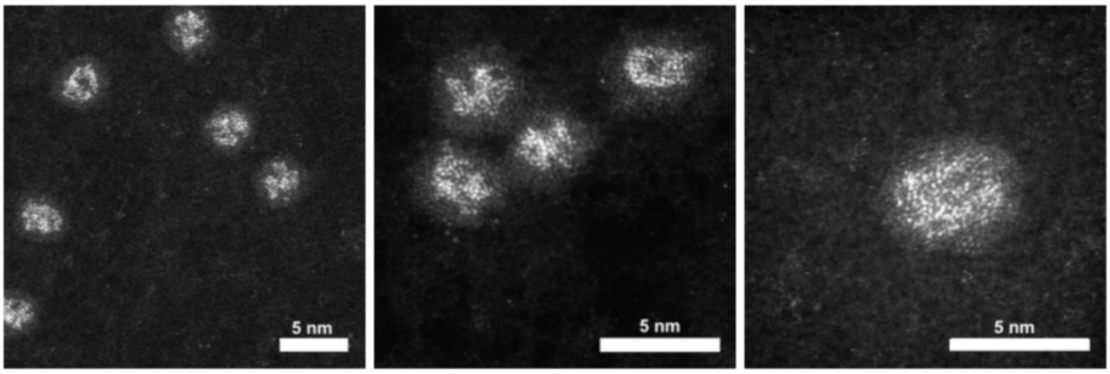

(a) (b) (c)

FIGURE 4.3: 90 kDa Pt-Ti nanoparticle prior to air exposure. The nanoparticles demonstrates an alloy morphology. The higher magnification image (c) shows the amorphous structure with greater details. Image form [109]

Pt atoms within the nanoparticle is also clearly visible in higher magnification images.

The difference in morphology of the surface oxidised Pt-Ti nanoparticles and the fully oxidised samples, suggests that the formation of core-shell structure is driven by the oxidation process. There are two possible routes for this process at the atomic level. Either the oxygen penetrates through the nanoparticles to oxidise the Ti or the Ti atoms migrate towards the surface of the nanoparticle to be oxidised. Generally the consequence of the second process is formation of Kirkendall effect (void formation). However, due to the small size of the nanoparticles and poor contrast of Ti in HAADF imaging, it is difficult to confirm or exclude void formation. In any case, the experimental observation confirm that the core-shell formation is primarily driven by oxidation. In the case of 30 kDa nanoparticles the particles are small enough for the Pt atoms to diffuse and form a single core. In larger 90 kDa particles the diffusion length of Pt atoms inside the TiO_x matrix is insufficient to from a single Pt core, in this case the multi-core structure i.e. several local Pt cores is formed within the nanoparticle. Further investigation on the morphology of surface oxidised Pt-Ti nanoparticles concluded that there is no particular structure within the alloy nanoparticle. This is clearly demonstrated in the high magnification image in figure 4.3(c).

4.5 Theoretical Results

Many different morphologies are observed in small metallic nanoparticles, these can range from octahedral (Oh), truncated-octahedral (t-Oh), decahedral (Dh), Ino-decahedral (I-Dh), Marksdecahedral (M-Dh), and icosahedral (Ih) [110, 111]. However, in the small nanoparticles i.e. number of atoms around 100, the strained Ih is the most stable structure, due to the low surface energies. Hence, for this study Ih Pt-Ti nanoparticles are investigated under the influence of oxygen exposure. Ih structure demonstrates twenty facets in closed packed (111) orientation that has twelve vertices on the surface. The Ih magic number 147 was chosen for this study as it offered balanced nanoparticle size and computational feasibility. The total number of atoms was divided to 13 Pt and 134 Ti to approximately match the experimental 1:13 ratio of Pt to Ti. The chosen number of Pt atoms matches the magic number Ih morphology which means it can form a stable single core in the computational analysis. The stability of 5 different configurations was investigated. (I) A random arrangement of Pt and Ti atoms in the nanoparticle (random), (II) one Pt atom positioned at the centre of the nanoparticle with other 12 sitting on the vertex sites (vertex), (III) a single core morphology with Pt atoms all residing at centre (single-core), (IV) double core morphology i.e. Pt atoms forming two separate cores (double-core), (V) Three core morphology i.e. Pt atoms forming three separate cores (triple-core). Each aforementioned morphology was covered with four different coverage and the total energy was calculated to assess the stability. The coverages were as follow 0 ML, 0.5 ML, 1 ML and 2 ML. 0 ML represents the unoxidised nanoparticles.

Figure 4.4 represents the most stable configuration for different coverages. Figure 4.4(a) presents the most stable structure without any oxygen exposure, the random arrangement was only slightly less stable. As the oxygen coverage increases the stability of the vertex arrangement becomes dominant, as shown in Figure 4.4(b). Further increase of the oxygen coverage to 1 ML results to a triple core

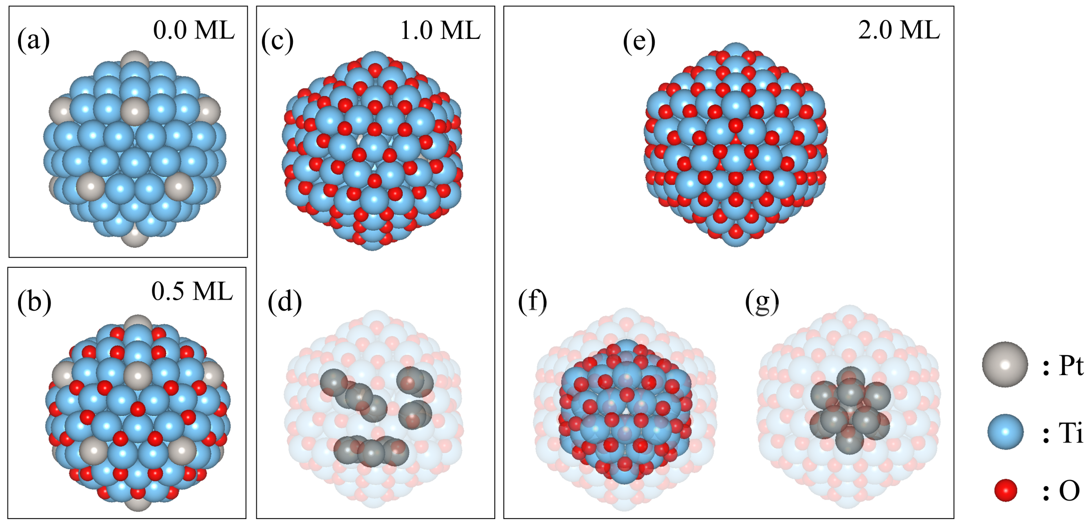

FIGURE 4.4: The most stable (Pt-Ti)$_{147}$ nanoparticle morphology obtained from DFT calculations.The Most stable structure with (a) zero oxygen exposure, (b) 0.5 ML of oxygen, (c) 1 ML of oxygen, (d) the three Pt cores in the centre, (e) 2.0 ML of oxygen with (f) (g) demonstrating oxygen configuration in sub-surface layer and the central Pt core. Blue spheres are Ti, silver represents Pt and red is oxygen. Figure and caption from [109].

morphology being the most stable structure, shown in 4.4(c) and finally fully oxidised nanoparticles i.e. 2 ML oxygen coverage demonstrates a single core as the most stable structure as shown in 4.4(e).

TABLE 4.1: Diameters and bond lengths for the (Pt-Ti)$_{147}$ nanoparticles with the most energetically stable arrangement for different oxygen coverages.Table from [109]

Oxygen coverage (ML)	Arrangement	Diameter of nanoparticle (Å)	Average bond length (Å)			
			Ti-Ti	Pt-Ti	Pt-Pt	Ti-O
0.0	vertex	15.58	2.85	2.73	-	-
0.5	vertex	15.66	2.95	2.95	-	1.95
1.0	triple-core	16.68	3.05	3.05	2.95	1.95
2.0	single-core	16.75	3.05	2.75	3.05	2.15

Table 4.1 presents the average bond length as well as the nanoparticle diameter for the most stable configuration in each case. The diameter is defined as the distance between two diagonal vertices passing through the centre of the nanoparticle. There is an increasing trend on almost every parameter suggesting that the oxygen adsorption induces an expansive strain in the nanoparticle. The only exception is in the Pt-Ti bond length where the Pt atoms form a single core at the centre, the

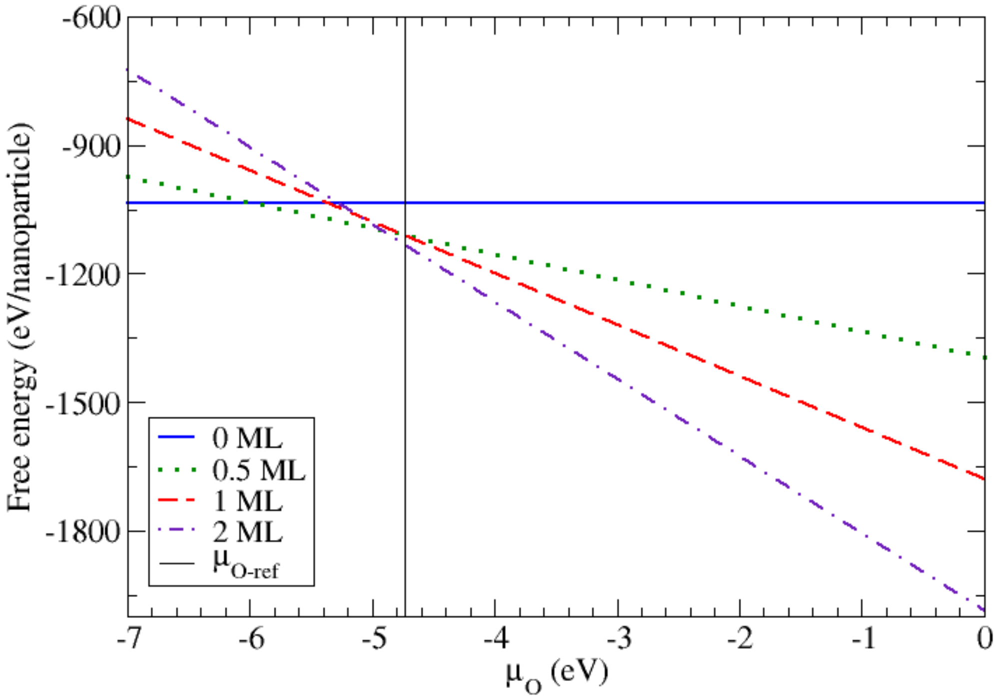

FIGURE 4.5: Free energy of the Pt-Ti nanoparticle as a function of oxygen chemical potential. The vertical line at $\mu_O = -6.0$ eV represents the point where the reduction of TiO_2 to hcp-Ti occurs. Figure and caption from [109]

decrease is expected as the arrangement is more compact due to the location of the cores.

In order to understand the influence of oxygen on the morphology in a continues manner. The free energy as a function of the oxygen chemical potential was calculated, presented in Figure 4.5. The free energies were computed using the total energy of the most stable morphology for four different coverages. The upper limit of oxygen chemical potential was defined as half the energy of the oxygen molecule i.e. $\mu_O = E_{O_2}/2 = 0$ eV. The most stable morphology is the vertex arrangement for $\mu_O = -6.0$ eV. The most stable structure is maintained as the same vertex arrangement between -6.0 eV $< \mu_O < -4.9$ eV with 0.5 ML coverage.

For oxygen chemical potential values higher than -4.9 eV the most stable structure is the single core morphology with 2 ML oxygen coverage. It is also clear that the 1 ML oxygen coverage is not thermodynamically stable at any oxygen potential in the calculation. The chemical potential at which rutile TiO_2 is reduced to metallic hcp-Ti is also demonstrated on Figure 4.5. This suggests that the surface and subsurface of the Ih nanoparticles are fully oxidised at oxygen chemical potentials lower than the bulk reduction limit, leading to the conclusion that the nanoparticle is more readily oxidised than the bulk TiO_2. The finding are in agreement with the experimental observations for 30 kDa Pt-Ti forming a Pt core with TiO_2 shell after oxygen exposure.

4.6 Discussion

It has been demonstrated that oxygen exposure through the ambient air or by other means has a crucial impact on the morphology of the Pt-Ti bimetallic nanoparticles. HAADF STEM observations showed that fully oxidised nanoparticles by prolong exposure to the air, results in formation of TiO_2 accompanied by Pt core formation. In the case of smaller 30 kDa nanoparticles a single core formation was observed whereas increasing the mass of the particles to 90 kDa, result in a multi-core morphology. In order to capture the morphology before any oxidation, 90 kDa nanoparticles were transferred under Ar gas, although there were still a brief exposure to air but this provided an insight into the morphology before any oxidation as close as possible with the available experimental setup. The results demonstrated a mixture morphology for Pt-Ti nanoparticle, i.e.Pt dispersed within Ti. In the case of smaller 30 kDa nanoparticles, the diffusion length of the Pt atoms within Ti is sufficient for the Pt atoms to coalesce as a single Pt core. On the other hand, increasing the size of the nanoparticle to 90 kDa results in insufficient diffusion length of Pt atoms within nanoparticle to form a large single core, rather several local cores are observed.

The most stable theoretical structural was deduced by considering 10 different arrangements covered by 4 different oxygen coverages. The lower symmetry random and multiple core morphologies may have other possible arrangements, but it is not feasible to examine all possibilities by DFT due to the high computational power required. It is also important to note that real adsorption of oxygen may reduce the symmetry, whereas in the calculation it was assumed that oxygen atoms adsorb homogeneously and symmetrical on all facets of the nanoparticle. Nevertheless, the subset of configuration studied is sufficient to demonstrate the structural trends on oxidation.

The general trends observed experimentally and theoretically are in close agreement. Both trends are towards core formation as the level of oxidation increases. For instance, experimentally, it was observed that oxidation is mainly responsible for nucleation of Pt atoms to form single cores, similar trend is also observable in theoretical calculation. The agreement is particular strong in the smaller size 30 kDa nanoparticles, where the single core morphology is observed.

This is expected due to the size of the simulated nanoparticles being much closer to 30 kDa nanoparticles. However, there are also differences, for instance, one might say that the most stable structure with 0.5 ML or zero coverage of oxygen was theoretically shown to be the vertex configuration i.e. majority of Pt atoms residing on the surface, this morphology was not seen in the experimental analysis. The important point to note when making this correlation is that experimental results did not show an oxygen free nanoparticle or even 0.5 ML oxidised nanoparticle, due to the brief exposure of the samples to the air during electron microscope sample loading. Thus, all the samples analysed, most likely had at least the first full layer of Ti, oxidised. Therefore, a better approach would be to correlate theoretical results for oxygen coverages greater than or equal to 1.0 ML with the experimental results. In this case, the morphology of Ar transferred Pt-Ti nanoparticles fits very closely to the theoretically calculated structure. In addition, the experimental observation of the multi-core structure could be mainly due to the increased flexibility in the size and shape and the ability of the nanoparticle to accommodate strain fields associated with the multi-core structure, as well as the inability of Pt atoms to diffuse fast enough to form a single core at room temperature.

Chapter 5

Post Processing of Pt-Ti Nanoparticles Through Thermal Annealing

5.1 Introduction

In this chapter, the focus is on thermal effects on the morphology of Pt-Ti nanoparticles. The aim was to show that it is possible to modify and control the morphology of bimetallic nanoparticles after production stage i.e. post processing. In the first section, the surface oxidised nanoparticles were modified through electron beam heating. To further investigate the thermal effect and the electron beam interaction, DENS Wildfire heating stage was used to perform the heating under the electron beam.

The first section of this chapter is from a published paper by the author.

Many chemical reactions require high temperature to take place or elevate the sample temperature due to exothermic properties of the reaction. In other cases other than chemical reactions, high temperature treatments may be utilised to overcome potential barriers from a low state to a lower state. Therefore firstly it is important to investigate the rule of temperature on the morphology of nanoparticle. Secondly, the thermal treatment of nanoparticle may be utilised to post process nanoparticles. In this chapter we attempt to address both possible affect of temperature on Pt-Ti nanoparticles.

5.2 Method

Samples were made in the magnetron cluster source through sputtering of the Pt-Ti target. The nanoparticles were size selected through time-of-flight based mass filter. The nanoparticles were then deposited on TEM grids or DENS heating nanoChips for the experiments. Soft landing regime was used to deposit the nanoparticles, this corresponds to landing energies of 1 to 2 eV per atom. The inert gas glove box was used to transfer the samples from the cluster source room to the STEM to minimise oxygen exposure through air. HAADF ac-STEM imaging was employed to collect data. The electron beam current was 30 pA. Temperature measurements were done through the software provided by DENS for the DENS wildfire holder.

5.3 Beam Induced Pt-Ti Morphology

In order to examine the electron beam - nanoparticle interactions, initially 90 kDa Pt-TiO_2 nanoparticles on TEM grids were loaded in the microscope. Numerous experiments were performed to examine the effect on the morphology of the nanoparticles. For instance, exposing a single nanoparticle to high dose of electron radiation by focusing the electron beam on the nanoparticle for a short period, or long scanning of a nanoparticle to achieve small dose but persistent exposure

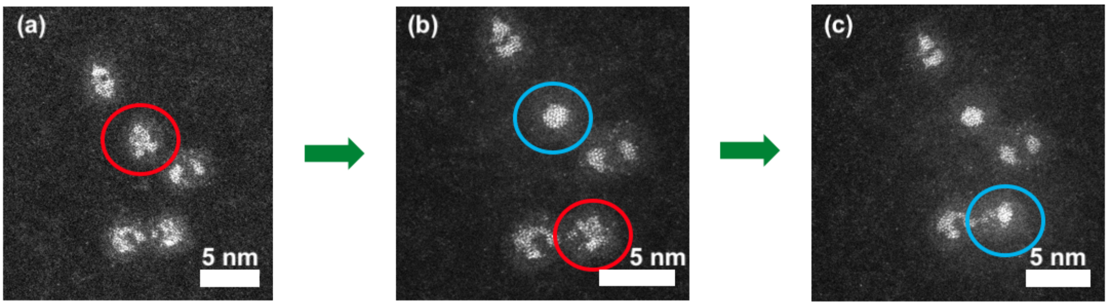

FIGURE 5.1: Sequential modification of two individual surface oxidised Pt-Ti 90 kDa nanoparticles using a focused electron beam. Initial state is an amorphous alloy Pt-Ti, however the interactions with the electron beam at 30 pA current creates a single Pt core. The time direction is from left to right. Red circle indicate the nanoparticle before modification and blue circles indicate the same nanoparticle after modification. Figure and caption from [109]

to the electron radiation. However the nanoparticles were unresponsive to any electron beam effect.

On the other hand, when Pt-Ti nanoparticles were transferred under the Ar gas to the electron microscope to achieve only surface oxidised morphology , the outcome was different. A high dose of electron radiation was provided to a single nanoparticle with an alloy structure through focusing the electron beam on the nanoparticle. This induced aggregation of the Pt atoms within the nanoparticle to form a single core. The procedure and the experiments results are presented in Figure 5.1.

This radiation was achieved by zooming the electron beam to a magnification of x50M. Figure 5.1(a) shows the start of the experiment, the nanoparticles are in an alloy morphology. The red circle indicates the selected nanoparticle in its pre-exposure state. After applying the electron dose radiation for 5 seconds, image presented in Figure 5.1(b) was taken. The blue circle indicates the same nanoparticle after the exposure. It is clear that the exposed nanoparticle has transformed to a single core morphology from the original alloy structure. The procedure was repeated on the second nanoparticle indicated by the red circle in figure 5.1(b) and the outcome is represented in figure 5.1(c), similar outcome was observed. The procedure was repeated on many different nanoparticles of different samples and the outcome was reproducible.

The electron beam - nanoparticle interaction mechanism is generally believed to be through electron beam induced heating effect, defect formation in the particles, charging of the particle and excitation of surrounding gases. To examine which mechanism is primarily causing the single core formation, the electron beam was focused adjacent to the particle, the electron beam had no affect on the nanoparticle. This eliminated the possibility of excitation of surrounding gases. Then the electron beam was focused on an off-centred location on the nanoparticle, the single core formation was observed however the location of the core did not depend on the position of the electron beam, which also eliminates defect formation.

It should also be noted that the absence of single core formation when Ti is fully oxidised in multi-core structure, suggests that the electron beam reduction is inactive, it is reasonable to assume that the effect of charging is also negligible. Hence, the only remaining interaction is the electron beam induced heating.

The contradicting final morphology in the presence of electron beam versus exposure to oxygen i.e. single against multi-core configuration, suggests that the extra thermal energy provided by the electron beam is sufficient to increase the diffusion length of Pt within the nanoparticle to form a single core which is, as discussed in section 4.5, the most energetically favourable configuration. In contrast, in the absence of this thermal energy, several local Pt cores are formed rather than a single core.

5.4 Thermal Annealing

An electron bombardment heating stage was developed to anneal samples *in situ* after deposition. The annealing temperature was measured by a pyrometer focused

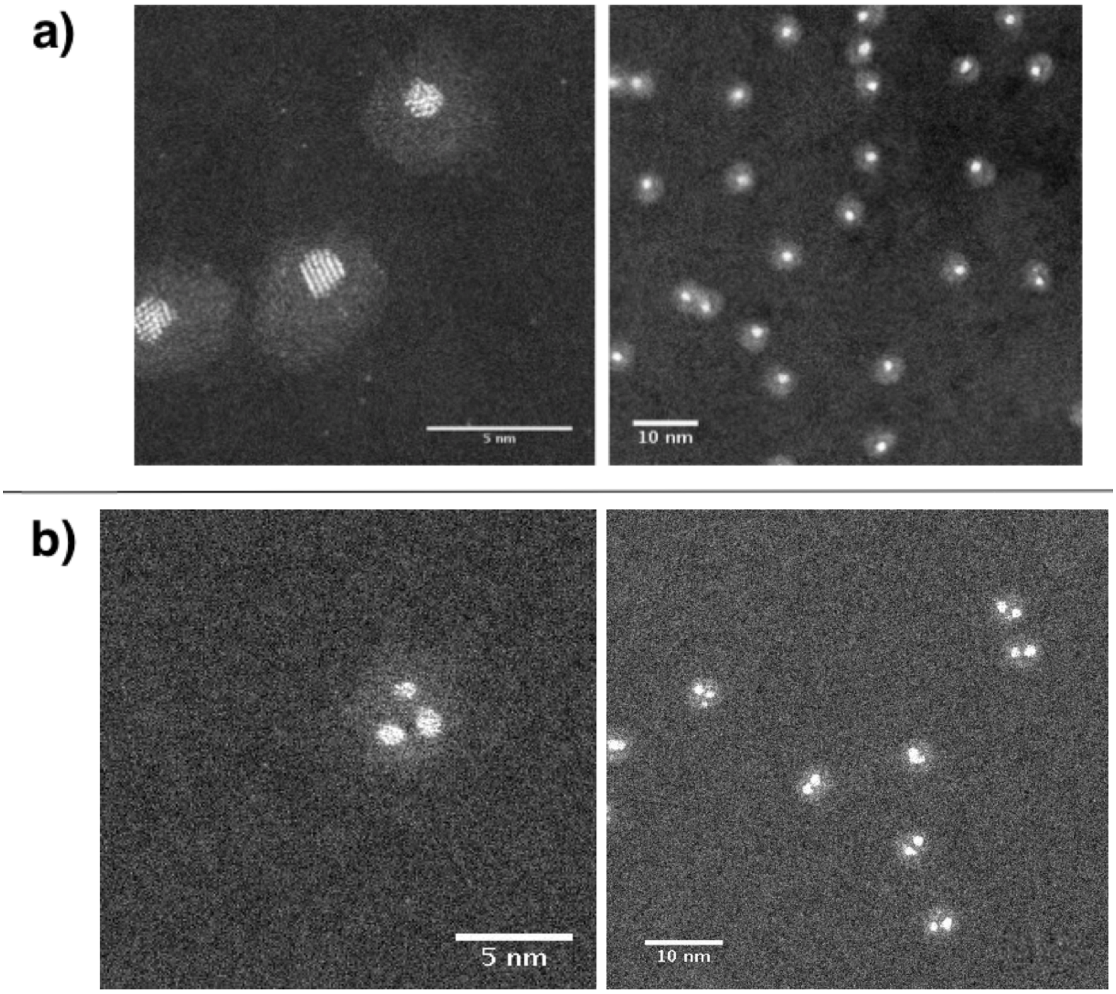

Figure 5.2: HAADF-STEM image of 90 kDa Pt-Ti nanoparticle. a) single Pt core with Ti shell induced by annealing the sample using laser, b) multiple core formed by exposing sample to the oxygen without annealing.

on the sample. 90 kDa nanoparticles were deposited on two TEM grids, positioned next to each other. However, only one was annealed by the annealing stage, the annealing temperature was measured to be around 600 ± 100 ^{o}C. Then both samples were transferred under Ar gas for STEM imaging. The annealed sample was loaded first into the microscope, while the other sample was allowed to oxidise through exposure to the ambient air and was imaged the next day. Figure 5.2 presents the data obtained.

Figure 5.2(a) presents two STEM images of the annealed sample, it is clear that the single core morphology is formed by the 90 kDa nanoparticles. However, the sample that had not been annealed prior to oxidation demonstrated multi-core morphology. In order to investigate the stability of the single core formation, the sample was stored under the ambient air and re-imaged in the electron microscope within two weeks. It was observed that the single core morphology was retained after full oxidation of the Ti shell.

Previously the Pt core size was measured to be 1.0 ± 0.2 nm in diameter for single core 30 kDa Pt-Ti nanoparticles and the core size was measured to be 0.8 ± 0.4 nm in diameter for Pt cores in 90 kDa multi-core morphology. Figure 5.3 presents statistical analysis on the core and total particle diameter for 90 kDa single core induced through annealing. It was deduced that the particles form a core size of 1.7 ± 0.4 nm. The increase of the core size in respect to the 90 kDa multi core morphology and single core 30 kDa morphology, confirms that it is the total coalescence of Pt atoms within the nanoparticles that creates the larger Pt core. In contrast, the total size of the nanoparticle stays constant.

Further investigation was carried out by increasing the annealing temperature. The temperature was increased to 900 ± 100 ^{o}C without changing the annealing time or the sample production parameters.

Figure 5.4 presents the HAADF STEM images of the data acquired. Increasing the annealing temperature induced the segregated Pt-Ti morphology, where the Pt core is adjacent to a larger Ti nanoparticle. The stability of both single core and segregated morphology was examined by exposing the samples to oxygen through air and re-imaged under the electron microscope. It was observed that the samples retain the morphology after oxygen exposure.

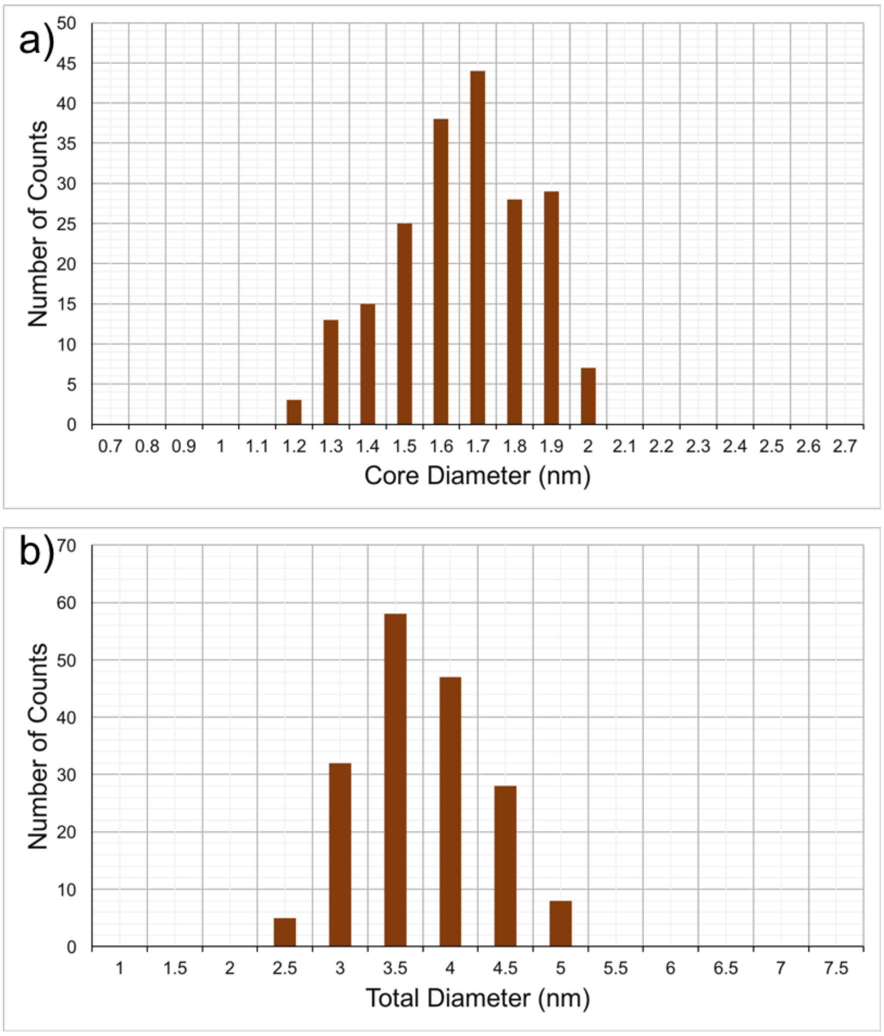

FIGURE 5.3: Histogram of the core (a) diamater and total particle diameter (b) for 90 kDa single core induced through annealing.

5.5 Annealing Under the Electron Beam

In order to further develop the understanding on thermally induced morphology of the Pt-Ti, the DENS Wildfire heating stage was employed to perform live annealing under the electron beam. 90 kDa nanoparticles were deposited on the DENS heating chips with 5% surface coverage. The samples were transferred under Ar gas inside a glove box to the STEM room and loaded into the STEM with minimal oxygen exposure.

Figure 5.5 demonstrates the experimental procedure. Following the green arrow

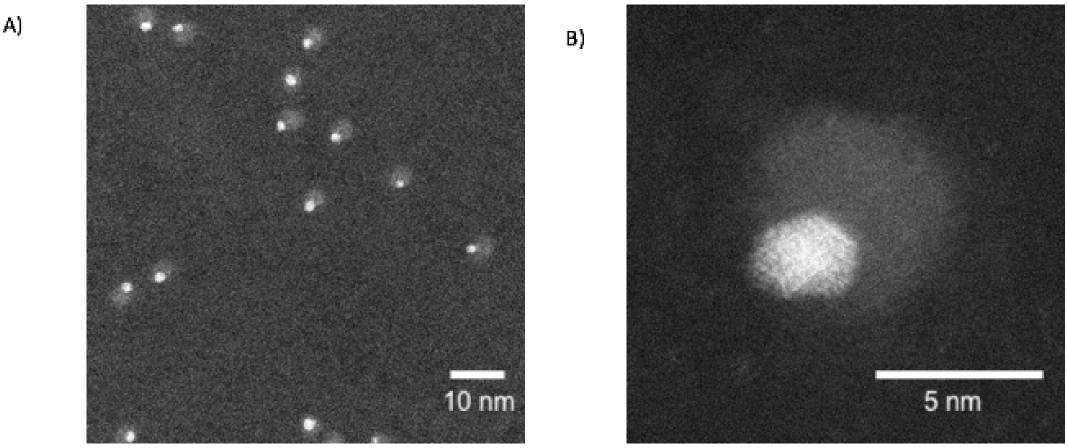

Figure 5.4: HAADF-STEM image of 90 kDa Pt-Ti nanoparticle annealed in situ to a higher temperature. A) presents a low mag and b) is a higher mag image.

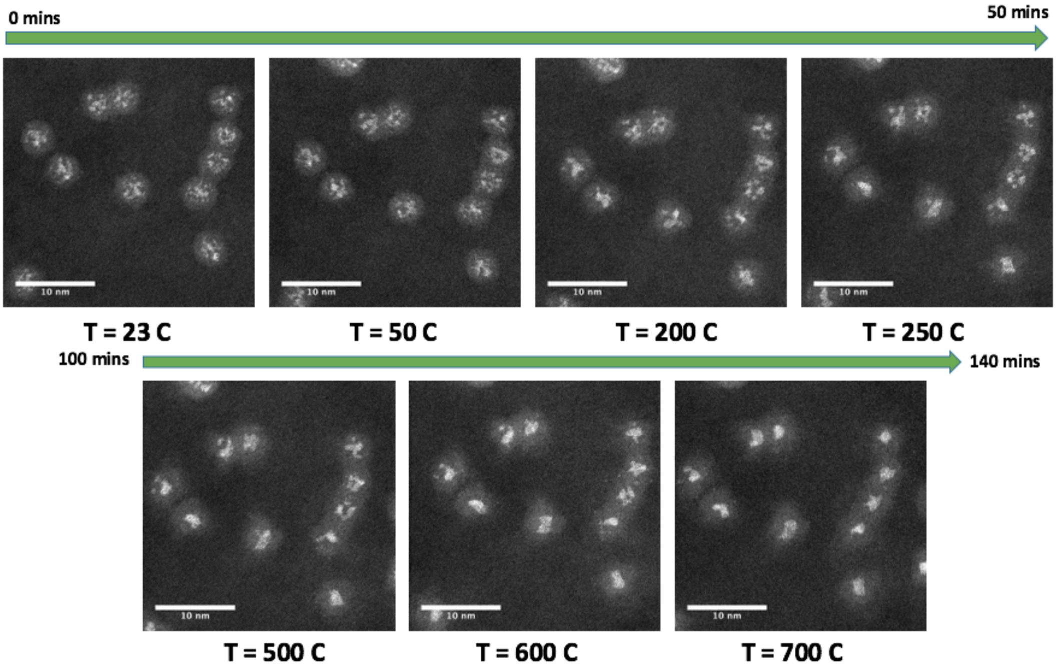

Figure 5.5: HAADF-STEM of thermally annealed Pt-Ti nanoparticles under the electron beam. The green arrow demonstrates the direction of time and the recorded temperature is demonstrated at the bottom of each image. It can be seen that as the temperature increases the morphology of the nanoparticle changes from an alloy to single Pt core.

which indicates the direction of time, the nanoparticles start in an alloy structure. The temperature was then increased in 50 ^{o}C increments. There was a 10 minutes settling period after each temperature increment.It can be seen that the morphology of the nanoparticle varied from a dispersed Pt within Ti to a single Pt core. It seems that the thermal energy supplied was enough to enhance diffusion of Pt atoms within the nanoparticle to form a single core morphology.

To establish that the morphology change was solely due to the thermal annealing process and not a combination of the electron beam induced effect (thermal and charging) and thermal energy supplied by the DENS holder. The following steps were taken. The annealing was stopped to prevent further changes after single core observation and the sample temperature was brought back to room temperature i.e. 23 ^{o}C. Then the location of the imaging was changed to observe whether nanoparticles on the substrate which had not been exposed to the electron beam prior to this stage, showed the same morphology change. It was observed that the morphology change was uniform across the sample, regardless of electron beam presence.

Figure 5.6 demonstrates the three stages of the experiment. Figure 5.6(a) presents the surface oxidised Pt-Ti nanoparticles at room temperature before any thermal processing. Figure 5.6(b) presents the same sample, heated to 700 ^{o}C under the electron beam. Single core morphology across the sample is clearly visible. Therefore, this rules out the possibility of the nanoparticles charging through the electron beam for single core formation. Finally the annealing temperature was increased to 900 ^{o}C, figure 5.6(c) shows images after increasing the temperature. It is clear that at higher temperatures the segregated core-shell morphology was formed, as expected. It should be noted that thermally annealing the samples to high temperatures affected the ability of obtaining atomic resolution in the STEM. This could be mainly due to the shake up of the nanoparticle and the sample substrate due to high thermal energies.

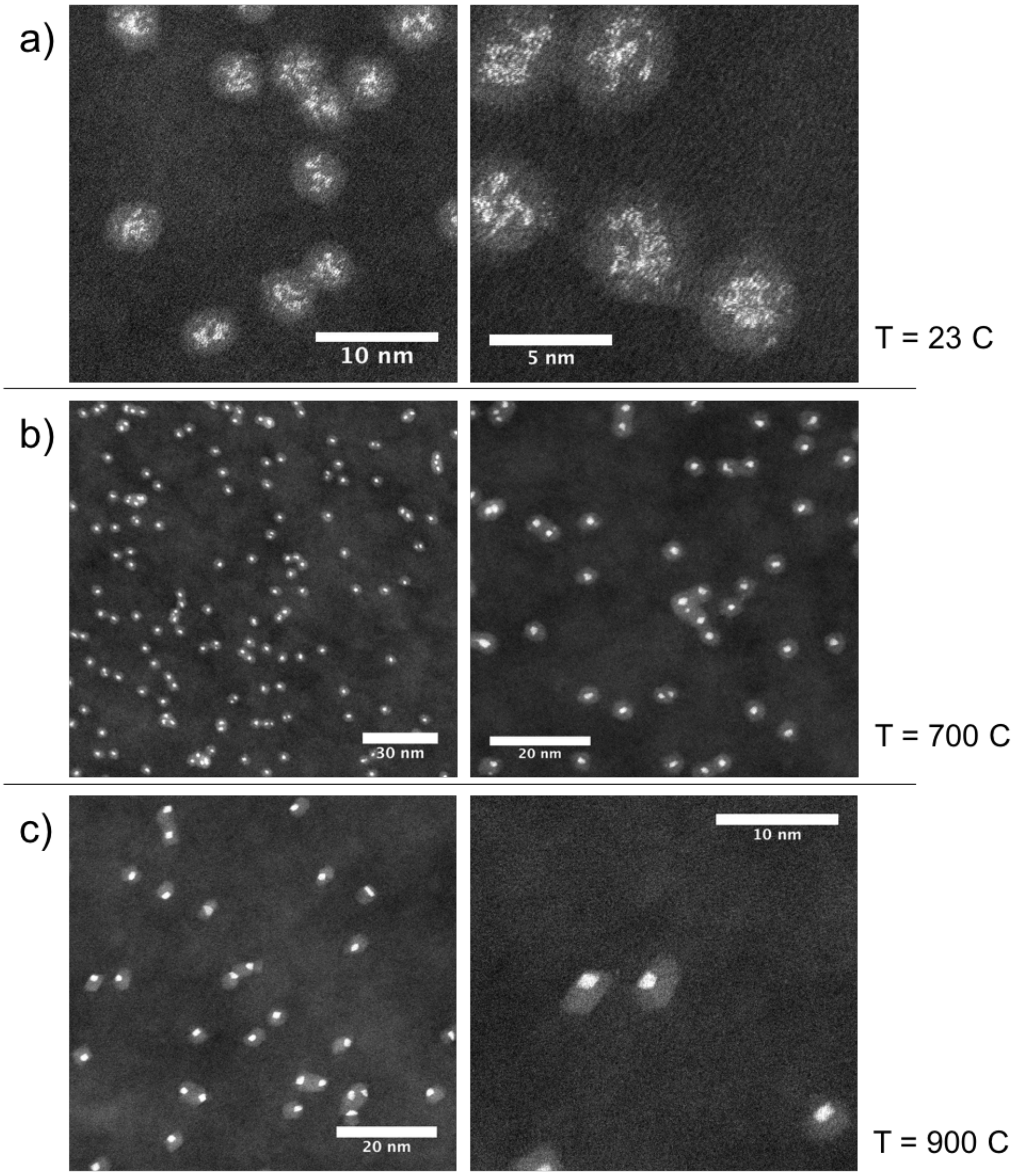

Figure 5.6: HAADF STEM images of surface oxidised 90 kDa Pt-Ti at different temperatures. (a) demonstrates the morphology at room temperature, It is clear that Pt atoms are dispersed within the nanoparticle.(b) presents nanoparticles at 700 C, it can be seen that a single core morphology is formed, (c) presents images at 900 C where a segregated Pt-Ti is formed.

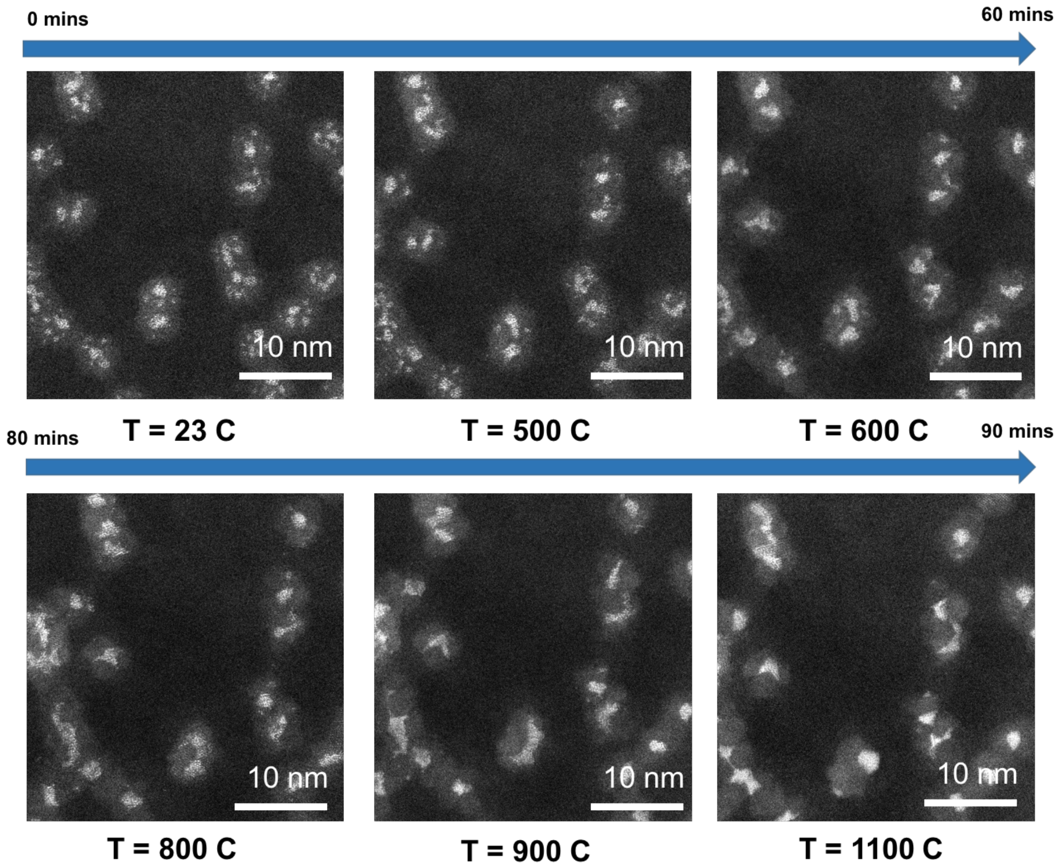

FIGURE 5.7: HAADF-STEM of thermally annealed Pt-Ti nanoparticles under the electron beam. The blue arrow demonstrates the direction of time and the recorded temperature is demonstrated at the bottom of each image. It can be seen that as the temperature increases the morphology of the nanoparticle changes from multi-core to single segregated core-shell.

The same process was repeated for fully oxidised Pt-TiO_2 nanoparticles. 90 kDa Pt-Ti nanoparticles were deposited on DENS heating chips. Then the sample was exposed to oxygen through the air for more than 24 hours to ensure full oxidation. The sample was loaded into the microscope.

Figure 5.7 presents the process as well as the nanoparticles morphology at different temperatures. The temperature was increased in 50 °C increments and every temperature increment was followed by 10 minutes of stabilisation period. The multi-core morphology of the nanoparticles is clearly visible at the beginning of the process. As the sample temperature was elevated, the aggregation of the Pt atoms within the nanoparticles is visible. However, unlike the surface oxidised

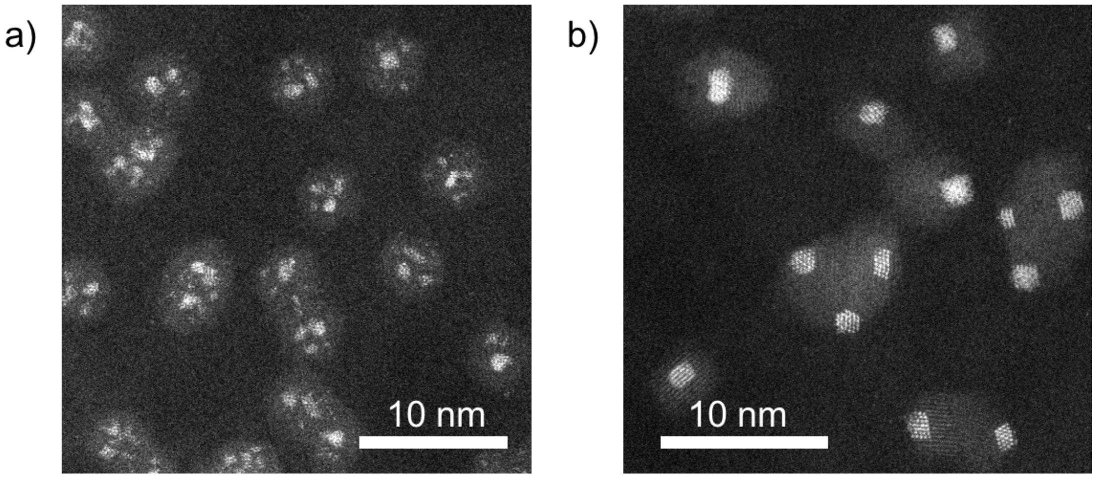

FIGURE 5.8: HAADF STEM image of 90 kDa Pt-TiO_2 nanoparticles. (a) demonstrated as oxidised morphology of the nanoparticle at room temperature. a multi core structure. (b) the same sample after annealing to 1100 C under the electron microscope, a segregated Pt-TiO_2 nanoparticle.

nanoparticles presented in figure 5.5, the process lacked the uniform single core formation stage. As mentioned earlier, aggregation of Pt atoms was observed. But the process was rather disordered for formation of single core. When the sample temperature increased even further to around 900 ^oC, the movements of the Pt aggregate to the sides of the nanoparticle was observed similar to the surface oxidised Pt-Ti. Finally ramping up the temperature to 1100 ^oC which was the maximum temperature achievable by the DENS heating setup, an entirely segregated core-shell morphology was observed with Pt positioning itself adjacent to the TiO_2.

Figure 5.8 presents a before and after image of the sample. Figure 5.8(a) demonstrates the morphology of fully oxidised Pt-TiO_2 at room temperature, the particles show a multi core structure as expected. In figure 5.8(b) the particles were annealed to the maximum temperature of 1100 ^oC, the thermal energy provided induced a Pt-TiO_2 segregated morphology.

In order to determine if the Pt core in segregated morphology is exposed or buried under a Ti shell, two nanoparticles with similar size were chosen having similar Pt core size. Both nanoparticles are presented in figure 5.9. Figure 5.9(a) is the single core and figure 5.9(b) is the segregated structure. Further, the average line profile of a rectangle shape area on the core was obtained. The blue and red rectangles indicate the area. The results were then normalised for comparison. Figure 5.9(c) shows the results from the line profiles. The plot shows similar intensity for both Pt cores. In single core morphology the Pt core was covered by a Ti shell. The Pt core intensity in segregated morphology demonstrates similar overall intensity, this suggests that even in the segregated morphology the Pt core was not completely exposed and still covered by Ti.

It was noticed that heating the nanoparticles produced an ordered structure of Pt and Ti shell as it can be seen in figure 5.10(a). The HAADF STEM image presents two 90 kDa Pt-TiO_2 nanoparticles annealed to 1100 ^oC.

In figure 5.10(a), the right hand-side nanoparticle is on-axis with the electron beam and it can be clearly identified as the (111) plane of the FCC structure. On the other hand, the left hand-side shows a particle that was slightly off axis to the electron beam, hence the structure was blurred. Both particles were exposed to air after annealing. In both cases an average line profile was obtained. The coloured rectangles indicate the area. Figure 5.10(b)-(c) presents the results of each line profile. The colour of the plot corresponds to the colour of the rectangle. The plots were then used to determine the atomic spacing for the Pt and TiO_2 atomic rows. Similar procedure was repeated for Pt-TiO_2 annealed to 1100 ^oC without any further air exposure as well as single core Pt-Ti.

Table 5.1 presents the measured values for the atomic spacing in every case. It was deduced that the spacing is similar between all cases. However Pt atomic spacing is smaller than the bulk value of the atomic spacing in (111) plane, this value was obtained using $\frac{\sqrt{2}a}{2}$ where a is the lattice constant. This could be an induced effect due to a combination of the higher strain present in a nanoparticle, an effect imposed by presence of Ti or an affect due to the accuracy of the calibration in the STEM.

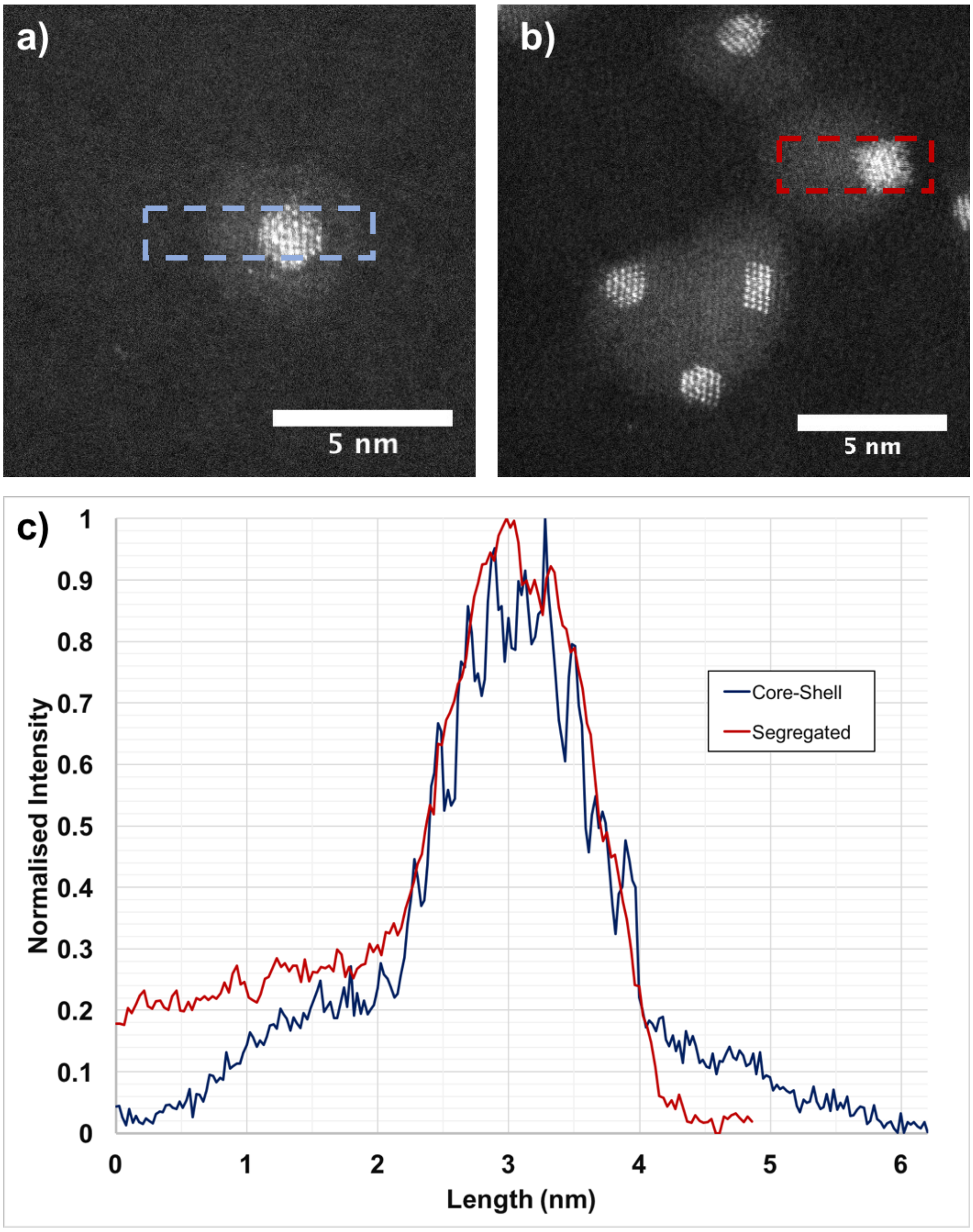

Figure 5.9: HAADF STEM image of 90 kDa Pt-TiO_2 nanoparticles with different morphology. (a) single core and (b) segregated. The blue and red rectangle indicate the area chosen for line profile. (c) average line profiles with matching colour to the rectangles. Total intensity over the core were comparable.

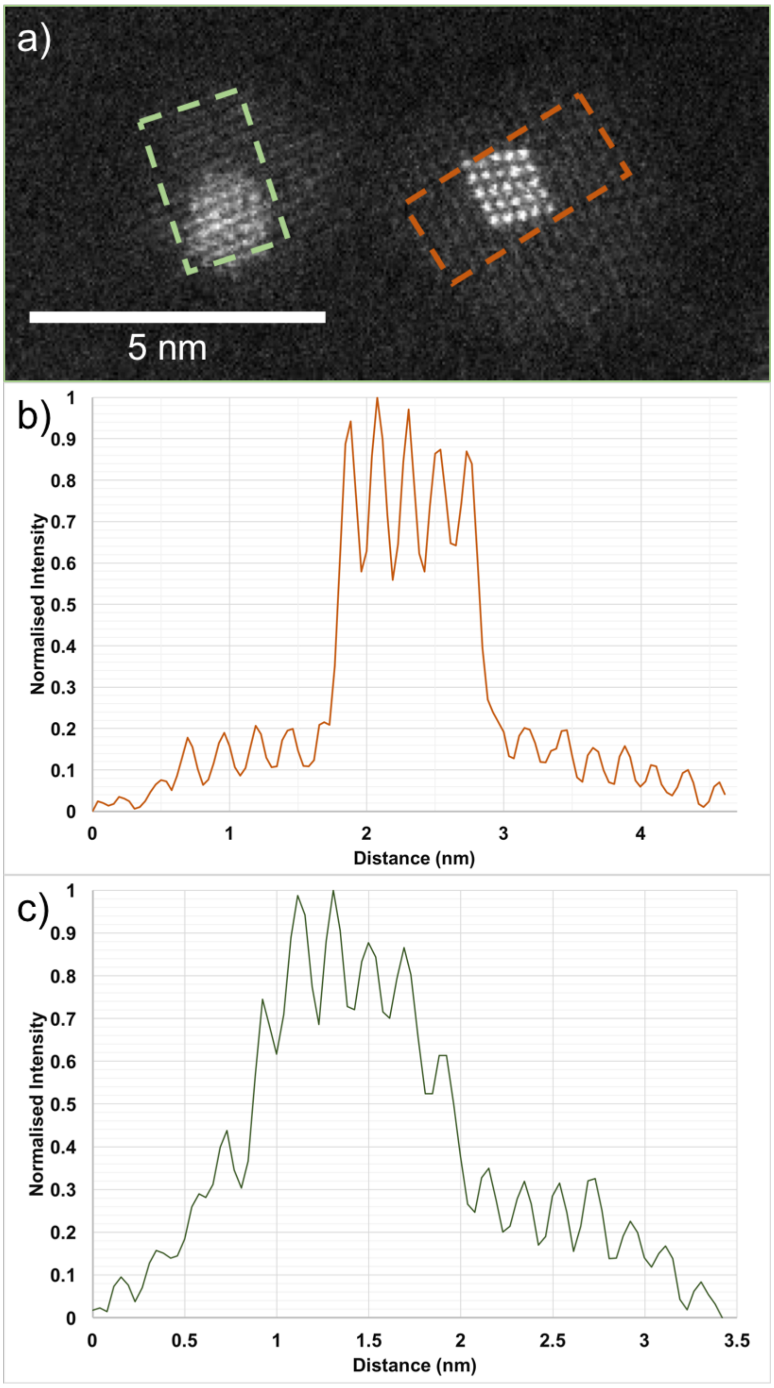

FIGURE 5.10: (a) HAADF STEM image of 90 kDa Pt-TiO_2 nanoparticles after annealing. The green and brown rectangle indicate the area chosen for line profile. (b)-(c) show the results for each line profile. The colour of the plot corresponds to the colour of the rectangle.

Table 5.1: Segregated (A) Argon transferred - annealed, Segregated (B) oxygen exposure - annealed - oxygen exposure. Segregated (C) oxygen exposure - annealed. Pt and Ti bulk atomic spacing values obtained from [112] and [113] respectively.

Type	Pt (nm)	Ti (nm)
Single Core	0.21 ± 0.02	-
Segregated (A)	0.23 ± 0.02	0.28 ± 0.03
Segregated (B)	0.22 ± 0.01	0.28 ± 0.01
Segregated (C)	0.21 ± 0.01	0.25 ± 0.02
Bulk	0.277	0.295

5.6 Discussion

It was demonstrated that the electron beam can be used to modify the structural configuration of Pt-Ti nanoparticle. The nanoparticle was manipulated by the electron beam to form a single Pt core morphology. An investigation was performed to determine what aspect of the electron beam was the main driving force of the observed behaviour. It was concluded that the additional thermal energy transferred to the nanoparticle by the electron beam is the main interaction.

This led to thermal annealing investigation of the nanoparticles. It was demonstrated that identical results can be achieved by thermal annealing of the nanoparticle *in situ* after deposition and prior to oxygen exposure. Statistical analysis on the core and total nanoparticle size showed that the total size of the nanoparticle is unaffected, however the size of single Pt core of 90 kDa Pt-Ti nanoparticles increases to 1.7 ± 0.4 nm. It was also observed that elevating the annealing temperature to 900 ± 100 ^{o}C, induced a segregated core shell morphology.

This phenomenon was investigated in real time using the DENS heating stage. The sample was heated gradually and the structural change was recorded under the electron beam. It was also established that the additional thermal energy is the main cause of the morphology change. Due to the nature of the experimental i.e. gradual change of the morphology it is difficult to determine a precise onset temperature. However, it can be estimated by reviewing the videos to be 700

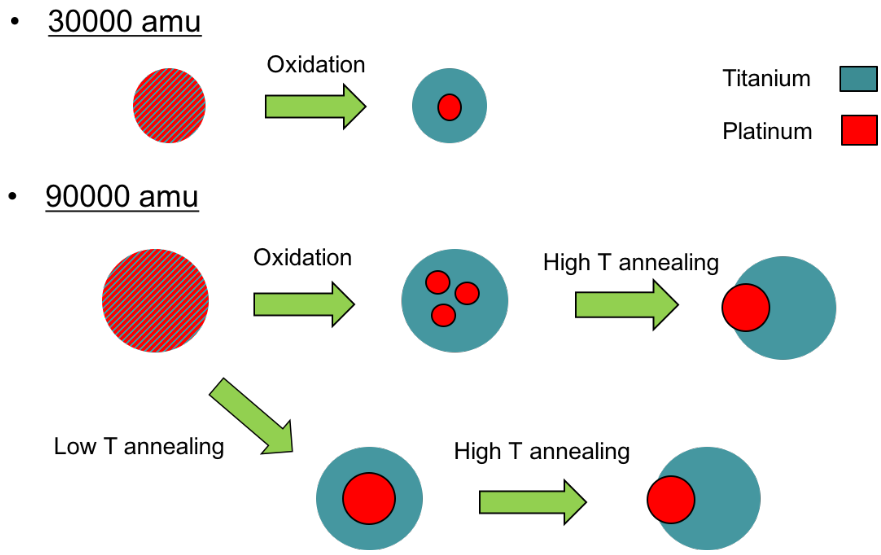

Figure 5.11: Schematic of modification process through either oxidation of Pt-Ti nanoparticle or thermal annealing.

± 100 °C for single core formation and 900 ± 100 °C for formation of segregate morphology. Similar experiment was performed after allowing the nanoparticles to fully oxidise prior to annealing in the STEM. Figure 5.11 presents a schematic of the processes observed in the experiment.

The initial state of the nanoparticle is a mixed Pt-Ti morphology, this configuration can be used as a template for any desired structure. For instance, oxygen exposure can force core formation, low temperature annealing single core formation and high temperature annealing segregated core configuration. It is clear that thermal energy provided to the nanoparticle enhances the aggregation of Pt atoms within the nanoparticle, hence a single core is formed in the centre. It is less likely to form single core after full oxidation due to formation of smaller Pt cores at an off-centred location.

This can be explained using measured atomic spacing for Pt and Ti, presented in figure 5.1. The atomic spacing for Ti atoms is more or less close to the bulk value, however the spacing between Pt atoms is lower than the bulk value. This suggest that the Pt atoms are under strain compared to their bulk state. The Pt core attempts to release some of this strain by shifting to an off-centre location. It was also shown that even in a segregated morphology the Pt core is covered with Ti layers.

Chapter 6

X-ray Analysis of Fully Oxidised Pt-Ti

6.1 Introduction

In this chapter, the chemical states of the Pt-TiO_2 were investigated as an ensemble. X-ray Photoemission spectroscopy (XPS) was used to investigate the chemical and morphological states of nanoparticles. The focus was on two different sizes, 90 kDa and 30 kDa. The XPS measurements were used to estimate the core and shell sizes using the relative intensities of Pt and Ti element. The chemical states of both Pt and Ti were determined. Post processing method i.e. *in situ* annealing was used to investigate the heating effect on the chemical states and morphology of nanoparticles.

The XPS results were compared to GIXRF results obtained by PTB in Germany to obtain a better understanding of the nanoparticle state.

The figures presented in this chapter are not transmission function corrected, however, for quantification, the data were corrected by the transmission function.

Electronic structure and precise chemical composition of nanoparticles are crucial in their properties. These could naturally directly affect the catalytic and optical properties of the particles but more importantly, clear understanding of the mentioned characteristics of nanoparticles may be utilised to fine-tune desired properties and further examine the characteristics with greater certainty at various stages of application of such nanoparticles. In this chapter, we attempt to address analysis of the aforementioned characteristics using a combination of traditional methods of analysis.

6.2 Method

Kratos Analytical AXIS X-ray XPS setup with an Aluminium source of Kα radiation with 1486.6 eV photon energy was used. The Pt-Ti nanoparticles with two sizes of 90 kDa and 30 kDa were deposited on Si substrates through soft landing. The surface coverage was 10%. Samples were then allowed to oxidise by exposure to the ambient air. The nanoparticles were irradiated by the X-ray beam and the spectra were measured. Then samples were heated in situ to 600 ^{o}C for 20 mins and the XPS measurements were repeated to determine the chemical and morphological states. Finally the samples were exposed to the air to achieve full oxidation and the XPS measurements were repeated once more.

6.3 Chemical States

Figure 6.1(a) presents the spectrum of the Pt core in 30 kDa Pt-TiO$_2$ nanoparticles. Deconvolution of the recorded spectrum reveals the presence of two separate doublets. The measured binding energy of the Pt 4f$_{7/2}$ was 71.23 eV which corresponds to the pure Pt state. The asymmetric shape of the peak also confirms this observation. The 4f$_{7/2}$ peak at the higher binding energy was measured to be at

72.04 eV, this is close to the oxide Pt binding energy reported in the literature. Therefore it was deduced that the surface of the Pt core is in an oxide state. Figure 6.2(a) presents the spectrum of the Ti core in 30 kDa Pt-TiO_2 nanoparticles. The main observed peak is Ti $2p_{3/2}$ that appears at the binding energy of 458.49 eV, this is equal to the binding energy of TiO_2 reported in the literature, as expected. However the presence of an extra doublet with lower binding energy was also observed. The Ti $2p_{3/2}$ peak for this doublet appears to be at 456.87 eV, this is close to the binding energy reported for Ti_2O_3. Therefore, it was deduced that the Ti shell consists of mainly TiO_2 with a small amount of Ti_2O_3. The surface and interface core level shift for pure Pt, Ti and Pt-Ti is reported to be from 0.3 to 0.5 eV [114–116]. The measured values lack a specific trend within this range, it is difficult to extract the binding energy shift due to this phenomenon. The binding energies for the acquired spectra are presented in table 6.1 and table 6.2 for 30 kDa and 90 kDa nanoparticles respectively.

Figure 6.3(a) shows the spectrum of the Pt core for larger 90 kDa Pt-TiO_2 nanoparticles. Similar to the 30 kDa nanoparticles, two doublets are observed on the spectrum. The bonding energy of Pt $4f_{7/2}$ for the lower metallic peak was 71.12 eV with the higher peak appearing at 72.07 eV. This suggests similar chemical structure of the Pt core to that of the 30 kDa nanoparticle. 6.4(a) shows the chemical composition of the Ti shell. Once again, two doublets appear to exist with TiO_2 at 458.55 eV and Ti_2O_3 peak at 457.25 eV, the values are in agreement with values reported in the literature. They are also close to the values observed in 30 kDa Pt-TiO_2 nanoparticles.

Figure 6.5(a) and 6.6(a) demonstrate the acquired data for the Carbon 1s of both 30 kDa and 90 kDa samples respectively. The peak deconvolution reveals presence of C-C , C-C=O and C-O-C peak with the dominant peak being C-C, as expected. Figure 6.7 presents the spectrum of oxygen 1s for 30 kDa Pt-TiO_2. The most intense peak is the SiO_2 due to substrate, in addition to further peaks indicating

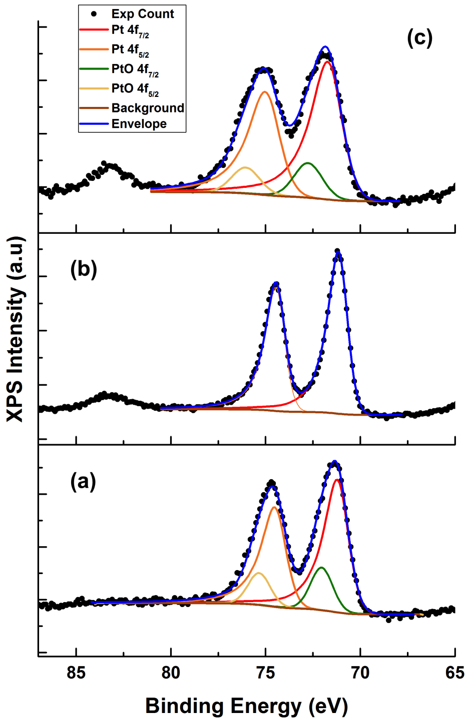

Figure 6.1: Platinum XPS spectra of 30 kDa Pt-TiO$_2$ nanoparticle. (a) fully oxidised nanoparticle before heating. (b) after in situ heating and (c) after re-exposure to the atmospheric air. Residuals of the fitted data for this figure are presented in Appendix A.

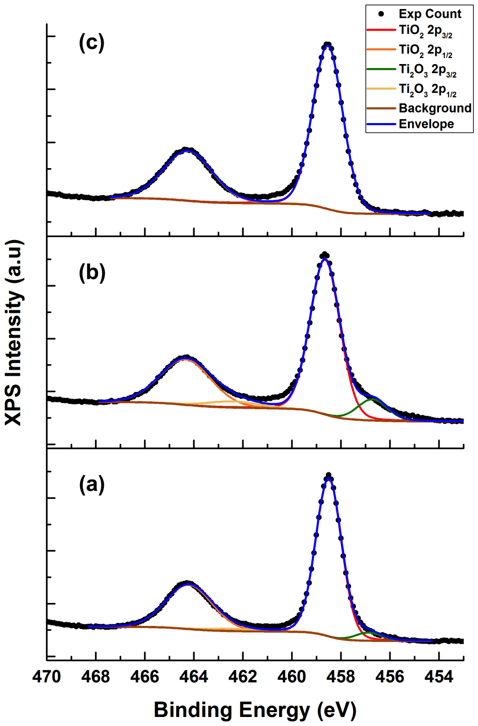

Figure 6.2: Titanium XPS spectra of 30 kDa Pt-TiO$_2$ nanoparticle. (a) fully oxidised nanoparticle before heating. (b) after in situ heating and (c) after re-exposure to the atmospheric air.

the presence of organic C-O and C=O as well as metal oxide. Table 6.3 presents Pt and Ti signal ratio. It can be seen that values are close to the Pt to Ti ratio in the sputtering target.

6.3.1 Ensemble Core-Shell Calculations Using T$_{NP}$ Method

It has been demonstrated previously that the XPS data contains useful information about the structure. The method is explained by Shard [117, 118], a summery of which, as it applies to the present thesis, is provided here. To simplify the argument, dimensionless terms can be derived as follows:

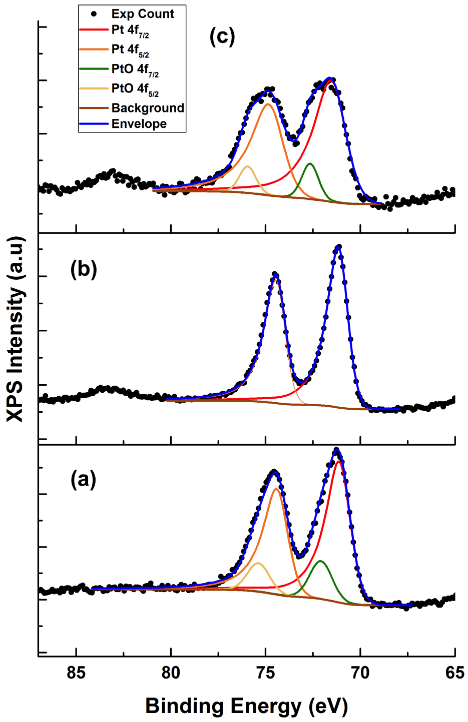

FIGURE 6.3: Platinum XPS spectra of 90 kDa Pt-TiO_2 nanoparticle. (a) fully oxidised nanoparticle before heating. (b) after in situ heating and (c) after re-exposure to the atmospheric air

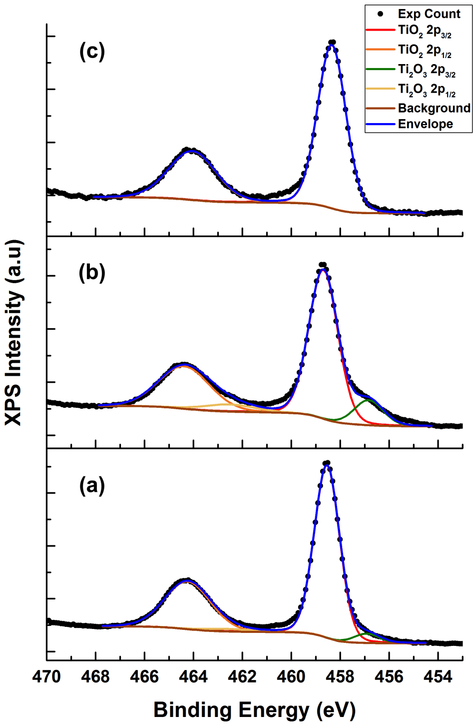

FIGURE 6.4: Titanium XPS spectra of 90 kDa Pt-TiO_2 nanoparticle. (a) fully oxidised nanoparticle before heating. (b) after in situ heating and (c) after re-exposure to the atmospheric air

TABLE 6.1: Binding energy values for 30 kDa Pt-TiO_2 nanoparticles.

Species	Initial (eV)	After Heating (eV)	After Air Exposure (eV)	Literature (eV)
TiO_2 $2p_{3/2}$	458.55	458.68	458.51	458.5
TiO_2 $2p_{1/2}$	464.25	464.38	464.21	464.2
Ti_2O_3 $2p_{3/2}$	457.09	456.89	-	457.8
Ti_2O_3 $2p_{1/2}$	462.79	462.59	-	463.5
Pt $4f_{7/2}$	71.12	71.16	71.44	71
Pt $4f_{5/2}$	74.42	74.46	74.74	74.35
PtO $4f_{7/2}$	72.07	-	72.71	72.4
PtO $4f_{5/2}$	75.37	-	76.01	75.75
C-C 1s	284.88	284.79	284.93	284.8
C-O-C 1s	288.34	288.58	288.59	286
O-C=O 1s	286.12	286.25	286.12	288.5

Table 6.2: Binding energy values for 90 kDa Pt-TiO_2 nanoparticles.

Species	Initial (eV)	After Heating (eV)	After Air Exposure (eV)	Literature (eV)
TiO_2 $2p_{3/2}$	458.49	458.64	458.54	458.5
TiO_2 $2p_{1/2}$	464.19	464.34	464.24	464.2
Ti_2O_3 $2p_{3/2}$	457.87	456.71	-	457.8
Ti_2O_3 $2p_{1/2}$	462.57	462.54	-	463.5
Pt $4f_{7/2}$	71.23	71.16	71.73	71
Pt $4f_{5/2}$	74.53	74.46	75.03	74.35
PtO $4f_{7/2}$	72.04	-	72.75	72.4
PtO $4f_{5/2}$	75.34	-	76.05	75.75
C-C 1s	284.88	284.83	284.85	284.8
C-O-C 1s	288.08	288.22	288.02	286
O-C=O 1s	286.14	286.49	286.47	288.5

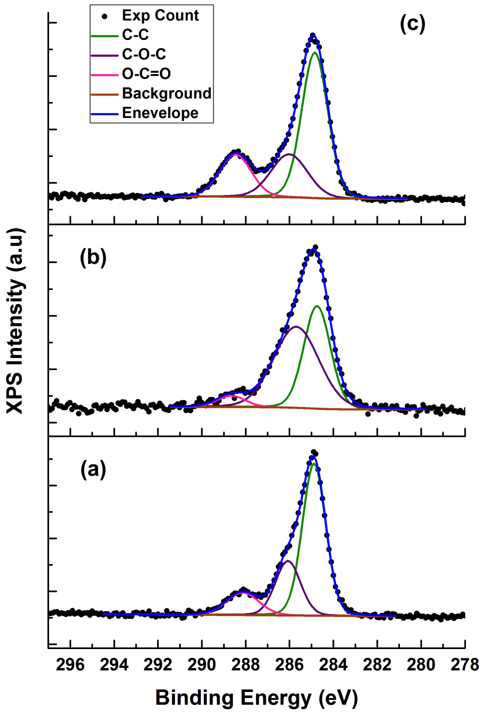

Figure 6.5: Carbon XPS spectra of 30 kDa Pt-TiO_2 nanoparticle. (a) fully oxidised nanoparticle before heating. (b) after in situ heating and (c) after re-exposure to the atmospheric air.

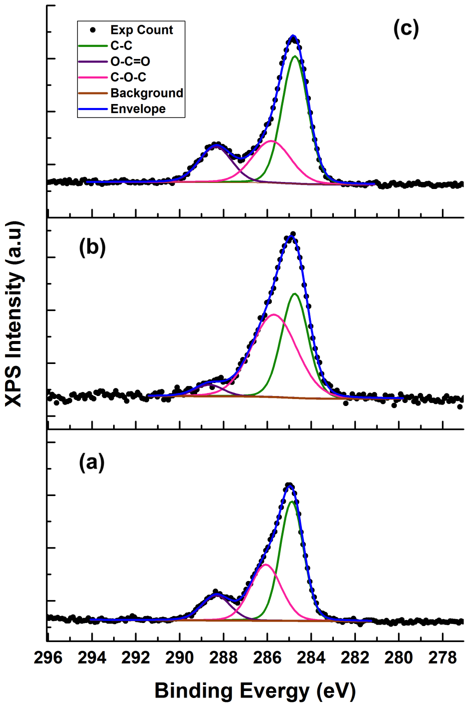

Figure 6.6: Carbon XPS spectra of 90 kDa Pt-TiO_2 nanoparticle. (a) fully oxidised nanoparticle before heating. (b) after in situ heating and (c) after re-exposure to the atmospheric air.

Table 6.3: Pt to Ti ratio from XPS spectrum of Pt-TiO_2 nanoparticles.

Ratio of Pt to Ti	Initial	After Heating	After Air exposure
30 kDa nanoparticle	14.67±0.53	15.65±0.93	15.11±1.1
90 kDa nanoparticle	16.00±0.45	17±0.94	17.01±0.78

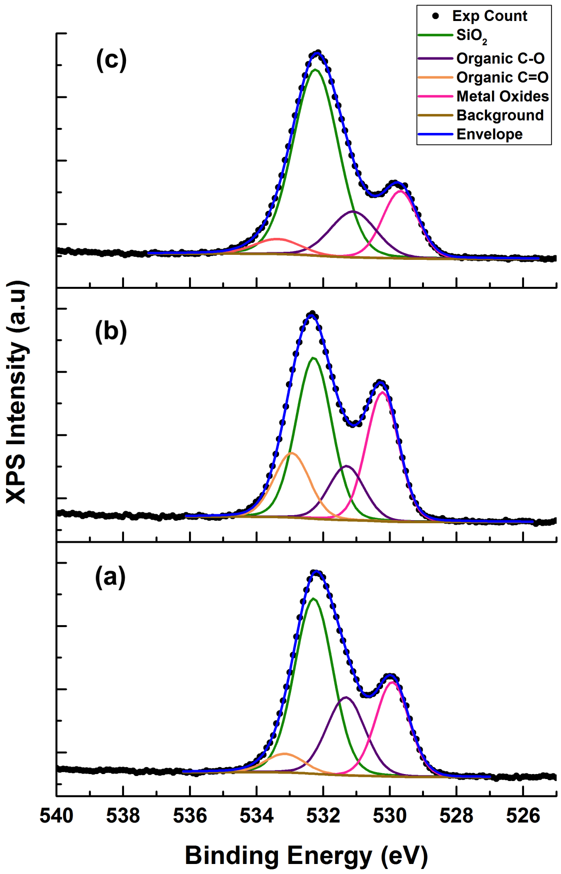

Figure 6.7: Oxygen XPS spectra of 30 kDa Pt-TiO_2 nanoparticle. (a) fully oxidised nanoparticle before heating. (b) after in situ heating and (c) after re-exposure to the atmospheric air.

$$A = \frac{I_1 I_2^{\infty}}{I_2 I_1^{\infty}} \tag{6.1}$$

$$B = \frac{L_{1,a}}{L_{2,a}} \tag{6.2}$$

$$C = \frac{L_{1,a}}{L_{1,b}} \tag{6.3}$$

where I_i is the measured XPS intensity and I_i^{∞} is the measured or calculated intensity for the pure material of the unique photoelectrons from the shell, i = 1, and the core i = 2. $L_{i,j}$ is the attenuation length of photoelectrons arising from material i travelling through material j, where j = a represents the shell and j = b represents the core. The core radius of the particle, R, and shell thickness, T, are expressed in units of $L_{1,a}$. For microscopic spherical particles where R is much larger but not large enough for the X-ray shadowing effects become significant, the thickness of the overlayer can be calculated using

$$T_{R\to\infty} = \frac{0.75A^{3.6}ln(A)B^{-0.9} + 4.3AB^{-0.41}}{A^{3.6} + 8.9} \tag{6.4}$$

For very small values of R and T where the product of ABCR approaches zero, the value T_0 can calculated by

$$T_0 = R[(ABC + 1)^{1/3} - 1] \tag{6.5}$$

However, when the size of the nanoparticle and the attenuation length are comparable, equations 6.4 and 6.5 are not suitable. The relationship between T and R for fixed values of A,B and C and moderate values R is described by the empirical relations shown below

$$T_{R\sim 1} = \frac{T_{R\to\infty}R}{R + \alpha} \tag{6.6}$$

where α is a function of A,B and C and it can be found by fitting the numerical data. The accurate value for very small particles provided from equation 6.5 can be used combined with equation 6.6 to provide a suitable estimate of shell thickness over a range of R,

$$T_{NP} = \frac{T_{R\sim 1} + \beta T_0}{1 + \beta} \tag{6.7}$$

where the numerical analysis can be used to obtain an equation for α and β as shown

$$\alpha = \frac{1.8}{A^{0.1}B^{0.5}C^{0.4}} \tag{6.8}$$

$$\beta = \frac{0.13\alpha^{2.5}}{R^{1.5}} \tag{6.9}$$

The HAADF STEM images acquired from the Pt-TiO$_2$ nanoparticles provide a significantly more accurate value on the average Pt core size than that of the TiO$_2$ shell thickness. This is due to fact that STEM imaging is heavily dependent on the atomic number of elements. However, the empirical T$_{NP}$ calculation can be used to verify and examine the STEM analysis. On the other hand, comparison of the two data set can be used to put the T$_{NP}$ method to a further experimental test. The single Pt core size of 30 kDa Pt-TiO$_2$ nanoparticle was calculated to be 1.0 ± 0.2 nm using the HAADF STEM data. This value was used as the Pt core size for the T$_{NP}$ method. The total Pt and Ti intensity was measured from the spectra and used to calculate the thickness of the TiO$_2$ shell. The T$_{NP}$ calculation provides a shell thickness of 1.0 ± 0.2 nm. This value is slightly larger than the shell calculation obtained from the analysis of the STEM data (0.8 ± 0.4 nm).

The T$_{NP}$ calculation is based on a perfectly centred core. In order to examine the core position in 30 kDa Pt-TiO$_2$ nanoparticles, FIJI was used to determine the distance between the centre of the core to the centre of the shell. Figure 6.8 presents a histogram of the statistical analysis. It can be seen that in majority of the nanoparticles the distance between the centre of Pt core and shell was less than 0.1 nm.

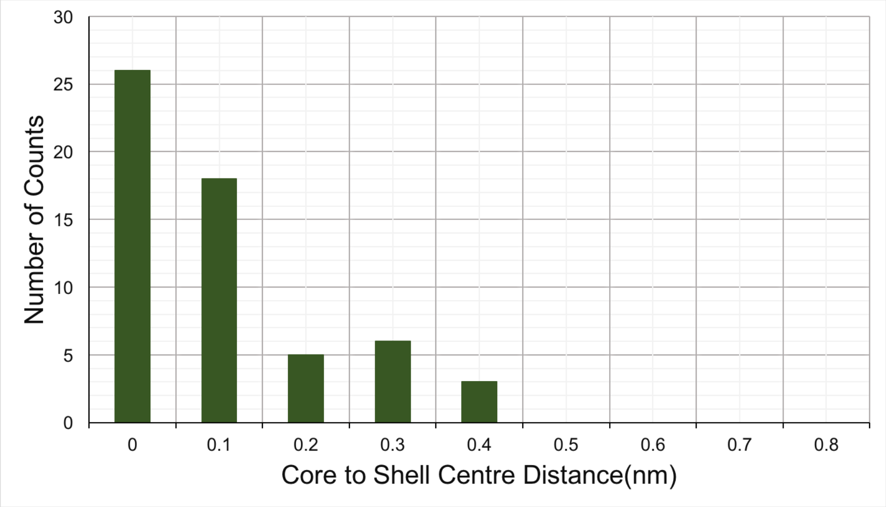

FIGURE 6.8: Histogram of the distance between the centre of the core to the centre of the shell.

6.4 Thermal Annealing Effect

The available *in situ* heating feature of the XPS setup was used to investigate chemical configuration of the nanoparticles after thermal manipulation. In order to achieve this 30 kDa and 90 kDa Pt-TiO_2 nanoparticles samples were loaded into the XPS, then the samples were thermally annealed at 600 ^{o}C for 20 mins. Figure 6.1(b) presents the Pt 4f spectrum of 30 kDa nanoparticle. The spectrum shows disappearance of the PtO peak, the asymmetric shape of the peaks also confirms the presence of the metal Pt only. The metal Pt $4f_{7/2}$ doublet binding energy was 71.16 eV which is close to the binding energy before annealing. (see table 6.1). Similar chemical reduction was observed for the oxide Ti shell. The relative intensity of Ti_2O_3 peak was increased after annealing, demonstrated in figure 6.2(b). The binding energies were also consistent with the initial state. Figure 6.5(b) shows a relative reduction in the C-C peak which suggests that during annealing carbon contamination was evaporated off the sample. The oxygen 1s spectrum after anneal indicates reduction of Si and oxidation of carbon on the surface, shown in figure 6.7(b).

Similar observation was made for 90 kDa nanoparticles. Figure 6.3(b) presents the Pt 4f spectrum of the heavier 90 kDa nanoparticles, the Pt is fully reduced to its metal state, and the binding energy is consistent to the initial metallic binding energy. The TiO_2 shell also shows reduction after heating, as demonstrated in figure 6.4(b), the relative intensity of Ti_2O_3 doublet was increased in comparison to the initial state. The carbon also demonstrate similar features to the 30 kDa nanoparticles, (see figure 6.6(b)). It is clear that in both 30 kDa and 90 kDa nanoparticle samples a reduction process was taking place. The Pt was reduced to the pure metallic Pt and a small portion of the Ti shell was reduced to a less stable Ti_2O_3 state.

The samples were then exposed to the atmospheric air for prolong time. Figure 6.1(c) presents the spectrum of Pt 4f after air exposure, it is clear that the Pt core formed an oxide layer once again. The binding energy was consistent to the initial state. Figure 6.2(c) shows the spectra of the Ti shell. It can be seen that the less stable Ti_2O_3 state has disappeared and the Ti shell is in a fully oxidised state. Analysis on the spectra of Pt 4f and Ti 2p of the 90 kDa nanoparticles suggests similar behaviour. Figures 6.3(c) and 6.4(c) presents the spectra of Pt 4f and Ti 2p of 90 kDa nanoparticles accordingly. The presence of oxide states is clear on the Pt core and also the fully oxidised state of the Ti shell. Figure 6.5(c) and 6.6(c) present the carbon 1s spectra after air exposure for both samples. It can be seen that the C-C peak has the highest intensity which suggest the carbon contamination recovered after handling and exposure to air. The oxygen also recovered its original state as it is demonstrated in figure 6.7(c). Table 6.3 presents the Pt to Ti ratios at every stage. The initial value is close to the Pt to Ti ratio of the sputtering target. The value stays constant after heating and after storage. It can be deduced that there was no loss of material due to the heating.

6.5 Grazing Incidence X-ray Fluorescence Analysis

In collaboration with Physikalisch-Technische Bundesanstalt(PTB), 30 kDa Pt-TiO_2 nanoparticles were also investigated by Grazing Incidence X-ray Fluorescence Analysis (GIXRF) for surface coverage and equipment tuning in addition to Near-Edge X-ray Absorption Fine Structure (NEXAFS) for probing the binding state of the titanium shell.

Figure 6.9 presents a schematic drawing of the experimental setup used for XRF and GIXRF. The samples were aligned using translations and rotation motors to the pivot point of the chamber with respect to the incident excitation radiation. A radiometrically calibrated photodiode was used to measure the flux of the excitation radiation. GIXRF measurements are a variation of the incident angle around the critical angle of total external reflection when the fluorescence radiation is detected. The signal detected is strongly dependent on the angle of incident. The shape of the fluorescence line intensity is also different for nanoparticles, thin films or implantation profiles.

The excitation energy of 12.5 KeV was used in reference-free GIXRF, since this is above the titanium Kα and the platinum L3 edges. Figure 6.10 demonstrates the fluorescence spectrum for the sample with surface coverage of 5.0 %. The Ti Kα and Kβ fluorescence lines are clearly visible as well as the Pt Lα line. The Si from the substrate is also visible in addition to minor contamination such as Ca, Fe, Ni, Cu and Zn. These contaminants could be from the cleaning or handling process. The mass ratio Ti:Pt obtained from reference-free XRF measurements was 0.63:0.37 which is reasonably close to the mass ratio of the sputtering target 0.75:0.25 as well as values form the XPS measurements.

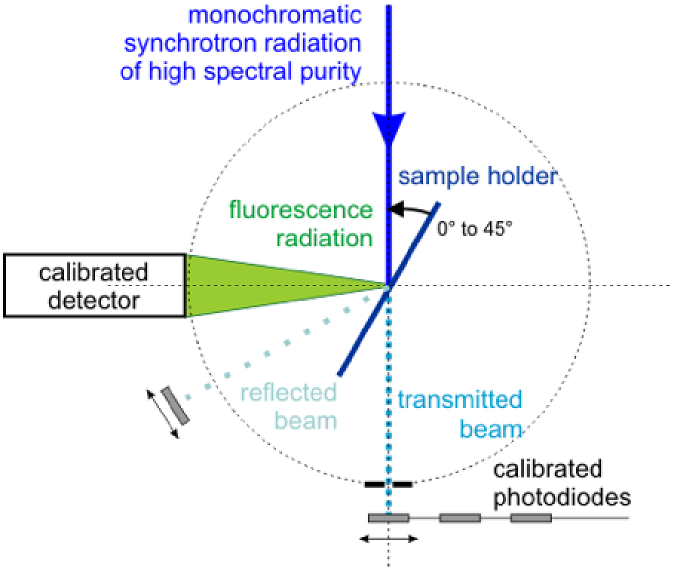

Figure 6.9: Scheme of the experimental setup used for the measurements of the X-ray fluorescence lines in various geometries. The direct beam, the reflected beam and (if the sample allows for transmission of the excitation radiation) the transmitted beam can be detected using calibrated photodiodes. Figure and caption from PTB.

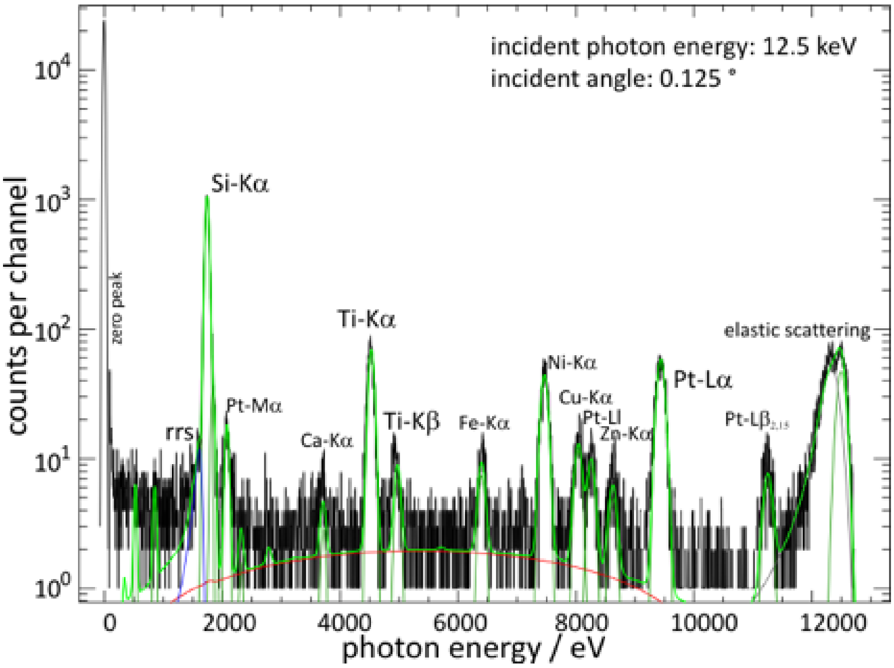

Figure 6.10: GIXRF-spectrum of a sample with nominal 5 % surface coverage as an example of the determination of the elemental composition. Titanium and platinum can be identified. Figure and caption from PTB.

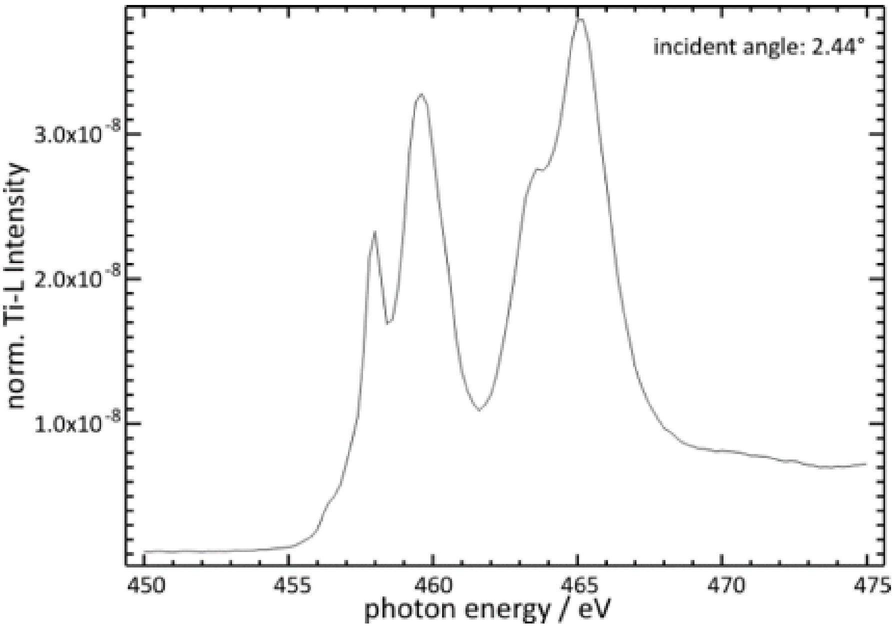

Figure 6.11: Ti L3,2 NEXAFS measurements of sample with 5 % surface coverage. The incidence angle was chosen to be below the critical angle of total reflection in order to receive information about the core-shell nanoparticles, located at the surface of the substrate. The shape of the curves are similar and suggests the same chemical binding state, titanium dioxide. Figure and caption from PTB.

Figure 6.11 presets the Ti L3,2 NEXAFS spectra of the samples with a surface coverage of 5 %. The incidence angle was set below to the critical angle of total reflection. There are dominant peaks of the L3 absorption edge at 458 eV, 459.6 eV, and 460.4 eV, which are due to splitting caused by the crystal field surrounding the oxygen atoms. This behaviour can also be observed at the L2 edge, but these peaks are broadened due to the shorter lifetime. Thus, one can conclude that titanium dioxide is the dominant state of the Ti shell.

6.6 Discussion

The XPS provided valuable insight into the chemical composition of the Pt-TiO_2 nanoparticles. The two sizes demonstrated significantly similar chemical characteristics. It was shown that the initial state of the fully oxidised nanoparticle contains a Pt core which consists of metallic Pt with a Pt oxide surface layer. This was verified by comparing the binding energies to binding energies reported in the literature. The Ti shell was almost fully TiO_2, however small traces of Ti_2O_3 was observed in the initial state. *in situ* annealing of the samples demonstrated oxygen reduction. The Pt core was fully reduced to pure metallic state. A portion of the Ti_2O_3 were also increased after annealing, it should be noted that the annealing temperature was lower than the bulk TiO_2 reduction temperature which is reported to be above 1000 ^{o}C. Analysis of the carbon and the oxygen spectra also demonstrated oxygen reduction on the samples induced by annealing.

The binding energies are also consistent between the two samples as well as after and before annealing. The size of the nanoparticles influence the binding energies at the nano range, mainly due to the strains induced in the nanoparticle by a much higher surface atom to bulk ratio compared to bulk. Therefore, the consistent binding energies between the two sizes confirms previous STEM analysis that the average core size is similar between the two samples. In addition, the binding energies are consistent before and after thermal manipulation which suggests that the heating did not induce aggregation of the nanoparticles on the substrate.

The XPS data was used to complete the analysis obtained from the HAADF STEM data. The HAADF STEM imaging is a powerful tool in analysis of heavy metals. However, due to the nature of the technique, it is not as reliable for light elements. Therefore, XPS quantification methods such as the T_{NP} used in this work, can complete the analysis. In addition both methods can be used for mutual verification. For instance, the core size value obtained from the STEM data was used with the T_{NP} method to obtain a value for the total size of the nanoparticle. The thickness calculation from both methods agreed within the errors. The relative position of the core inside the nanoparticle was also investigated. It was observed that statistically the Pt core positions in the centre of the 30 kDa nanoparticles. The XPS measurements as well as the GIXRF and NEXAFS measurements demonstrated that the Pt to Ti ratio of the nanoparticles is consistent to the ratio of the two metals in the sputtering target.

Chapter 7

Conclusion

The aim of this work was to address two main issues, firstly the importance of oxygen on the morphology of metallic nanoparticles and secondly the ability of morphological modification through thermal annealing of the nanoparticles. Initially, Pt-Ti nanoparticles were investigated after exposure to air. It was observed that the 30 kDa nanoparticles demonstrate single core morphology, however increasing the size to 90 kDa, results in a multi core morphology. The nanoparticles were then examined with minimal air exposure, this resulted in an alloy morphology. This highlighted the effect of oxygen on the final morphology of this bimetallic system. DFT calculation was performed to further develop the knowledge of the system. The results show that as the oxidation level increases, core formation was more stable. The fully oxidised Pt-Ti nanoparticle demonstrates single core morphology. This is in agreement with observation of single core structure in smaller 30 kDa nanoparticle. This was expected, as the size of smaller nanoparticle is more comparable to theoretically analysed nanoparticle.

The effect of the electron beam on the nanoparticle is often neglected in analysis of both pure or bimetallic nanoparticle.It was demonstrated that the interaction of the electron beam with the nanoparticle prior to air exposure, induces a single core morphology in the 90 kDa nanoparticle. The additional energy provided by the electron beam, drives nucleation of the Pt atoms within the nanoparticle. This was confirmed by thermal annealing of the nanoparticle to modify the structure to single core morphology. The morphology was also modified to a segregated core-shell by increasing the thermal energy. The process was investigated in great detail using the DENS heating stage under the electron beam. The induction of single core morphology requires a surface oxidised nanoparticle. The single core formation was not observed in the case of heating multi-core morphology.

Finally, X-ray analysis was used to determine the electronic structure of the system. Both 30 kDa and 90 kDa Pt-TiO_2 nanoparticles, demonstrate identical chemical structure. The majority of the Pt core is in pure metallic state, with a small traces of oxide states. On the other hand, the Ti shell was almost fully in TiO_2 state with small amount of lower oxide state i.e. Ti_2O_3. heating of the nanoparticle under vacuum induced chemical reduction of both Pt and Ti. The Pt core was changed to pure metallic after the heating process. The ratio of Ti_2O_3 to TiO_2 was also increased. However, this reduction was reversed after re-exposure to the atmospheric air. The relative XPS intensity of Pt to Ti was used in the T_{NP} method to calculate the shell thickness of the single core 30 kDa Pt-TiO_2. The shell thickness obtained from the HAADF STEM intensity and the XPS intensity were comparable within the errors. The chemical state of the nanoparticles was also investigated using GIXRF and NEXAFS measurements to confirm the results obtained by the XPS.

In conclusion, the outcome of this work highlights the importance of oxygen exposure in the stability of multi-metallic nanoparticles. This information is crucial for any large scale application of such particles. In addition, it was demonstrated that the final morphology of the nanoparticle can be modified and manipulated through thermal heating. The findings of this work could be expanded by varying the ratio of Pt to Ti in the oxidised state. The inert atmosphere transfer system could also be improved in the STEM loading part to fully eliminate oxygen exposure. In this way the theoretical work becomes even more strongly comparable to experimental results.

For instance, the ratio of Pt and Ti can be varied more precisely if a dual magnetron sputtering setup is utilised whereby two pure Pt and Ti target could be used to finely determine the ratios by individually adjusting sputtering power. Furthermore, if the the inert atmosphere system is improved to eliminate exposure to oxygen completely, utilising a STEM arm that is capable of introducing gas during the imaging process would allow imaging the formation of multi core structure in real time. Additionally this setup allows introduction of hydrogen gas at high temperatures to potentially reverse the oxidation process by reducing the nanoparticle to a fully unoxidised state in real time.

A further improvement could be employing an XPS setup that is capable of direct connection to the cluster source so that the samples can be transferred directly without any oxygen exposure between the two steps, this would allow XPS analysis of the nanoparticles prior to any oxygen exposure which is currently unavailable.

Finally, as the system is highly relevant to various catalytic reactions as discussed in earlier chapters, the dependence of catalytic properties of the studied system can be examined by methods such as electro-chemistry to determine whether any of the induced structures in this work provide and improvement or deterioration of the known catalytic properties of the system.

Appendix A

Residuals of Data Presented in Figure 6.1

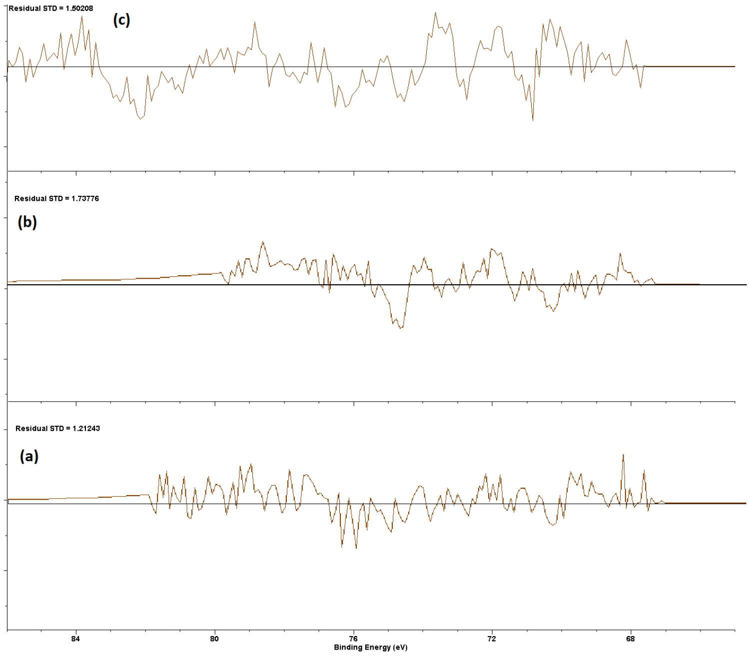

FIGURE A.1: Residual of the fit presented in figure 6.1 of platinum XPS spectra of 30 kDa Pt-TiO_2 nanoparticle. (a) residual of fully oxidised nanoparticle before heating. (b) after in situ heating and (c) after re-exposure to the atmospheric air.

Bibliography

[1] Jaison Jeevanandam, Ahmed Barhoum, Yen S. Chan, Alain Dufresne, and Michael K. Danquah. Review on nanoparticles and nanostructured materials: history, sources, toxicity and regulations. *Beilstein Journal of Nanotechnology*, 9:1050–1074, 2018. ISSN 2190-4286.

[2] Rajib Ghosh Chaudhuri and Santanu Paria. Core/shell nanoparticles: Classes, properties, synthesis mechanisms, characterization, and applications. *Chemical Reviews*, 112(4):2373–2433, 2012.

[3] Anu Mary Ealias and M P Saravanakumar. A review on the classification, characterisation, synthesis of nanoparticles and their application. *IOP Conference Series: Materials Science and Engineering*, 263(3):032019, 2017.

[4] Juha Samela and Kai Nordlund. Emergence of non-linear effects in nanocluster collision cascades in amorphous silicon. *New Journal of Physics*, 10 (2):023013, 2008.

[5] Roy Johnston. *Atomic and molecular clusters.* Taylor & Francis, London; New York, 2002. ISBN 0748409300 9780748409303 0748409319 9780748409310.

[6] Ahmed Abdela. Gas Phase Generation and Deposition of Size-Selected Metal Clusters. *The University of Birmingham*, (July), 2013.

[7] Gaurav Sharma, Vinod Kumar Gupta, Shilpi Agarwal, Amit Kumar, Samariti Thakur, and Deepak Pathania. Fabrication and characterization of fe@mopo nanoparticles: Ion exchange behavior and photocatalytic activity against malachite green. *Journal of Molecular Liquids*, 219:1137 – 1143, 2016.

[8] Naoki Toshima and Tetsu Yonezawa. Bimetallic nanoparticles-novel materials for chemical and physical applications. *New J. Chem.*, 22:1179–1201, 1998.

[9] J. K. Norskov, J. Rossmeisl, A. Logadottir, L. Lindqvist, J. R. Kitchin, T. Bligaard, and H. Johanson. Origin of the overpotential for oxygen reduction at a fuel-cell cathode. *The Journal of Physical Chemistry B*, 108(46): 17886–17892, 2004.

[10] Jeffrey Greeley and Nenad M. Markovic. The road from animal electricity to green energy: combining experiment and theory in electrocatalysis. *Energy Environ. Sci.*, 5:9246–9256, 2012.

[11] Greeley J., Rossmeisl J., Hellmann A., and Norskov J. K. Theoretical trends in particle size effects for the oxygen reduction reaction. *J. Phys. Chem. C*, page 1209.

[12] Paul C. Jennings, Bruno G. Polleta, and L. Johnston Roy. Theoretical studies of pt–ti nanoparticles for potential use as pemfc electrocatalysts. *Phys. Chem. Chem. Phys*, 14:3134–3139, 2012.

[13] Paul C. Jennings, Hristiyan A. Aleksandrov, Konstantin M. Neyman, and L. Johnston Roy. O2 dissociation on m@pt core-shell particles for 3d, 4d, and 5d transition metals. *J. Phys. Chem. C*, 119:11031–11041, 2015.

[14] Riccardo Ferrando, Julius Jellinek, and Roy L. Johnston. Nanoalloys: From theory to applications of alloy clusters and nanoparticles. *Chemical Reviews*, 108(3):845–910, 2008.

[15] Zhiming Cui, Hao Chen, Mengtian Zhao, Daniel Marshall, Yingchao Yu, and Francis J Disalvo. Synthesis of structurally ordered pt 3 ti and pt 3 v nanoparticles as methanol oxidation catalysts. *J. Am. Chem. Soc*, 136: 10206–10209, 2014.

[16] Govindachetty Saravanan, Hideki Abe, Ya Xu, Nobuaki Sekido, Hirohito Hirata, Shin-ichi Matsumoto, Hideki Yoshikawa, and Yoko Yamabe-mitarai. Pt 3 Ti Nanoparticles : Fine Dispersion on SiO 2 Supports , Enhanced Catalytic CO Oxidation , and Chemical Stability at Elevated Temperatures. *Langmuir*, 26(26):11446–11451, 2010.

[17] Hideki Abe, Futoshi Matsumoto, Laif R Alden, Scott C Warren, Héctor D Abruña, and Francis J Disalvo. Electrocatalytic Performance of Fuel Oxidation by Pt 3 Ti Nanoparticles. *J. Am. Chem. Soc*, (13):5452–5458, 2008.

[18] Errun Ding, Karren L More, and Ting He. Preparation and characterization of carbon-supported PtTi alloy electrocatalysts. *Journal of Power Sources*, 175:794–799, 2008.

[19] P Davide Cozzoli, Elisabetta Fanizza, Roberto Comparelli, M Lucia Curri, Angela Agostiano, Dipartimento Chimica, V Uni, Via Orabona, Processi Chimico, Fisici Ipcf, and Via Orabona. Role of Metal Nanoparticles in TiO 2 / Ag Nanocomposite-Based Microheterogeneous Photocatalysis. *J. Am. Chem. Soc*, pages 9623–9630, 2004.

[20] Ying Li, Wei-ning Wang, Zili Zhan, Myung-heui Woo, Chang-yu Wu, and Pratim Biswas. Applied Catalysis B : Environmental Photocatalytic reduction of CO 2 with H 2 O on mesoporous silica supported Cu / TiO 2

catalysts. *"Applied Catalysis B, Environmental"*, 100(1-2):386–392, 2010. ISSN 0926-3373.

[21] Fatih Sen and Gulsun Gokagac. Different Sized Platinum Nanoparticles Supported on Carbon : An XPS Study on These Methanol Oxidation Catalysts. *J. Phys. Chem. C*, pages 5715–5720, 2007.

[22] Evgeny I. Vovk, Alexander V. Kalinkin, Mikhail Yu. Smirnov, Igor O. Klembovskii, and Valerii I. Bukhtiyarov. Xps study of stability and reactivity of oxidized pt nanoparticles supported on tio2. *The Journal of Physical Chemistry C*, 121(32):17297–17304, 2017.

[23] Kyriakos Bourikas, Christos Kordulis, and Alexis Lycourghiotis. Titanium Dioxide (Anatase and Rutile): Surface Chemistry , Liquid-Solid Interface Chemistry , and Scientific Synthesis of Supported Catalysts. *Chem. Rev*, 114:9754–9823, 2014.

[24] Frigyes Solymosi and Imre Tomb. Photocatalytic reaction of H20 + CO2 over pure and doped Rh / TiO2. *Catalysis Letters*, 27:61–65, 1994.

[25] Susanta K Mohapatra, Narasimharao Kondamudi, Subarna Banerjee, and Mano Misra. Functionalization of Self-Organized TiO2 Nanotubes with Pd Nanoparticles for Photocatalytic Decomposition of Dyes under Solar Light Illumination. *Langmuir*, (19):11276–11281, 2008.

[26] Vaidyanathan Subramanian, Eduardo E Wolf, and Prashant V Kamat. Influence of Metal / Metal Ion Concentration on the Photocatalytic Activity of TiO 2 - Au Composite Nanoparticles. *Langmuir*, (25):469–474, 2003.

[27] Hexing Li, Zhenfeng Bian, Jian Zhu, Yuning Huo, Hui Li, and Yunfeng Lu. Mesoporous Au / TiO 2 Nanocomposites with Enhanced Photocatalytic Activity. *J. Am. Chem. Soc*, (101):4538–4539, 2007.

[28] N Rajalakshmi, N Lakshmi, and K S Dhathathreyan. Nano titanium oxide catalyst support for proton exchange membrane fuel cells. *International Journal of Hydrogen Energy*, 33(24):7521–7526, 2008. ISSN 0360-3199.

[29] Gratian R Bamwenda, Susumu Tsubota, Toshiko Nakamura, and Masatake Haruta. Photoassisted hydrogen production from a water-ethanol solution : a comparison of activities of Au-TiO2 and Pt-TiO2. *Journal of Photochemistry and Photobiology A: Chemistry*, 89:177–189, 1995.

[30] Masakazu Anpo, Hiromi Yamashita, and Shaw Ehara Yuichi Ichihashi. Photocatalytic reduction of co2 with h20 on various titanium oxide catalysts. *Journal of Electroanalytical Chemistry*, 396:21–26, 1995.

[31] Masakazu Anpo. Photocatalysis on titanium oxide catalysts approaches in achieving highly efficient reactions and realizing the use of visible light. *Catalysis Surveys*, page 1, 1997.

[32] Jiaguo Yu, Lifang Qi, and Mietek Jaroniec. Hydrogen production by photocatalytic water splitting over pt/tio2 nanosheets with exposed (001) facets. *The Journal of Physical Chemistry C*, 114(30):13118–13125, 2010.

[33] Xiaowei Teng, Donald Black, Neil J. Watkins, Yongli Gao, and Hong Yanga. Platinum-maghemite core-shell nanoparticles using a sequential synthesis. *Nano Letters*, Vol. 3(No. 2):261–264, 2003.

[34] Idalia Bilecka, Igor Djerdj, and Markus Niederberger. One-minute synthesis of crystalline binary and ternary metal oxide nanoparticles. *Chem Commun.*, 886(886-888), 2008.

[35] A. Caillard, S. Cuynet, T. Lecas, P. Andreazza, M. Mikikian, A l Thomann, and P. Brault. Pdpt catalyst synthesized using a gas aggregation source and magnetron sputtering for fuel cell electrodes. *J. Phys D: Appl. Phys*, 48: 475302, 2015.

[36] Beatriz Roldan Cuenya. Synthesis and catalytic properties of metal nanoparticles size, shape, support, composition, and oxidation state effects. *Thin Solid Films*, 518:3127–3150, 2010.

[37] A. V. Nikam, B. L. V. Prasad, and A. A. Kulkarni. Wet chemical synthesis of metal oxide nanoparticles: a review. *CrystEngComm*, 20:5091–5107, 2018.

[38] Brian L. Cushing, Vladimir L. Kolesnichenko, and Charles J. O'Connor. Recent advances in the liquid-phase syntheses of inorganic nanoparticles. *Chemical Reviews*, 104(9):3893–3946, 2004.

[39] Rishu Katwal, Harpreet Kaur, Gaurav Sharma, Mu. Naushad, and Deepak Pathania. Electrochemical synthesized copper oxide nanoparticles for enhanced photocatalytic and antimicrobial activity. *Journal of Industrial and Engineering Chemistry*, 31:173 – 184, 2015.

[40] Gaurav Sharma, Amit Kumar, Shweta Sharma, Mu Naushad, Ram Prakash, Zeid A Alothman, and Genene Tessema. Science Novel development of nanoparticles to bimetallic nanoparticles and their composites : A review. *Journal of King Saud University - Science*, 2017.

[41] J. Belloni. Nucleation, growth and properties of nanoclusters studied by radiation chemistry: Application to catalysis. *Catalysis Today*, 113(3):141 – 156, 2006.

[42] V. M. Chakka, B. Altuncevahir, Z. Q. Jin, Y. Li, and J. P. Liu. Magnetic nanoparticles produced by surfactant-assisted ball milling. *Journal of Applied Physics*, 99(8):08E912, 2006.

[43] V. M. Chakka, B. Altuncevahir, Z. Q. Jin, Y. Li, and J. P. Liu. Magnetic nanoparticles produced by surfactant-assisted ball milling. *Journal of Applied Physics*, 99(8):08E912, 2006.

[44] O. F. Hagena and W. Obert. Cluster formation in expanding supersonic jets: Effect of pressure, temperature, nozzle size, and test gas. *The Journal of Chemical Physics*, 56(5):1793–1802, 1972.

[45] C. Binns. Nanoclusters deposited on surfaces. *Surface Science Reports*, 44 (1):1 – 49, 2001.

[46] Walt A. de Heer. The physics of simple metal clusters: experimental aspects and simple models. *Rev. Mod. Phys.*, 65:611–676, Jul 1993.

[47] P Eichberger, C Winkler, and T D Mtirk. Time-of-flight apparatus for studies of pulsed neutral van-der-waals-cluster production and of the interaction between electrons and van der waals clusters at high electron energy resolution. *International Journal of Mass Spectrometry and Ion Processes*, 129:57 – 65, 1993.

[48] W Marine, L Patrone, B Luk'yanchuk, and M Sentis. Strategy of nanocluster and nanostructure synthesis by conventional pulsed laser ablation. *Applied Surface Science*, 154-155:345 – 352, 2000.

[49] Alfredo M. Morales and Charles M. Lieber. A laser ablation method for the synthesis of crystalline semiconductor nanowires. *Science*, 279(5348): 208–211, 1998.

[50] Pavel Solar, Oleksandr Polonskyi, Ansgar Olbricht, Alexander Hinz, Artem Shelemin, Ondrej Kylian, Andrei Choukourov, Franz Faupel, and Hynek Biederman. Single-step generation of metal-plasma polymer multicore shell nanoparticles from the gas phase. *Scientific Reports*, 7:6–11, 2017.

[51] F. Frank, W. Schulze, B. Tesche, J. Urban, and B. Winter. Formation of metal clusters and molecules by means of the gas aggregation technique and characterisation of size distribution. *Surface Science*, 156:90 – 99, 1985.

[52] Z. Y. Li, J. P. Wilcoxon, F. Yin, Y. Chen, R. E. Palmer, and R. L. Johnston. Structures and optical properties of 4-5 nm bimetallic agau nanoparticles. *Faraday Discuss.*, 138:363–373, 2008.

[53] A. N. Dobrynin, D. N. Ievlev, G. Verschoren, J. Swerts, M. J. Van Bael, K. Temst, P. Lievens, E. Piscopiello, G. Van Tendeloo, S. Q. Zhou, and A. Vantomme. Atomic-scale modification of hybrid fept cluster-assembled films. *Phys. Rev. B*, 73:104421, 2006.

[54] L. Martnez, M. Daz, E. Romn, M. Ruano, D. Llamosa P., and Y. Huttel. Generation of nanoparticles with adjustable size and controlled stoichiometry: Recent advances. *Langmuir*, 28(30):11241–11249, 2012.

[55] J. B. Park, S. F. Conner, and D. A. Chen. Bimetallic ptau clusters on tio2(110): growth, surface composition, and metalsupport interactions. *The Journal of Physical Chemistry C*, 112(14):5490–5500, 2008.

[56] N. Lidgi-Guigui, P. Mulheran, and R. E. Palmer. Seed induced growth of binary ag/au nanostructures on a graphite surface. *Applied Physics Letters*, 93(12):123107, 2008.

[57] Kenji Sumiyama, Takehiko Hihara, Dong Liang Peng, and Ryoji Katoh. Structure and magnetic properties of co/coo and co/si core-shell cluster assemblies prepared via gas-phase. *Science and Technology of Advanced Materials*, 6(1):18, 2005.

[58] E. Perez-Tijerina, M. Gracia Pinilla, S. Mejia-Rosales, U. Ortiz-Mendez, A. Torres, and M. Jose-Yacaman. Highly size-controlled synthesis of au/pd nanoparticles by inert-gas condensation. *Faraday Discuss.*, 138:353–362, 2008. doi: 10.1039/B705913M.

[59] S. Fedrigo, W. Harbich, and J. Buttet. Soft landing and fragmentation of small clusters deposited in noble-gas films. *Phys. Rev. B*, 58:7428–7433, Sep 1998.

[60] W. Harbich, S. Fedrigo, J. Buttet, and D. M. Lindsay. Deposition of mass selected gold clusters in solid krypton. *The Journal of Chemical Physics*, 96 (11):8104 – 8108, 1992.

[61] Harbich W., Fedrigo S., Meyer F., D. M. Lindsay, Lignieres J., Rivoal J C., and Kreisle D. Deposition of mass selected silver clusters in rare gas matrices. *The Journal of Chemical Physics*, 93(12):8535 – 8543, 1990.

[62] Riccardo Ferrando. Symmetry breaking and morphological instabilities in core-shell metallic nanoparticles. *Journal of Physics: Condensed Matter*, 2015. doi: 10.1088/0953-8984/27/1/013003.

[63] Diego Guedes-Sobrinho, Ricardo K. Nomiyama, Anderson S. Chaves, Maurício J. Piotrowski, and Juarez L. F. Da Silva. Structure, Electronic, and Magnetic Properties of Binary Pt n TM 55 n (TM = Fe, Co, Ni, Cu, Zn) Nanoclusters: A Density Functional Theory Investigation. *The Journal of Physical Chemistry C*, 119(27):15669–15679, 2015. ISSN 1932-7447.

[64] Davide Bochicchio and Riccardo Ferrando. Morphological instability of core-shell metallic nanoparticles. *The Journal of Physical Review B*, 165435 (January):1–13, 2013.

[65] Feng Yin, Zhi Wei Wang, and Richard E. Palmer. Controlled formation of mass-selected cuau coreshell cluster beams. *Journal of the American Chemical Society*, 133(27):10325–10327, 2011.

[66] Feng Yin, Zhi Wei Wang, and Richard E Palmer. Journal of Experimental Nanoscience Ageing of mass-selected Cu / Au and Au / Cu core / shell clusters probed with atomic resolution. *Journal of Experimental*

Nanoscience, 7(N. 6 October-November):703–710, 2012. ISSN 1745-8080. doi: 10.1080/17458080.2012.710856.

[67] Sheng Dai, Yuan You, Shuyi Zhang, Wei Cai, Mingjie Xu, Lin Xie, Ruqian Wu, George W Graham, and Xiaoqing Pan. core-shell formation in Pt 3 Co nanoparticles. *Nature Communications*, 8:1–8. ISSN 2041-1723.

[68] Keewah Chan, Boon Tong, Saadah Abdul, Muhamad Rasat, and Chang Fu. Annealing effect on the structural and optical properties of embedded Au nanoparticles in silicon suboxide films. *Vaccum*, 86(9):1367–1372, 2012. ISSN 0042-207X.

[69] Marin Tadic, Slavko Kralj, Marko Jagodic, Darko Hanzel, and Darko Makovec. Magnetic properties of novel superparamagnetic iron oxide nanoclusters and their peculiarity under annealing treatment. *Applied Surface Science*, 322:255–264, 2014. ISSN 01694332.

[70] Grégory Guisbiers, Subarna Khanal, Francisco Ruiz-zepeda, Jorge Roque, De Puente, and Miguel José-yacaman. CuNi nano-alloy: mixed, coreshell or Janus nano-particle? *Nanoscale*, 6:14630–14635, 2014. doi: 10.1039/c4nr05739b.

[71] Tianlong Wen and Kannan M. Krishnan. Thermal stability and morphological transformations of aucorecoshell nanocrucibles. *The Journal of Physical Chemistry C*, 114(35):14838–14842, 2010.

[72] Z W Wang and R E Palmer. Intensity calibration and atomic imaging of size-selected Au and Pd clusters in aberration-corrected HAADF-STEM. *Journal of Physics: Conference Series*, 371:012010, 2012. ISSN 1742-6596.

[73] P Hartel, H Rose, and C Dinges. Conditions and reasons for incoherent imaging in STEM. *Ultramicroscopy*, 63(96):93–114, 1996.

[74] Z. W. Wang, Z. Y. Li, S. J. Park, A. Abdela, D. Tang, and R. E. Palmer. Quantitative z-contrast imaging in the scanning transmission electron microscope with size-selected clusters. *Phys. Rev. B*, 84:073408, Aug 2011.

[75] Sreedevi A, Priyanka K P, Babitha K.K., Ganesh Sanjeev, and Thomas Varghese. Influence of electron beam irradiation on structural and optical properties of -ag2wo4 nanoparticles. *Micron*, 88, 05 2016.

[76] Haimei Zheng, Utkur M. Mirsaidov, Lin-Wang Wang, and Paul Matsudaira. Electron beam manipulation of nanoparticles. *Nano Letters*, 12(11):5644–5648, 2012.

[77] CM Wang, DR Baer, JE Amonette, MH Engelhard, JJ Antony, and Y Qiang. Electron beam-induced thickening of the protective oxide layer around fe nanoparticles. *Ultramicroscopy*, 108(1):43–51, December 2007. ISSN 0304-3991.

[78] E A Lewis, T J A Slater, E Prestat, A Macedo, P O Brien, P H C Camargo, and S J Haigh. Real-time imaging and elemental mapping of AgAu nanoparticle transformations. *Nanoscale*, 22:13598–13605, 2014.

[79] J. Liu, D. Foster, Z.Y. Li, N. Wilkinson, and J. Yuan. Coalescence dynamics of size-selected gold clusters studied by time-resolved transmission electron microscopy. *Journal of Physics: Conference Series*, 902(1):012008, 2017.

[80] M. Flueli, P.A. Buffat, and J.-P. Borel. Real time observation by high resolution electron microscopy (hrem) of the coalescence of small gold particles in the electron beam. *Surface Science*, 202(1):343 – 353, 1988. ISSN 0039-6028.

[81] F. Banhart, Ph. Redlich, and P.M. Ajayan. The migration of metal atoms through carbon onions. *Chemical Physics Letters*, 292(4):554 – 560, 1998. ISSN 0009-2614.

[82] Miyoko Tanaka, Masaki Takeguchi, and Kazuo Furuya. Behavior of metal nanoparticles in the electron beam. *Micron*, 33(5):441 – 446, 2002. ISSN 0968-4328.

[83] Mukesh Kumar Kumawat, Mukeshchand Thakur, Jaya R Lakkakula, Deepika Divakaran, and Rohit Srivastava. Evolution of thiol-capped gold nanoclusters into larger gold nanoparticles under electron beam irradiation. *Micron*, 95:1–6, 2017. ISSN 0968-4328.

[84] Yubiao Niu, Philomena Schlexer, Bela Sebok, Ib Chorkendorff, Gianfranco Pacchioni, and Richard E. Palmer. Reduced sintering of mass-selected au clusters on sio2 by alloying with ti: an aberration-corrected stem and computational study. *Nanoscale*, 10:2363–2370, 2018.

[85] B. Richter, H. Kuhlenbeck, H.-J. Freund, and P. S. Bagus. Cluster core-level binding-energy shifts: The role of lattice strain. *Phys. Rev. Lett.*, 93:026805, Jul 2004.

[86] S Peters, S Peredkov, M Neeb, W Eberhardt, and M Al-hada. Size-dependent xps spectra of small supported au-clusters. *Surface Science*, 608:129–134, 2013. ISSN 0039-6028.

[87] Ignacio Lopez-Salido, Dong Chan Lim, and Young Dok Kim. Ag nanoparticles on highly ordered pyrolytic graphite (hopg) surfaces studied using stm and xps. *Surface Science*, 588(1):6 – 18, 2005. ISSN 0039-6028. doi: https://doi.org/10.1016/j.susc.2005.05.021.

[88] Christian Mohr and Peter Claus. On the origin of binding energy shifts of core levels of supported gold nanoparticles and dependence of pretreatment and material synthesis. *Phys. Chem. Chem. Phys.*, 5:172–177, 2003.

[89] I Aruna, B R Mehta, L K Malhotra, and S M Shivaprasad. Size dependence of core and valence binding energies in Pd nanoparticles : Interplay

of quantum confinement and coordination reduction Size dependence of core and valence binding energies in Pd nanoparticles : Interplay of quantum confinement. *Journal of Applied Physics*, 064308(May 2013), 2008.

[90] J. E. Castle. Practical surface analysis by auger and x-ray photoelectron spectroscopy. *Surface and Interface Analysis*, 6(6):302–303, 1984.

[91] Evgeny I. Vovk, Alexander V. Kalinkin, Mikhail Yu. Smirnov, Igor O. Klembovskii, and Valerii I. Bukhtiyarov. Xps study of stability and reactivity of oxidized pt nanoparticles supported on tio2. *The Journal of Physical Chemistry C*, 121(32):17297–17304, 2017.

[92] Pilar Prieto, Valentin Nistor, Khalid Nouneh, Munetaka Oyama, Mohammed Abd-Lefdil, and Raquel Daz. Xps study of silver, nickel and bimetallic silvernickel nanoparticles prepared by seed-mediated growth. *Applied Surface Science*, 258(22):8807 – 8813, 2012. ISSN 0169-4332.

[93] A. Lewera, W.P. Zhou, C. Vericat, J.H. Chung, R. Haasch, A. Wieckowski, and P.S. Bagus. Xps and reactivity study of bimetallic nanoparticles containing ru and pt supported on a gold disk. *Electrochimica Acta*, 51(19): 3950 – 3956, 2006. ISSN 0013-4686.

[94] Selim Alayoglu, Simon K. Beaumont, Fan Zheng, Vladimir V. Pushkarev, Haimei Zheng, Viacheslav Iablokov, Zhi Liu, Jinghua Guo, Norbert Kruse, and Gabor A. Somorjai. Co2 hydrogenation studies on co and copt bimetallic nanoparticles under reaction conditions using tem, xps and nexafs. *Topics in Catalysis*, 54(13):778, Aug 2011.

[95] Yoshiteru Mizukoshi, Kenji Okitsu, Yasuaki Maeda, Takao A. Yamamoto, Ryuichiro Oshima, and Yoshio Nagata. Sonochemical preparation of bimetallic nanoparticles of gold/palladium in aqueous solution. *The Journal of Physical Chemistry B*, 101(36):7033–7037, 1997.

[96] S. Pratontepa, S. J. Carroll, C. Xirouchaki, M. Streun, and R. E. Palmer. Size-selected cluster beam source based on radio frequency magnetron plasma sputtering and gas condensation. *Review of Scientific Instruments*, 76:045103, 2005.

[97] Richard E. Palmer and Carl Leung. Immobilisation of proteins by atomic clusters on surfaces. *Trends in Biotechnology*, 25(2):48 – 55, 2007. ISSN 0167-7799.

[98] B. von Issendorff and R. E. Palmer. A new high transmission infinite range mass selector for cluster and nanoparticle beams. *Review of Scientific Instruments*, 70:4497, 1999.

[99] Simon R Plant, Lu Cao, Feng Yin, Zhi Wei Wang, and Richard E Palmer. Size-dependent propagation of au nanoclusters through few-layer graphene. *Nanoscale*, 6(3):1258–1263, 2014.

[100] David B. Williams and C. Barry Carter. *Transmission Electron MicroscopyA Textbook for Materials Science.* 2008. ISBN 9780387765006.

[101] Z.W.Wang, Z. Y. Li, S. J. Park, A. Abdela, D. Tang, and R. E. Palmer. Quantitative z-contrast imaging in the scanning transmission electron microscope with size-selected clusters. *Physical Review B - Condensed Matter and Materials Physics*, 84(7):2–4, 2011.

[102] DENSsolutions. Mems-based technology. *Nanochip*.

[103] Einstein Albert. ber einen die erzeugung und verwandlung des lichtes betreffenden heuristischen gesichtspunkt. *Annalen der Physik*, 322(6):132–148.

[104] Vickerman John C. *Molecular Surface Mass Spectrometry by SIMS*, chapter 4, pages 113–205. Wiley-Blackwell, 2009. ISBN 9780470721582.

[105] Ignacio Lopez Salido. Electronic and Geometric Properties of Silver and Gold Nanoparticles. 2007.

[106] David Henry Cant. Synthesis and characterisation of semiconductor nanoparticle thin films. *The University of Manchester*, 2013.

[107] URL https://fiji.sc/.

[108] Copyright 2005 casa software ltd. URL http://www.casaxps.com/.

[109] Saeed Gholhaki, Shih-Hsuan Hung, David J. H. Cant, Caroline E. Blackmore, Alex G. Shard, Quanmin Guo, Keith P. McKenna, and Richard E. Palmer. Exposure of mass-selected bimetallic ptti nanoalloys to oxygen explored using scanning transmission electron microscopy and density functional theory. *RSC Adv.*, 8:27276–27282, 2018.

[110] L. D. Marks. Experimental studies of small particle structures,. *Rep Prog. Phys*, 57:603–649, 1994.

[111] Wheeler P. Davey. Precision measurements of the lattice constants of twelve common metals,. *Phys Rev.*, 25:753–761, 1925.

[112] J. W. Arblaster. Crystallographic properties of platinum. *Platinum Metals Reviews*, 41(1):12, 1997.

[113] Ulrike Diebold. The surface science of titanium dioxide. *Surface Science Reports*, 48(5):53 – 229, 2003. ISSN 0167-5729.

[114] R C. Baetzold, G Apai, E Shustorovich, and R Jaeger. Surface core-level shifts for pt single-crystal surfaces. *Phys. Rev. B*, 26:4022–402, 1982.

[115] W Gpel, J.A Anderson, D Frankel, M Jaehnig, K Phillips, J.A Schfer, and G Rocker. Surface defects of tio2(110): A combined xps, xaes and els study. *Surface Science*, 139(2):333 – 346, 1984. ISSN 0039-6028.

[116] A. Kakanakova-Georgieva, Ts. Marinova, O. Noblanc, C. Arnodo, S. Cassette, and C. Brylinski. Interface chemistry of a ti/au/pt/ti/sic structure. *Applied Surface Science*, 121-122:208 – 212, 1997. ISSN 0169-4332.

[117] Alexander G. Shard. A straightforward method for interpreting xps data from core-shell nanoparticles. *The Journal of Physical Chemistry C*, 116 (31):16806–16813, 2012.

[118] David J. H. Cant, Yung-Chen Wang, David G. Castner, and Alexander G. Shard. A technique for calculation of shell thicknesses for coreshellshell nanoparticles from xps data. *Surface and Interface Analysis*, 48(5):274–282.

[119] Caroline Elizabeth Blackmore. Experimental and Theoretical Studies of the Atomic Structure of Platinum-based Nanoclusters. *The University of Birmingham*, (September), 2016.

[120] Dawn Michelle Foster. Production and characterisation by scanning transmission electron microscopy of size-selected noble metal nanoclusters by. *The University of Birmingham*, 2017.

[121] Shih-Hsuan Hung and Keith P. McKenna. First-principles investigation of titanium nanoparticle oxidation. *J. Phys. Chem. C*, 122(5):3107–3114, 2018.

[122] Yoshiyuki Matsuura, Satoshi Seino, Tomohisa Okazaki, Tomoki Akita, Takashi Nakagawa, and A. Yamamoto Takao. Synthesis of carbon-supported ptrh random alloy nanoparticles using electron beam irradiation reduction method. *Radiation Physics and Chemistry*, 122:9–14, 2016.

[123] Kun Cao, Xiao Liu, Qianqian Zhu, Bin Shan, and Rong Chen. Atomically controllable pd@pt core–shell nanoparticles towards preferential oxidation of co in hydrogen reactions modulated by platinum shell thickness. *ChemCatChem*, 8:326–330, 2016.

[124] Deli Wang, Huolin L. Xin, Robert Hovden, Hongsen Wang, Yingchao Yu, David A. Muller, Francis J. DiSalvo, and Hector D. Abruna. Structurally ordered intermetallic platinum–cobalt core–shell nanoparticles with enhanced

activity and stability as oxygen reduction electrocatalyst. *Nature Materials*, 12:8187, 2013.

[125] R. Nakamura, D. Tokozakura, H. Nakajima, and H. Mori. Hollow oxide formation by oxidation of al and cu nanoparticles. *Journal of Applied Physics*, 101:074303, 2007.

[126] Yu.V. Fedoseeva, L. G. Bulusheva, A. V. Okotrub, D. V. Vyalikh, Junping Huo, Huaihe Song, and Jisheng Zhou Xiaohong Chen. Effect of oxidation and heat treatment on the morphology and electronic structure of carbon-encapsulated iron carbide nanoparticles. *Materials Chemistry and Physics*, 135:235–240, 2012.

[127] Caroline E. Blackmore, Neil V. Reesb, and E. Palmer Richard. Modular construction of size-selected multiple- core pt–tio2 nanoclusters for electrocatalysis. *Phys.Chem.Chem.Phys*, 17(28005), 2015.

[128] J. P. Perdew, K. Burke, and M. Ernzerhof. Generalized gradient approximation made simple. *Phys. Rev. Lett.*, 77:3865, 1996.

[129] G. Kresse and J. Furthmuller. Efficient iterative schemes for ab initio total-energy calculations using a plane-wave basis set. *Phys. Rev. B*, 54:11169, 1996 .

[130] Keith P. McKenna. Gold nanoparticles under gas pressure. *Phys.Chem Chem Phys.*, 11:4145–4151, 2009.

[131] A. N. Chibisov. Oxygen adsorption on small ti clusters: A first-principles study,. *Comp Mater. Sci*, 82:131–133, 2014.

[132] J. Zemann. Crystal structures, 2nd edition. Vol. 1 by R. W. G. Wyckoff. *Acta Crystallographica*, 18(1):139–139, 1965.

[133] D. A. Outka, J. Stöhr, W. Jark, P. Stevens, J. Solomon, and R. J. Madix. Orientation and bond length of molecular oxygen on ag (110) and pt (111):

A near-edge x-ray-absorption fine-structure study,. *Phys Rev. B*, 35:4119, 1987.

[134] A. Janotti, J. B. Varley, P. Rinke, N. Umezawa, G. Kresse, and C. G. Van de Walle. Hybrid functional studies of the oxygen vacancy in tio_2,. *Phys Rev. B*, 81:085212, 2010.

[135] G. Charlton, P. B. Howes, C. L. Nicklin, P. Steadman, J. S. G. Taylor, C. A. Muryn, S. P. Harte, J. Mercer, R. McGrath, D. Norman, and Others. Relaxation of tio_2 (110)-(1× 1) using surface x-ray diffraction,. *Phys Rev. Lett.*, 78:495, 1997.

[136] Jose Luis Elechiguerra, Jose Reyes-Gasga, and Miguel Jose Yacaman. The role of twinning in shape evolution of anisotropic noble metal nanostructures,. *J Mater. Chem*, 16:3906–3919, 2006.

[137] Francesca Baletto and Riccardo Ferrando. Structural properties of nanoclusters: Energetic, thermodynamic, and kinetic effects,. *Rev Mod. Phys*, 77:371, 2005.

[138] Chang Raymond. *Physical chemistry for the chemical and biological sciences.* University Science Books, 2000.

[139] Y. A. Mastrikov, E. Heifets, E. A. Kotomin, and J. Maier. Atomic, electronic and thermodynamic properties of cubic and orthorhombic lamno3 surfaces. *Surface Science*, 603:326–335, 2009.

[140] Fen Liu, Zhijuan Zhao, Limei Qiu, and Liangzhong Zhao. Applications of XPS on Nanoscale Material Research. *Journal of Surface Analysis*, 15(3): 271–273, 2009.

[141] Norbert Kruse and Sergey Chenakin. Applied Catalysis A : General XPS characterization of Au / TiO 2 catalysts : Binding energy assessment and

irradiation effects. *Applied Catalysis A, General*, 391(1-2):367–376, 2011. ISSN 0926-860X.